Transverse Waves in the Solar Corona

by

Rebecca Sarah White

Thesis

Submitted to the University of Warwick

for the degree of

Doctor of Philosophy

Department of Physics

May 2014

THE UNIVERSITY OF
WARWICK

Contents

iii

List of Tables

List of Figures

x

Acknowledgments

First and foremost I would like to thank my supervisor Erwin Verwichte for his support, guidance and endless enthusiasm which has made my PhD a truly enjoyable experience. I am also grateful to STFC for financial assistance through an STFC studentship. I would like to thank my parents, Andy and Annette, brother Chris, and the wider family for their support and encouragement throughout my education and beyond. Thanks also to members of the CFSA and other postgraduate students in the physics department, for insightful discussions and distractions, both work related and otherwise. Lastly thanks to my friends at Myton church, for all the support and fellowship I have enjoyed over the last four years, not least the countless roast dinners!

This thesis was typeset with LaTeX 2_ε[1] by the author.

---

[1] LaTeX 2_ε is an extension of LaTeX. LaTeX is a collection of macros for TeX. TeX is a trademark of the American Mathematical Society. The style package *warwickthesis* was used.

Declarations

This thesis is submitted to the University of Warwick in support of my application for the degree of Doctor of Philosophy. It has been composed by myself and has not been submitted in any previous application for any degree. Work presented in this thesis has been published in the following peer-reviewed journal articles:

1. R. S. White and E. Verwichte. *Transverse coronal loop oscillations seen in unprecedented detail by AIA/SDO*, A&A, 537, A49 (2012)

2. R. S. White, E. Verwichte and C. Foullon. *First observation of a transverse vertical oscillation during the formation of a hot post flare loop*, A&A, 545, A129 (2012)

    • C. Foullon determined the geometry of the hot loop by comparing STEREO-B/EUVI observations with SDO/AIA observations, produced figure 4.11 and contributed useful discussions.

3. R. S. White, E. Verwichte and C. Foullon. *Anti-phase signature of flare generated transverse loop oscillations*, ApJ, 774, 104 (2013)

    • C. Foullon contributed useful discussions.

Abstract

Transverse loop oscillations (TLOs) are standing oscillations of coronal loops that are interpreted as kink waves in Magneto-hydrodynamic theory. These waves are particularly important as they can be used to infer local plasma properties such as the magnetic field strength through the technique of coronal seismology. In this thesis TLOs are studied both observationally, primarily with the Atmospheric Imaging Assembly (AIA) instrument on the Solar Dynamics Observatory (SDO) satellite, and numerically using the Lare2D code.

In the first observational study, eleven transversely oscillating loops in three active regions are analysed in detail. The time series analysis revealed periods between 1.7 and 10 minutes and damping times between 2.9 and 13 minutes and are compared with previously observed events. Coronal seismology of the kink mode is applied to determine the range of the internal Alfvén speed and the magnetic field strength for each loop. The magnetic field strength is found to have a range of $4 - 18$ G.

The second observational study presents the first observation of a transverse oscillation in a hot coronal loop following a linked coronal-flare mass-ejection event. The TLO is observed exclusively in the 131 Å and 94 Å bandpasses, indicating a loop plasma temperature in the range of 9 - 11 MK. Furthermore, the loop is not observed to cool into the other AIA channels, but just disappears from all bandpasses at the end of the oscillation. The time series analysis reveals a period of 302 ± 14 s (291 ± 9 s) and a damping time of 306 ± 43 s (487 ± 125 s) for the first (second) loop strand and a spatial phase shift along the loop of approximately $180°$ suggests that a higher order harmonic is observed. We show that the excitation mechanism of this unusual oscillation is directly connected with the reconnection processes that form the post flare loop. This differs from the blast wave excitation mechanism often proposed as the cause of cooler transverse loop oscillations.

The third observation presents another unusual TLO event that is also shown to have a direct link to the local magnetic field topology and the flare reconnection processes. A transversely oscillating coronal loop seen in the 171 Å bandpass is seen to oscillate in anti-phase with respect to adjacent larger loops seen in the 193 Å and 211 Å bandpasses. The local magnetic topology of the active region is modelled using potential field source surface (PFSS) extrapolation which reveals that the loops are anchored in different topological regions with footpoint locations identified either side of the EUV flare peak emission source. Lastly, numerical simulations using the Lare2D code are performed to further investigate the anti-phase TLO observations. Loops positioned in different topological regions above and below a magnetic X-point are impulsively excited and we observe inwardly directed anti-phase oscillations of the loops. In addition we show that both the loop oscillations and the oscillatory behaviour of the X-point are independent of the resistivity.

Chapter 1

The Sun and Magnetohydrodynamics

1.1 Outline of the thesis

In this thesis, three observational studies and one numerical study of transverse loop oscillations (TLOs) are presented. Chapters 1 and 2 put the work into context and give a review of previous observational examples of TLOs. Chapter 3 presents the first study of multiple TLOs observed in three active regions. Periods and damping times of the oscillations are compared with previous works and the intensity variations of the loop oscillations are studied. Using the multiple TLO observations, the seismology of the corona is probed. Chapter 4 presents the first study of a hot transverse loop oscillation where the loop temperature is in the range of 9 - 11 MK. This TLO is also unusual due to its vertically polarised oscillation and that it fades from view soon after its oscillation has decayed. In Chapter 5 an observation of TLOs displaying anti-phase behaviour is presented. Here, the observations are compared with a potential magnetic field extrapolation to probe the local magnetic topology of the active region. Chapters 4 and 5 discuss observations of TLOs that are proposed to have an excitation mechanism that differs to the often assumed blast wave scenario and where the reconnection processes are shown to play an important role in the perturbation of the transverse oscillations. Chapter 6 presents numerical simulations of loops located in different topological regions above and below a magnetic X-point to further investigate the novel observations discussed in Chapter 5. The thesis is summarised in Chapter 7.

1.2 The Sun

Our closest star plays host to some of the most spectacular and energetic phenomena in our Solar system. Flares and coronal mass ejections (CMEs) are two such phenomena that are responsible for some of the damaging consequences of space weather which can have an impact on both space and Earth based technologies. These events can also produce non damaging effects such as natural light displays in the form of the aurora at the Earth's north and south poles. The Sun is a main sequence star with spectral classification G2. It has a mass of 2×10^{30} kg, a radius of 6.96×10^8 m and a luminosity of 3.83×10^{26} W. It is located at a distance of approximately 10 kpc (1 pc = 3.086×10^{13} km) from the center of the milky way and it takes the Sun 250 million years, travelling at 250 km s^{-1} to do a complete revolution of the galaxy (Foukal 2013). Studying the Sun and the processes that govern it provides a greater understanding of dynamic Solar events such as flares and CMEs. In addition it can also serve as a remote laboratory for studying processes that cannot be or are difficult to replicate on Earth. The Sun, like Earth, is made up of several layers. It consists of a central core where the Sun's energy is generated, radiation and convection zones where this energy is transported from the core towards the upper layers, the photosphere and the atmosphere comprising of the chromosphere, transition region and corona. This structure is illustrated in figure 1.1.

1.2.1 Probing the Solar interior

Direct observations of the interior layers of the Sun are impossible, however the internal structure and physical processes can be inferred using indirect observations (e.g. the neutrino flux from the fusion reaction in the core) and methods (e.g. helioseismology). Indirect observational results can then be combined with observables such as the mass, and luminosity to test and develop the Standard Solar Model (SSM) which is the best model describing the Sun to date and which assumes that the Sun is spherical and that the effects of rotation and magnetic fields are negligible (Antia et al. 2003; Dwivedi and Parker 2003).
The Sun generates its energy by fusion reactions in the hot core (T $\approx$ 15 MK) between hydrogen and other light elements and this energy is then radiated and convected up through the layers. Direct evidence for the fusion process is given by the neutrino flux which can be detected using Earth based detectors. The SSM predicts fusion to occur via two reaction mechanisms: the pp chain which begins by the reaction between two protons or two protons and an electron, and the CN
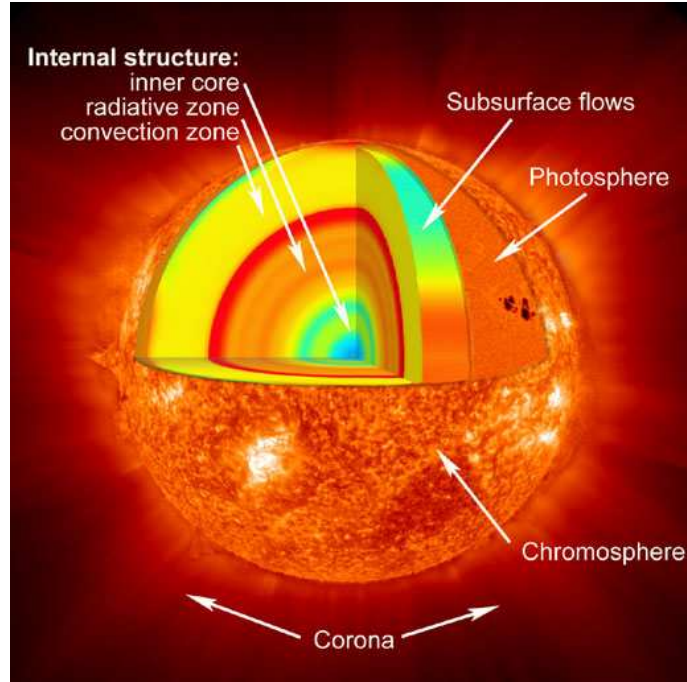
Figure 1.1: The structure of the Sun. (Image from NASA)

chain which begins with the reaction between a proton and a carbon nucleus. The pp chain is the dominant mechanism by which the energy is generated, providing approximately 99% of the power output compared with 1% provided by the CN chain. Both chains produce electron neutrinos from their reactions. When the first neutrino measurements were made, a discrepancy was found between the predicted neutrino flux from the SSM and the observed flux. This became known as the solar neutrino problem which was resolved thanks to the Japanese detector SuperKamiokande shown in figure 1.2. By studying high energy neutrinos from cosmic rays in the Earth's atmosphere, it discovered that neutrinos can oscillate between flavours i.e. an electron neutrino can become a muon neutrino. Early observations were sensitive exclusively to the electron neutrinos which is the only flavour generated by fusion. Taking into account the flavour oscillations of neutrinos as they travel from the Sun to Earth, the observed flux was found to match well with the flux predicted by the SSM (Dwivedi and Parker 2003).

Another powerful tool for probing the interior of the Sun and testing current models is helioseismology. The solar interior is able to support acoustic wave modes (or p modes) and gravity wave modes (or g modes) which have pressure and buoyancy respectively as their main restoring forces. There are also fundamental wave modes (or f modes) which are surface gravity modes with amplitudes that decrease with

3
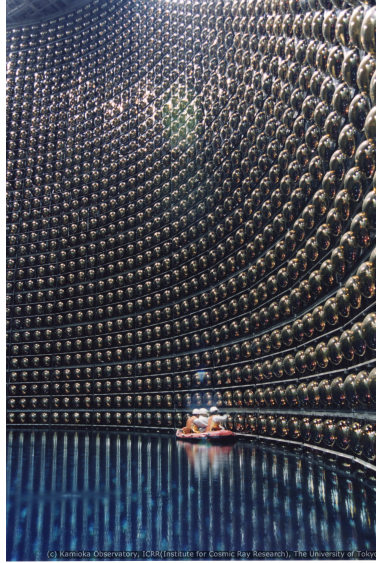
Figure 1.2: The Japanese neutrino detector SuperKamiokande that helped to solve the solar neutrino problem.

depth. The acoustic modes are excited by the turbulence in the convection zone which extends approximately a third of the solar radius towards the core and are trapped in cavities below the surface as long as they have frequencies that are less than the photospheric acoustic cutoff frequency with a period of approximately 3 minutes. As the waves travel deeper into the solar interior the sound speed increases since the velocity is proportional to the square root of the temperature, so that the waves are refracted and at a certain point are totally internally reflected. Waves with a larger wave number are reflected at a shallower depth compared with waves that have smaller wave numbers and therefore are excellent probes of the internal thermal structure. An important application of observing acoustic p modes is that they can be used to image active regions that are at the other side of the Sun to the Earth which may not be visible with satellites. This could be used as a tool for predicting future solar activity (Foukal 2013).

For as long as magnetic structures such as sunspots have been observed, the rotation rate of the Sun has been measured. The observed rotation rate at the equator is approximately 25 days which increases as you move towards the poles. Structures such as sunspots have been shown to rotate faster at all latitudes than the photospheric plasma and this difference in speed suggests that these solar features are actually located below the surface of the Sun where the rotation rate is slightly higher. The differential rotation observed at the photosphere continues down into the convection zone, however the core and radiative zones rotate rigidly at the value of the photo-
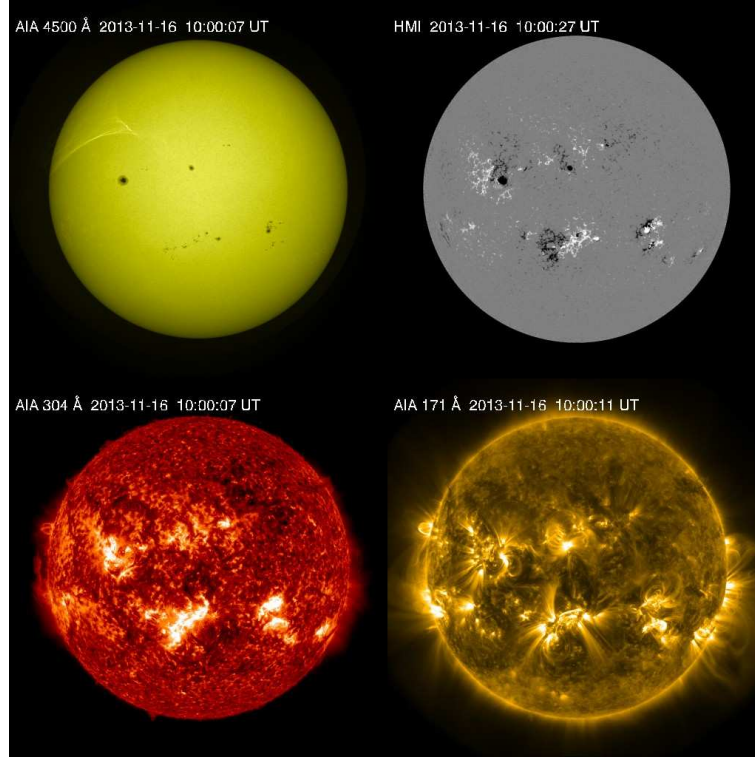
Figure 1.3: From left to right, top to bottom: The photosphere (SDO/AIA 4500 Å), line of sight magnetic field strength (HMI magnetogram), the chromosphere (SDO/AIA 304 Å) and corona (SDO/AIA 171 Å). (Data from the Virtual Solar Observatory).

spheric equatorial (mid latitude) rate. Between the radiative and convective zones is a slim layer called the tachocline. The tachocline marks the change from the rigid body rotation of the radiative zone and the differential rotation of the convective zone and above. It is thought to have a width of no more than a few percent of the solar radius and to be the location of the solar dynamo where the magnetic field is generated (Dwivedi and Parker 2003; Foukal 2013).

1.2.2 The photosphere, chromosphere and transition region

The photosphere is a narrow layer of the Sun located above the convection zone and beneath the chromosphere with a temperature of about 5000 K. It marks a point between what we are able to directly observe (e.g. sunspots and activity in the atmosphere) and what we cannot (e.g. fusion in the core). Features visible at the photospheric level include sunspots as shown in the top left of figure 1.3. These are regions that are often situated below active regions visible higher up in the atmo-

sphere and which have strong magnetic field strengths, in the range of 2000-3000 G, and lower temperatures than the background photosphere of around 4500 K. Granulation patterns visible at the photospheric level provide evidence for convection beneath the visible layers since they show bright cell structures which are separated by dark lanes highlighting up-flowing and down-flowing plasma respectively. Observations of the photospheric magnetic field obtained as magnetograms (e.g. top right of figure 1.3) from instruments such as the Heliospheric Magnetic Imager (Schou et al. 2012) on the Solar Dynamics Observatory (SDO) (Pesnell et al. 2012) give information on the geometry of the magnetic field.

Just before and after a total solar eclipse a thin red layer of the solar atmosphere is observed above the limb. This region is called the chromosphere and extends approximately 2000-3000km above the temperature minimum. Here temperatures rise from photospheric temperatures up to 10,000 - 20,000 K and densities that decrease rapidly from 10^{15} cm^{-3} near the photosphere to 10^{11} cm^{-3}. Bottom left of figure 1.3 shows the chromosphere as seen by SDO. Neutral hydrogen which has an ionisation temperature of around 11,000 K is still present so that the chromosphere is only partially ionised. This is an important layer of the solar atmosphere since it provides hot up-flows of plasma to structures higher up in the corona such as loops. Located between the chromosphere and corona is the transition region. This is a thin region with a thickness of approximately 100 km where hydrogen becomes fully ionised and the temperature increases rapidly up to the million degree temperatures of the corona (Aschwanden 2005).

1.2.3 The corona

The corona is the outer part of the solar atmosphere that extends out to several solar radii into interplanetary space. Temperatures in this region are of the same order of magnitude as the core temperatures and range from around 1 MK in quiet Sun regions up to 10's of MK in flaring active regions. Bottom right of figure 1.3 shows the corona as viewed by the 171 Å bandpass of the Atmospheric Imaging Assembly instrument (Lemen et al. 2012) on SDO, which corresponds to temperatures of around 1 MK. The surprisingly hot temperature of the corona was originally discovered from observations of the red (6374 Å) and green (5303 Å) emission lines formed due to highly ionised iron and were first identified in 1869 by Edlén (1943). The corona is a highly structured, magnetically dominated, fully ionised plasma which due to its elasticity and compressibility allows waves to propagate through it. It is characterised by three components: The K-corona due to photospheric light scattered by free electrons, the L-corona which is the spectral line emission from
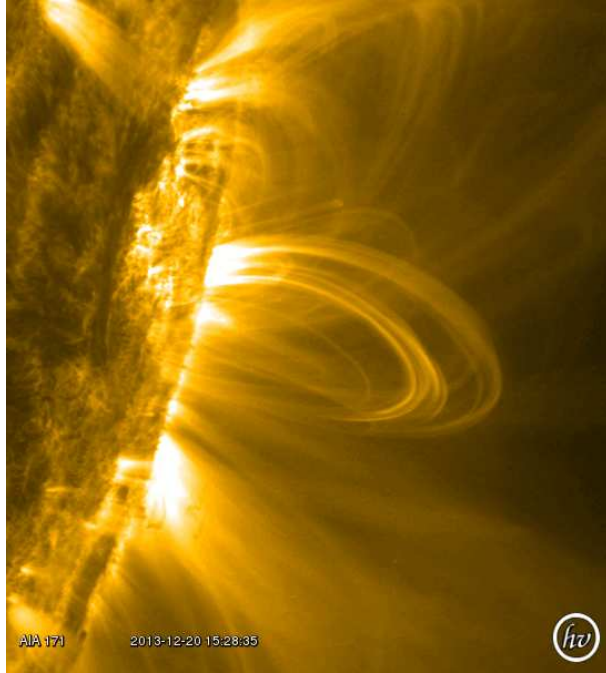
Figure 1.4: Coronal loops on the solar limb viewed in the 171 Å bandpass by the Solar Dynamics Observatory. (Courtesy of Helioviewer.org).
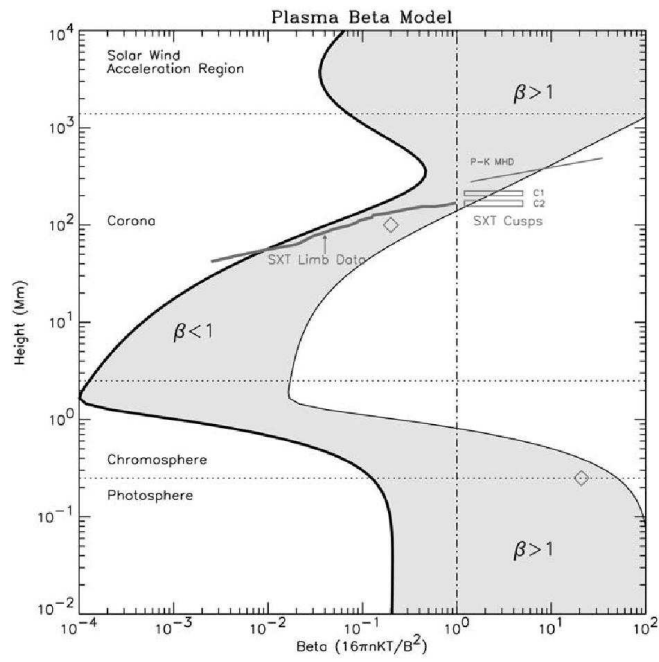
Figure 1.5: Modelled variation of the plasma β with height in the solar atmosphere. Taken from Gary (2001).

highly ionised atoms and the F-corona due to absorption lines of the photospheric Fraunhofer spectrum caused by diffraction from interplanetary dust (Aschwanden 2005). The corona can be divided into three main regions; active regions, coronal holes and quiet Sun regions. Active regions are regions of strong, mainly closed magnetic field concentrations which are visible as sunspots in optical wavelengths. Active regions are normally associated with dynamic events and processes such as solar flares, CMEs and magnetic reconnection. Coronal holes are located in the northern and southern polar zones and are dominated by open magnetic field lines. These zones appear dark because they are empty of plasma due to the efficient transport of plasma into the solar wind. Quiet Sun regions are defined to be regions of closed magnetic field lines that are not active regions or coronal holes, where dynamic processes can still occur. An important parameter in the solar atmosphere is the plasma-β parameter. This is the ratio between the plasma pressure and the magnetic pressure. For a region that is dominated by the magnetic field such as the corona then $\beta < 1$. A consequence of this is that the coronal plasma is mostly magnetically confined and organised into thin density enhanced magnetic flux tubes called coronal loops filled with heated plasma from the chromosphere. An image of coronal loops on the solar limb observed by SDO is shown in figure 1.4. For a region dominated by the plasma pressure, $\beta > 1$ and the magnetic field is dragged along by the plasma. This happens in regions below the atmosphere for example the photosphere and the solar wind regions. Figure 1.5 shows the modelled variation of the plasma-β with height in the solar atmosphere (Aschwanden 2005).

1.2.4 The solar cycle

The Sun undergoes an 11 year cycle during which the global magnetic field reverses its polarity. During this cycle the global magnetic field, under the influence of the differential rotation, evolves from an initial poloidal field at solar minimum towards a toroidal field at solar maximum. The magnetic flux reaches a maximum during the peak of the cycle when the flux in active regions can be eight times greater compared to the flux measured during the minimum part of the cycle. The frequency of energetic events such as solar flares also increases around the cycle maximum. A full cycle of 22 years, called the Hale cycle, marks the return of the magnetic field to the original polarity. Observations of sunspots since 1749 demonstrate the eleven year cycle through the butterfly diagram of sunspots. This butterfly diagram (figure 1.6) shows the latitude of sunspots against time and demonstrates that sunspots, and therefore active regions, migrate from high latitudes at the start of the cycle towards the equator at the end. There is also evidence of longer period cycles such

DAILY SUNSPOT AREA AVERAGED OVER INDIVIDUAL SOLAR ROTATIONS
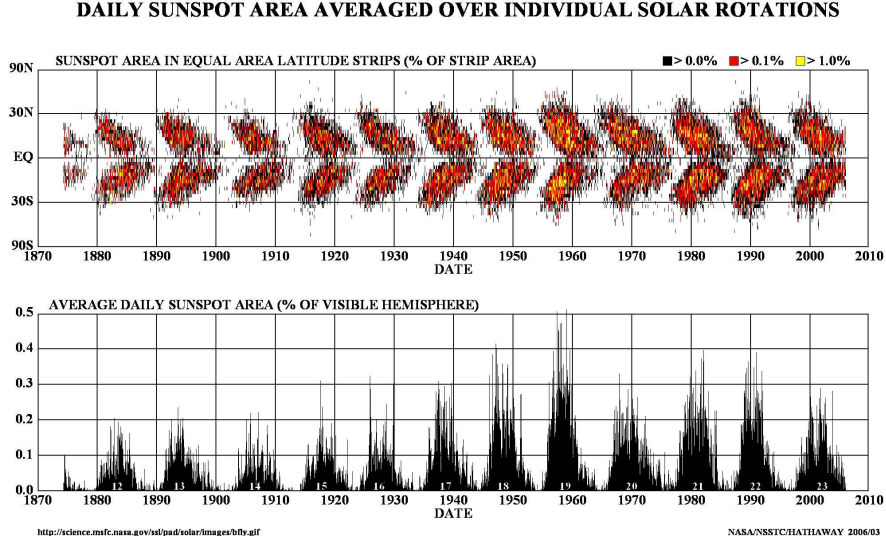
Figure 1.6: The butterfly diagram of sunspots (Image courtesy of NASA).

as the 80 year sunspot cycle (Gleissberg 1952) and time periods of unusually low activity such as the Maunder Minimum where there was little activity for a 70 year period between 1645 and 1715. The amplitude of the cycles also show variation with some periodicity (Antia et al. 2003; Dwivedi and Parker 2003).

1.3   Observing the corona

The brightest emission from the solar corona is in the EUV, soft X-ray, hard X-ray and radio wavelengths and observations are made using a variety of space and Earth based instruments. Current projects providing observational data of the corona include the Reuven Ramaty High Energy Solar Spectroscopic Imager (RHESSI) (Lin et al. 2002) which studies the X-ray emission from solar flares (Fletcher et al. 2011), the Interface Region Imaging Spectrograph (IRIS) (De Pontieu et al. 2014) which aims to study the transition region and the flow of energy and mass from the photosphere to the corona, and the ground based Coronal Multi-channel Polarimeter (CoMP) (Tomczyk et al. 2008) at Sacramento Peak Observatory in New Mexico which observes the low coronal magnetic field and the line of sight Doppler velocity. Of particular importance for observing coronal structures with high spatial resolution are the EUV imaging satellites.

The Transition Region and Coronal Explorer (TRACE) (Handy et al. 1999) was launched in 1998 and its telescope was designed to operate in three EUV wavelengths

9
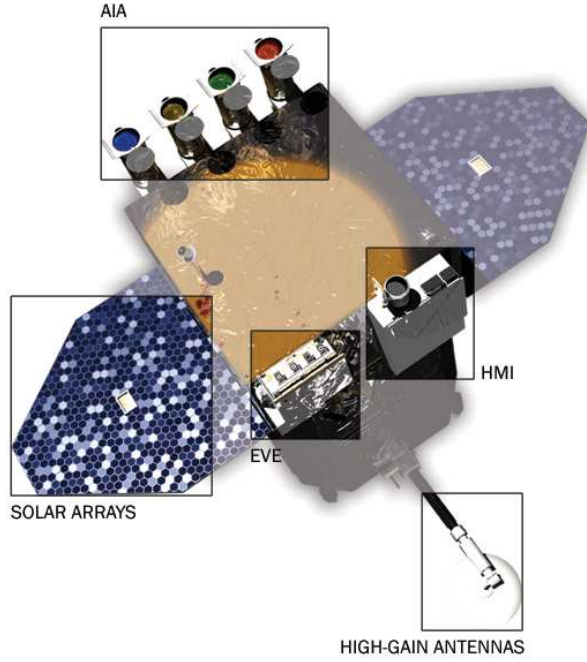
Figure 1.7: The Solar Dynamics Observatory (SDO) (Image courtesy of NASA).

(171 Å, 195 Å, 284 Å) with a spatial resolution of $1''$, a pixel size of $0.5''$, and a field of view of $8.5' \times 8.5'$. The first observations of transverse loop oscillations were made using this instrument (Aschwanden et al. 1999b) however the limited field of view meant that many potentially interesting events were not observed. The Solar Dynamics Observatory (SDO) sought to build on the success of TRACE by improving the temporal resolution, increasing the number of EUV channels so that observations at hotter temperatures could be conducted, and extending the field of view to the whole solar disk.

1.3.1 The Solar Dynamics Observatory

The Solar Dynamics Observatory (SDO), shown in figure 1.7, was launched in February 2010 into an inclined geosynchronous orbit. SDO carries on board three instruments; The Atmospheric Imaging Assembly (AIA), the Helioseismic and Magnetic Imager (HMI) and the Extreme ultraviolet Variability Experiment (EVE) (Woods et al. 2012). The AIA (Lemen et al. 2012), designed to focus on the magnetic environment in the corona and its interaction with the coronal plasma, provides continuous observations of the full solar disk. It consists of four Cassegrain tele-
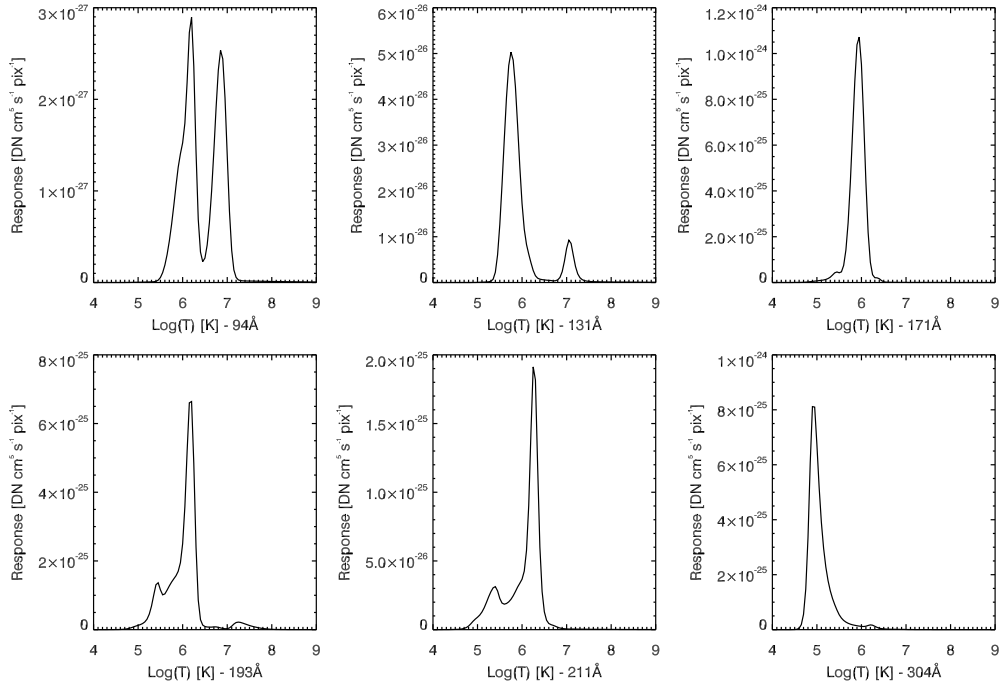
Figure 1.8: The temperature response of the 94 Å, 131 Å, 171 Å, 193 Å, 211 Å and 304 Å AIA bandpasses.

scopes that are optimized to observe the transition region and corona in one UV and six EUV band passes (Fe XVIII (94 Å), Fe VIII/XXI (131 Å), Fe IX (171 Å), Fe XII/XXIV (193 Å), Fe XIV (211 Å), He II (304 Å), Fe XVI (335 Å)) and the photosphere with wavelengths of 4500 Å and 1700 Å. AIA has a spatial resolution of 1.5″, a pixel size of 0.6″, a field of view of 41′×41′, and a temporal resolution of approximately 12 seconds. This improved temporal resolution compared with other instruments such as TRACE allows dynamics on much shorter time scales then previously observed to be studied. Figure 1.8 shows the temperature dependence of the AIA EUV bandpasses, for example the 171 Å bandpass is sensitive to emission at temperatures of just under 1 MK. Multiple peaks are visible in some of the temperature responses, for example the 131 Å bandpass is sensitive to emission peaking just under 1 MK and just over 10 MK. Care must therefore be taken when observing and comparing coronal features seen in different AIA bandpasses. The multithermal behaviour of the temperature response may cause difficulties in determining the approximate temperature of the observed plasma, and a feature observed in one bandpass may not correspond exactly to a feature seen in another bandpass. The HMI (Scherrer et al. 2012) measures full disk Doppler velocity and the line of

11

sight magnetic flux every 45 seconds and can provide vector magnetograms up to every 90 seconds. HMI has a pixel size of $0.5''$ and the same field of view as AIA. Lastly EVE measures the EUV full disk solar irradience with the aim of studying the variability of the irradiance on both long and short time scales.

1.3.2 The Solar Terrestrial Relations Observatory

Another important satellite for coronal observations is the Solar Terrestrial Relations Observatory (STEREO) which consists of two spacecraft, one ahead of Earth's orbit (STEREO A) and the other behind (STEREO B). At certain times this can enable observations of regions of the Sun that are on the opposite side to that facing Earth to be undertaken. Another important application of this satellite is that it can be used to infer the 3D geometry of solar structures such as coronal loops (Aschwanden et al. 2008; Verwichte et al. 2009). This can be achieved by either comparing the two different views of STEREO A and B or by comparing one of the STEREO views with another view such as that from SDO which observes the Sun from the Earth viewpoint. The Extreme Ultraviolet Imager (EUVI) instrument (Howard et al. 2008) on board STEREO observes the Sun in four band passes; Fe IX (171 Å), Fe XII (195 Å), Fe XV (284 Å) and He II (304 Å). EUVI has a pixel size of $1.6''$ and the CCDs consist of 2048 x 2048 pixels which provides a circular field of view of ±1.7 solar radii.

1.4 Magnetohydrodynamics

Plasma, often referred to as the fourth state of matter is gas that has been ionised, is electrically neutral and is characterised by long range electromagnetic forces between charged particles. These long range Coulomb forces mean that a single charged particle will interact with many other particles leading to a collective behaviour that can be compared to a fluid. A complete description of a plasma with N particles (where $N \gg 1$) needs N particle equations plus Maxwell's equations which is impractical to solve. For example in the solar corona N per unit volume is on the order of 10^9 cm^{-3}. To simplify this problem models have been developed that describe plasmas under certain assumptions and it is here that Magnetohydrodynamics (MHD) is introduced. MHD describes slow, large scale flow in plasmas under the following assumptions (Goossens 2003; Aschwanden 2005):

- $v \ll c$. Characteristic speeds are much slower than the speed of light so that relativistic effects are ignored.

- The typical length scales are much greater than the ion gyro-radius and the typical timescales are much slower than the ion gyro-frequency.

- Quasi-neutrality. The total charge of the plasma is approximately 0 so that $n_e \approx n_i$ and $\mathbf{j} = -n_e e(\mathbf{v}_e - \mathbf{v}_i)$. n_e and n_i are the electron and ion number densities respectively, $\mathbf{j}$ is the current density, e is the electric charge and $\mathbf{v}_e$ and $\mathbf{v}_i$ are the electron and ion velocities respectively.

- Characteristic timescales are much longer than the collision timescales and characteristic spatial scales are longer than the collision mean free path.

The equations describing plasmas in the MHD limit are a combination of the hydrodynamic fluid equations and Maxwell's equations of electrodynamics linked together by the generalised Ohm's law. The single fluid equations are,

$$\frac{D\rho}{Dt} + \rho \nabla.\mathbf{v} = 0, \tag{1.1a}$$

$$\rho \frac{D\mathbf{v}}{Dt} + \nabla p - \rho \mathbf{g} - \mathbf{j} \times \mathbf{B} = 0, \tag{1.1b}$$

$$\nabla.\mathbf{j} = 0, \tag{1.1c}$$

$$\frac{\rho^\gamma}{\gamma - 1} \frac{D}{Dt} \left(\frac{p}{\rho^\gamma} \right) = \eta j^2. \tag{1.1d}$$

These are the mass, momentum, charge conservation and energy equations respectively. Here,

$$\frac{D}{Dt} = \frac{\partial}{\partial t} + \mathbf{v}.\nabla, \tag{1.2}$$

is the material derivative, ρ is the mass density, $\mathbf{v}$ is the bulk velocity, p is the pressure, $\mathbf{B}$ is the magnetic field, $\mathbf{g}$ is the gravitational acceleration, $\mathbf{j}$ is the current density and γ is the ratio of specific heats which is 5/3 in the corona.

Maxwell's equations are Gauss' law, the solenoidal condition, Faraday's law and Ampère's law,

$$\nabla.\mathbf{E} = \frac{\rho_E}{\epsilon_0}, \tag{1.3a}$$

$$\nabla.\mathbf{B} = 0, \tag{1.3b}$$

$$\frac{\partial \mathbf{B}}{\partial t} = -\nabla \times \mathbf{E}, \tag{1.3c}$$

$$\nabla \times \mathbf{B} = \mu_0 \mathbf{j}, \tag{1.3d}$$

where $\mathbf{E}$ is the electric field strength, ρ_E is the electric charge density, ϵ_0 is the permittivity of free space and μ_0 is the permeability of free space. For non relativistic speeds and low frequency temporal behaviour the displacement current is negligible and is therefore neglected from Ampère's law. Since $\nabla \cdot \nabla \times \mathbf{B} = 0$, $\mathbf{B}$ and $\mathbf{j}$ are divergence free in MHD.

To provide a closed set of MHD equations and link $\mathbf{j}, \mathbf{B}$ and $\mathbf{E}$ with $\mathbf{v}$, generalised Ohm's law is introduced. This is derived by multiplying the momentum conservation equation for each species, Eq. (1.1b), by q/m and summing over all particle species. For a fully ionised plasma the particle species are electrons and ions. Additionally it is assumed that the ions are protons. Generalised Ohm's law is,

$$\mathbf{E} = -\mathbf{v} \times \mathbf{B} + \eta \mathbf{j}, \qquad (1.4)$$

The electric field is eliminated by combining Faraday's law (Eq. (1.3c)) with Ohm's law (Eq. (1.4)) to derive the induction equation,

$$\frac{\partial \mathbf{B}}{\partial t} = -\nabla \times \mathbf{E} = \nabla \times (\mathbf{v} \times \mathbf{B} - \eta \mathbf{j}). \qquad (1.5)$$

Therefore the set of ideal MHD equations, including resistivity but ignoring the effects of gravity are,

$$\frac{\partial \rho}{\partial t} = -\nabla . (\rho \mathbf{v}), \qquad (1.6a)$$

$$\rho \frac{\partial \mathbf{v}}{\partial t} + \rho (\mathbf{v}.\nabla) \mathbf{v} = -\nabla p + \frac{1}{\mu_0} (\nabla \times \mathbf{B}) \times \mathbf{B}, \qquad (1.6b)$$

$$\frac{\partial p}{\partial t} = -(\mathbf{v}.\nabla) p - \gamma p \nabla.\mathbf{v}, \qquad (1.6c)$$

$$\frac{\partial \mathbf{B}}{\partial t} = \nabla \times (\mathbf{v} \times \mathbf{B} - \eta \mathbf{j}). \qquad (1.6d)$$

These are the mass, momentum, energy and induction equations respectively.

If a static equilibrium is considered where $\mathbf{v} = 0$, then the MHD equations reduce to,

$$\nabla \left(p_0 + \frac{B_0^2}{2\mu_0} \right) = (\mathbf{B_0}.\nabla) \frac{\mathbf{B_0}}{\mu_0}. \qquad (1.7)$$

The left hand term of Eq (1.7) is the plasma and magnetic pressure and the right hand term is the magnetic tension force. For a straight magnetic field configuration the magnetic tension is zero. The total pressure p_T is defined as the sum of the plasma pressure p_0 and the magnetic pressure $B_0^2/2\mu_0$. The ratio of the plasma
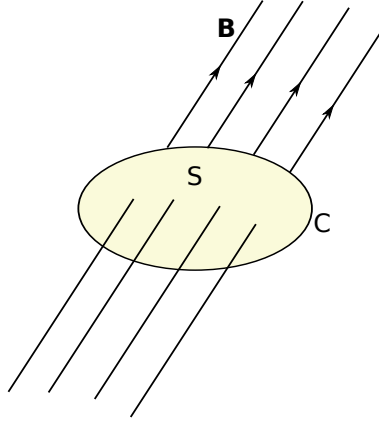
Figure 1.9: Illustration of the flux surface through which magnetic field lines pass.

pressure to the magnetic pressure is called the plasma-β,

$$\beta = \frac{p_0}{B_0^2/2\mu_0}, \tag{1.8}$$

and is a measure of whether a plasma is dominated by the magnetic pressure ($\beta <1$) or by the plasma pressure ($\beta >1$).

1.4.1 Frozen-in flux approximation

An important property of an ideal plasma is the frozen-in flux approximation which states that the number of magnetic field lines passing through any given moving fluid element will remain a constant. This has the consequence that the plasma drags the magnetic field lines along with it, or conversely, the plasma is dragged along by the magnetic field as is the case for a low β plasma such as the solar corona. This approximation is valid in the perfectly conducting limit where the magnetic Reynolds number, defined as the ratio of the convective term $\nabla \times (\mathbf{v} \times \mathbf{B})$ to the diffusive term $\nabla \times (\eta \mathbf{j})$, is much greater than 1 and resistive terms are ignored.
To show that the frozen in flux approximation is true, consider a closed surface S shown in figure 1.9 that moves with the plasma. The flux passing through S is,

$$\Phi = \int_S \mathbf{B} \cdot d\mathbf{A}. \tag{1.9}$$

The flux passing through this surface can change only if the magnetic field strength at a point enclosed by the boundary C changes or if the surface itself changes, leading to either an increase or decrease in the field.
For a change in the magnetic field strength the magnetic flux change is given by,

15

$$\int_S \frac{\partial \mathbf{B}}{\partial t} \cdot d\mathbf{A}. \tag{1.10}$$

For a change in the boundary of the surface consider a piece of the boundary dl moving at a velocity $\mathbf{v}$ past a magnetic field $\mathbf{B}$. The change in the amount of flux enclosed due to this motion integrated over the closed surface is,

$$\oint_C \mathbf{B} \cdot (\mathbf{v} \times d\mathbf{l}) = \oint_C - (\mathbf{v} \times \mathbf{B}) \cdot d\mathbf{l}. \tag{1.11}$$

Therefore the total change in the flux is given by summing Eq. (1.10) and Eq. (1.11),

$$\frac{d}{dt} \int_S \mathbf{B}(\mathbf{r}, t) \cdot d\mathbf{A} = \int_S \frac{\partial \mathbf{B}}{\partial t} \cdot d\mathbf{A} - \oint_C (\mathbf{v} \times \mathbf{B}) \cdot d\mathbf{l}. \tag{1.12}$$

Using Stokes' theorem, the flux due to the motion of the boundary can be rewritten as,

$$\oint_C (\mathbf{v} \times \mathbf{B}) \cdot d\mathbf{l} = \int_S \nabla \times (\mathbf{v} \times \mathbf{B}) \cdot d\mathbf{A}. \tag{1.13}$$

And the total change in the flux is given by,

$$\frac{d}{dt} \int_S \mathbf{B}(\mathbf{r}, t) \cdot d\mathbf{A} = \int_S \left[\frac{\partial \mathbf{B}}{\partial t} - \nabla \times (\mathbf{v} \times \mathbf{B}) \right] \cdot d\mathbf{A}. \tag{1.14}$$

Comparing Eq. (1.14) with the induction equation (1.6d), the right hand side is equal to zero for an ideal plasma so that the total magnetic flux passing through the surface is a constant and the frozen-in flux theorem holds.

1.4.2 MHD waves

Due to their compressibility and elasticity plasmas are able to support a variety of wave modes. These waves can be used to probe the physical properties of a plasma using seismology techniques e.g. coronal seismology (Nakariakov and Ofman 2001). Waves are also able to transfer energy within a plasma which can lead to dissipation and heating if resistive terms are added to the ideal MHD equations. To investigate the basic waves present in a uniform plasma, infinitesimally small Eulerian perturbations are applied to the physical quantities $\rho, p, \mathbf{B}$ and $\mathbf{v}$,

$$\rho = \rho_0 + \rho',$$
$$\mathbf{v} = \mathbf{v}',$$
$$\mathbf{B} = \mathbf{B_0} + \mathbf{B}',$$
$$p = p_0 + p'. \tag{1.15}$$

The subscript 0 indicates equilibrium quantities and the primed quantities are the small Eulerian perturbations. A static equilibrium is assumed so that $\mathbf{v_0} = 0$. Substituting Eq. (1.15) into the ideal MHD equations (1.6) and neglecting nonlinear terms in the perturbation quantities leads to the linearised mass, momentum, energy and induction equations,

$$\frac{\partial \rho'}{\partial t} = -\nabla \cdot \left(\rho_0 \mathbf{v}' \right), \tag{1.16a}$$

$$\rho_0 \frac{\partial \mathbf{v}'}{\partial t} = -\nabla p' + \frac{1}{\mu_0} \left(\nabla \times \mathbf{B_0} \right) \times \mathbf{B}' + \frac{1}{\mu_0} \left(\nabla \times \mathbf{B}' \right) \times \mathbf{B_0}, \tag{1.16b}$$

$$\frac{\partial p'}{\partial t} = - \left(\mathbf{v}' \cdot \nabla \right) p_0 - \gamma p_0 \nabla \cdot \mathbf{v}', \tag{1.16c}$$

$$\frac{\partial \mathbf{B}'}{\partial t} = \nabla \times \left(\mathbf{v}' \times \mathbf{B_0} \right) = -\mathbf{B_0} \nabla \cdot \mathbf{v}' + \left(\mathbf{B_0} \cdot \nabla \right) \mathbf{v}'. \tag{1.16d}$$

To derive a first wave equation, we start with the parallel component of the induction equation,

$$\frac{\partial \mathbf{B}'}{\partial t} \cdot \mathbf{B_0} = -B_0^2 \nabla \cdot \mathbf{v}' + B_0 \left(\mathbf{B_0} \cdot \nabla \right) v_\parallel'. \tag{1.17}$$

We take the time derivative of Eq (1.17) and use the following substitutions,

$$\mathbf{B}' \cdot \mathbf{B_0} = \mu_0 \left(p_T' - p' \right), \tag{1.18}$$

$$\rho_0 \frac{\partial v_\parallel'}{\partial t} = - \left(1_\parallel \cdot \nabla \right) p', \tag{1.19}$$

$$\rho_0 \frac{\partial \nabla \cdot v'}{\partial t} = -\nabla^2 p_T', \tag{1.20}$$

where Eq. (1.18) is a rearrangement of the total pressure perturbation p_T', and Eqs. (1.19) and (1.20) are the parallel component and the divergence of the momentum equation respectively. $1_\parallel$ is a unit vector in the direction parallel to the equilibrium magnetic field.

This leads to an equation in terms of both p' and p_T',

$$\frac{\partial^2}{\partial t^2}\left(p_T' - p'\right) = V_A^2 \nabla^2 p_T' - V_A^2 \left(\mathbf{1}_\parallel \cdot \nabla\right)^2 p'. \qquad (1.21)$$

Taking twice time derivatives of Eq. (1.21) and using the energy equation written in the form,

$$\frac{\partial^2 p'}{\partial t^2} = C_S^2 \nabla^2 p_T', \qquad (1.22)$$

an equation in terms of the total pressure perturbation describing the magnetoacoustic waves is derived,

$$\left[\frac{\partial^4}{\partial t^4} - \left(C_S^2 + V_A^2\right)\frac{\partial^2}{\partial t^2}\nabla^2 + C_S^2 V_A^2 \left(\mathbf{1}_\parallel \cdot \nabla\right)^2 \nabla^2\right] p_T' = 0. \qquad (1.23)$$

C_S and V_A are the sound and Alfvén speeds defined as,

$$C_S = \sqrt{\frac{\gamma p_0}{\rho_0}}, \qquad V_A = \frac{B_0}{\sqrt{\mu \rho_0}}. \qquad (1.24)$$

To derive a second wave equation we begin with the parallel component of Ampère's law,

$$\mu_0 j_\parallel' = \left(\nabla \times \mathbf{B}'\right) \cdot \mathbf{1}_\parallel. \qquad (1.25)$$

Taking a time derivative and substituting the parallel component of the induction equation, Eq. (1.17), leads to,

$$\mu_0 \frac{\partial j_\parallel'}{\partial t} = \nabla \times \left(\mathbf{B_0} \cdot \nabla\right) v_\parallel'. \qquad (1.26)$$

Taking the time derivative of Eq (1.26) and using the curl of the parallel momentum equation,

$$\rho_0 \frac{\partial}{\partial t}\left(\nabla \times v_\parallel'\right) = \left(\mathbf{B_0} \cdot \nabla\right) j_\parallel', \qquad (1.27)$$

leads to the Alfvén wave equation,

$$\left[\frac{\partial^2}{\partial t^2} - V_A^2 \left(\mathbf{1}_\parallel \cdot \nabla\right)^2\right] j_\parallel' = 0, \qquad (1.28)$$

where $j_\parallel'$ is the perturbed parallel current density.

Dispersion relations follow from solutions in the form of a plane wave e.g. $f\left(\mathbf{r}, t\right) = A \exp(i(\mathbf{k}.\mathbf{r} - \omega t))$. Substituting this into Eqs. (1.23) and (1.28) leads to the magnetoacoustic wave dispersion relation,
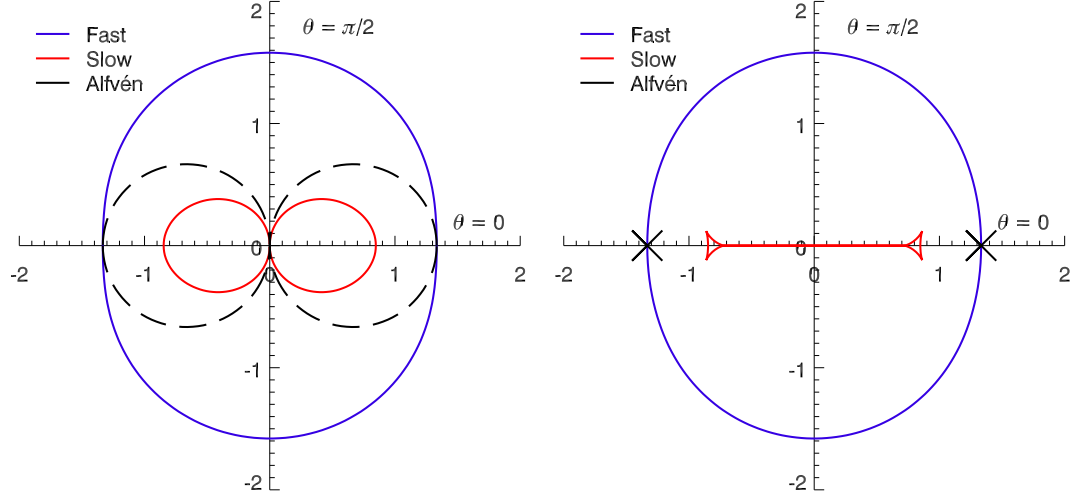
Figure 1.10: *Left*: Phase speed diagram and *Right*: Group speed diagram for the slow, fast and Alfvén waves. The magnetic field is along the x axis and θ is the angle between the k vector and the magnetic field. The figure is drawn for a plasma-β of 0.4.

$$\omega^2 = \frac{1}{2}k^2\left(C_S^2 + V_A^2\right)\left[1 \pm \sqrt{\left(1 - \frac{4C_T^2}{\left(C_S^2 + V_A^2\right)}\frac{k_\parallel^2}{k^2}\right)}\right], \qquad (1.29)$$

where the plus and minus signs denote the fast and slow magnetoacoustic waves respectively, and the Alfvén wave dispersion relation,

$$\omega^2 = V_A^2 k_\parallel^2. \qquad (1.30)$$

C_T is the tube speed defined as,

$$C_T = \frac{C_S V_A}{\sqrt{C_S^2 + V_A^2}}. \qquad (1.31)$$

Figure 1.10 shows the phase and group speeds for the three classes of waves in a homogeneous plasma. Here $\beta < 1$ and the propagation angle θ is the angle between the direction of wave propagation and the direction parallel to the magnetic field so that $k_\parallel = k\cos\theta$. The fast and slow magnetoacoustic waves described by Eq. (1.29) have displacements that are polarised in the plane defined by the wave vector and the equilibrium magnetic field. The fast magnetoacoustic wave is almost isotropic with a slight preference to propagate across magnetic field lines where as the slow magnetoacoustic wave is highly anisotropic and cannot propagate across

19
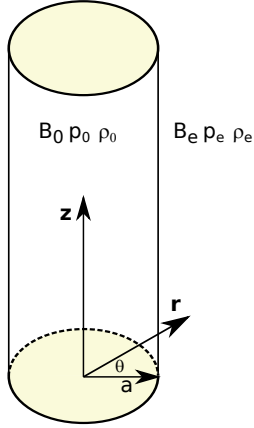
Figure 1.11: Model of a straight magnetic cylinder with radius a. Quantities inside and outside the cylinder are indicated by subscripts 0 and e respectively.

magnetic field lines. Both the fast and slow waves are restored by the plasma and magnetic pressure forces and are compressible. In the limit that β tends to zero, the slow wave vanishes. Alfvén waves described by Eq. (1.30) are incompressible and highly anisotropic, propagating parallel to the magnetic field. As a result of their incompressibility they have no density or pressure changes associated with their propagation. The driving force of the Alfvén wave is the magnetic tension force. The group speed diagram shows the highly anisotropic nature of the slow and Alfvén wave energy which only propagates parallel to the magnetic field compared to the isotropic nature of the fast wave energy.

1.4.3 MHD waves in a plasma cylinder

In the previous section the ideal MHD wave modes in a uniform plasma were introduced, namely the Alfvén wave and the slow and fast magnetoacoustic waves. In contrast however the solar coronal plasma is inhomogeneous and contains magnetic structures such as coronal loops which are denser than their surroundings and act as waveguides. Wave modes of a straight magnetic cylinder have been investigated analytically by Edwin and Roberts (1983) and this discussion follows their work. In their analysis they model a coronal loop as a straight magnetic cylinder with radius a and a magnetic field $B_0\hat{z}$ that is embedded in a magnetic environment with magnetic field $B_e\hat{z}$. The straight cylinder model is shown in figure 1.11. For a straight magnetic cylinder, pressure is balanced at the boundary and Eq. (1.7) implies that,

$$p_0 + \frac{B_0^2}{2\mu_0} = p_e + \frac{B_e^2}{2\mu_0},\tag{1.32}$$

where subscript 0 in this and subsequent equations implies quantities inside the cylinder and subscript e quantities outside the cylinder.

Assuming cylindrical geometry (r, θ, z) and linear perturbations of the form,

$$p'_T(\mathbf{r}, t) = \widetilde{p}_T(r_\perp) \exp i(\omega t + n\theta + kz), \tag{1.33}$$

Eq. (1.23) and Eq. (1.28) reduce to,

$$\frac{d^2 \widetilde{p}_T}{dr^2} + \frac{1}{r} \frac{d\widetilde{p}_T}{dr} - \left(m_0^2 + \frac{n^2}{r^2}\right) \widetilde{p}_T = 0, \tag{1.34}$$

where

$$m_0^2 = \frac{\left(k^2 C_{S0}^2 - \omega^2\right)\left(k^2 V_{A0}^2 - \omega^2\right)}{\left(C_{S0}^2 - V_{A0}^2\right)\left(k^2 C_{T0}^2 - \omega^2\right)}. \tag{1.35}$$

m_0 is the radial wavenumber which depends on the frequency of the wave. Equation (1.34) is a Bessel equation satisfied by $\widetilde{p}_T$. For a solution bounded on the axis of the cylinder,

$$\widetilde{p}_T = A_0 \begin{cases} I_n(m_0 r) & m_0^2 > 0 \\ J_n(n_0 r) & n_0^2 = -m_0^2 > 0 \end{cases} \tag{1.36}$$

for r<a, where we seek wave solutions that are trapped by the loop wave guide, and

$$\widetilde{p}_T = A_1 K_n(m_e r), \tag{1.37}$$

for r>a. A_0 and A_1 are constants and I_n, J_n and K_n are Bessel functions of order n. m_e is the same as m_0 in Eq. (1.35) but with the 0 subscripts replaced with e. It is assumed that there is no propagation of energy towards or away from the cylinder. The dispersion relations follow from the continuity of the radial velocity component and the total pressure across the cylinder boundary:

$$\rho_0 \left(k^2 V_{A0}^2 - \omega^2\right) m_e \frac{K'_n(m_e a)}{K_n(m_e a)} = \rho_e \left(k^2 V_{Ae}^2 - \omega^2\right) m_0 \frac{I'_n(m_0 a)}{I_n(m_0 a)}, \tag{1.38}$$

for surface waves and

$$\rho_0 \left(k^2 V_{A0}^2 - \omega^2\right) m_e \frac{K'_n(m_e a)}{K_n(m_e a)} = \rho_e \left(k^2 V_{Ae}^2 - \omega^2\right) n_0 \frac{J'_n(n_0 a)}{J_n(n_0 a)}, \tag{1.39}$$

for body waves. The dash denotes a derivative of a Bessel function.

For coronal conditions, $V_{Ae}, V_{A0} > C_{Se}, C_{S0}$ and there are no surface modes, only body modes. Modes with $n = 0$ are cylindrically symmetric modes called sausage
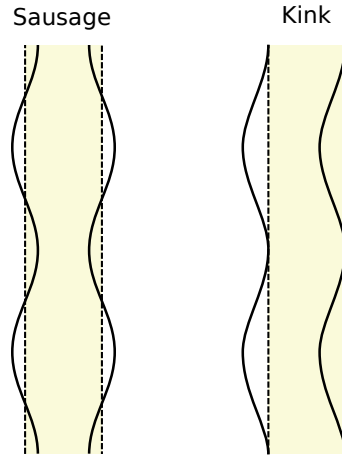
Figure 1.12: *Left:* Symmetric (Sausage) and *Right:* Antisymmetric (kink) perturbations of a straight cylinder.
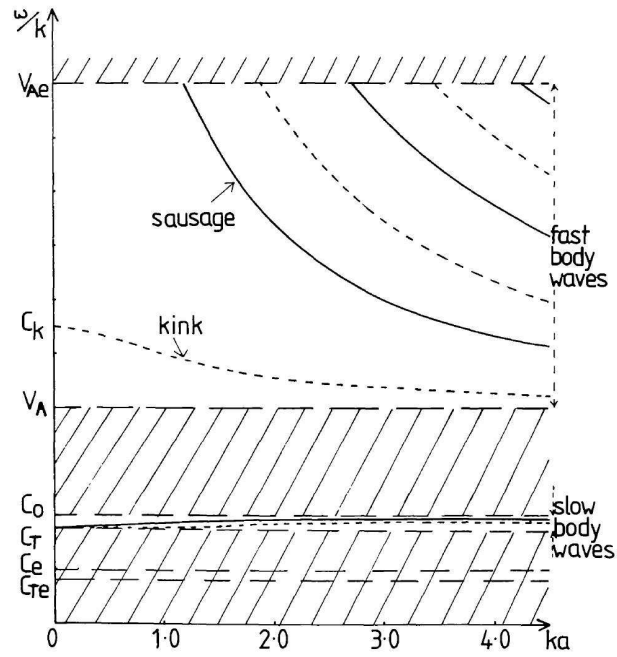
Figure 1.13: Phase speed diagram for waves in a magnetic cylinder under coronal conditions. Taken from Edwin and Roberts (1983).

modes, modes with $n = 1$ are antisymmetric modes called kink modes and modes with $n>1$ are called fluting or ballooning modes. Fast modes only arise if $V_{Ae} > V_{A0}$ and so for coronal parameters of $B_0 = B_e$ and $p_0 = p_e$, fast body waves only occur if the density in the cylindrical structure (ρ_0) is greater than the density of the surrounding corona (ρ_e). In the cylinder model the Alfvén wave is polarised in the azimuthal direction and is located in magnetic flux surfaces (Van Doorsselaere et al. 2008b). This torsional mode does not cause any perturbations of the cylinder axis or cylinder width and therefore does not cause intensity variations. For a cylinder that has a density that varies from the external density to the internal density over a finite width, the Alfvén speed will vary in the radial direction and so neighbouring flux surfaces will oscillate with different frequencies. Therefore the torsional Alfvén wave does not show collective behaviour. Figure 1.12 shows the sausage and kink perturbations of a magnetic cylinder. The fast kink mode is nearly incompressible and is the only mode that displaces the cylinder axis. In contrast the sausage modes do not displace the cylinder axis but they are compressible as they perturb the loop cross section and so cause perturbations in the density. Figure 1.13 shows the phase speed diagram for wave modes under coronal conditions. For long wavelengths all modes except for the sausage mode have a phase speed that tends to the kink speed,

$$C_k = \left(\frac{\rho_0 V_{A0}^2 + \rho_e V_{Ae}^2}{\rho_0 + \rho_e} \right)^{1/2} . \tag{1.40}$$

The fast body modes have a low wave number cut off which implies that only those wavelengths that are shorter than the diameter of a coronal loop can propagate freely.

1.5 Lare2D

To solve the MHD equations and investigate wave behaviour under coronal conditions, numerical codes such as Lare2D (Arber et al. 2001) can be used. Lare2D is a shock capturing Lagrangian remap code that solves the resistive MHD equations in Cartesian geometry. To recap, the set of resistive MHD equations are,

$$\frac{\partial \rho}{\partial t} = -\nabla \cdot (\rho \mathbf{v}),$$

$$\rho \frac{D\mathbf{v}}{Dt} = -\nabla p + \frac{1}{\mu_0} (\nabla \times \mathbf{B}) \times \mathbf{B},$$

$$\frac{\partial \mathbf{B}}{\partial t} = \nabla \times (\mathbf{v} \times \mathbf{B} - \eta \mathbf{j}), \tag{1.41}$$

$$\rho \frac{D\epsilon}{Dt} = -p \nabla \cdot \mathbf{v} + \eta j^2,$$

ϵ is the specific internal energy density and η is the resistivity. To convert between ϵ and pressure/temperature the following relations are used,

$$p = \frac{\rho k_B T}{\mu_m}, \tag{1.42}$$

$$\epsilon = \frac{p}{\rho(\gamma - 1)} = \frac{k_B T}{\mu_m(\gamma - 1)}, \tag{1.43}$$

where μ_m is the reduced mass and $\mu_m = 0.5 m_p$ for fully ionised hydrogen and γ is the specific heat ratio and has a value of $5/3$ under coronal conditions.

The code is second order accurate in space and time and each computational time step is split into two. First, the Lagrangian step during which the resistive MHD equations are advanced in time on a grid that moves with the solution. Next the solutions are remapped onto the fixed Eulerian grid. Lare2D is particularly suited for investigating processes under coronal conditions as it gives an accurate prediction of temperature that can be compared with observations. Obtaining an accurate estimate of the temperature is also an advantage if thermal conductivities or ionisation levels are required since these quantities are sensitive to the temperature. The numerical grid is staggered to prevent the development of the checkerboard instability and is shown in Figure 1.14. Velocities are defined at the cell vertices, scalar quantities and the ignorable magnetic field component are defined at cell centres and the remaining magnetic field components are defined at the cell edges.

The code solves the normalised form of the MHD equations and the dimensionless forms of the length scale, magnetic field and density are defined as,

$$x = L_0 \hat{x},$$

$$\mathbf{B} = B_0 \hat{\mathbf{B}}, \tag{1.44}$$

$$\rho = \rho_0 \hat{\rho},$$

where L_0, B_0, and ρ_0 are user defined values of the normalising length, magnetic field and density respectively. These user defined normalising quantities are used to
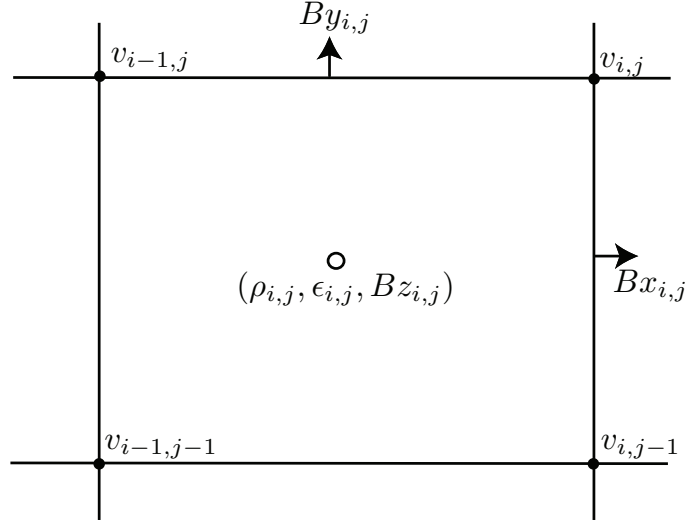
Figure 1.14: The 2D staggered grid.

define the normalisation for the other quantities such as the velocity, pressure and time, e.g.

$$
\begin{aligned}
v_0 &= \frac{B_0}{\sqrt{\mu_0 \rho_0}}, \\
p_0 &= \frac{B_0^2}{\mu_0}, \\
t_0 &= \frac{L_0}{v_0}.
\end{aligned}
\tag{1.45}
$$

The resistivity is defined as $1/S$ and can be uniformly applied or triggered when the current density exceeds a threshold value.

Chapter 2

Transverse loop oscillations

2.1 Transverse loop oscillations

Coronal loops (see figure 1.4), a consequence of the low β coronal plasma, can be perturbed by dynamic events such as CMEs and solar flares. Transverse loop oscillations (TLOs) are the standing modes of coronal loops where the oscillation is perpendicular to the loop axis and they are interpreted as the nearly incompressible fast kink (Alfvénic) mode (Edwin and Roberts 1983). For TLOs the fundamental mode is characterised by the displacement of the loop axis with all parts of the loop in phase (Aschwanden et al. 1999b; Nakariakov et al. 1999). These modes can be horizontally polarised, where the oscillation is perpendicular to the loop plane, vertically polarised where the loop expands and contracts and the oscillation is polarised in the loop plane or even a mixture of the two (Wang et al. 2008). TLOs are impulsively excited and are often assumed to be perturbed by a blast wave directly connected with solar flares (Tothova et al. 2011). Usually TLOs are observed to have their initial displacement away from the source of excitation and then to damp rapidly back to an equilibrium which may or may not be aligned with their initial start position (e.g. Aschwanden et al. 1999b; Verwichte et al. 2004). Figure 2.1 (top) shows a space-time diagram that highlights the oscillation of a coronal loop. The displacement-time profile of the oscillation is extracted and can be analysed by fitting a damped sinusoidal curve to the oscillation.

2.1.1 TLO observations

The first spatial observation of a TLO was made in 1998 using the TRACE EUV imaging satellite. Aschwanden et al. (1999b) observed five oscillating loops with periods in the range of 258 - 320 s. The loops were observed to support an aver-
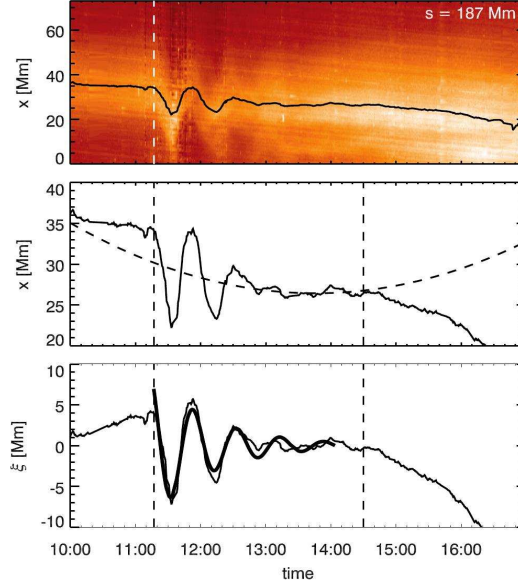
Figure 2.1: *Top*: Space-time diagram of an oscillating loop that highlights the transverse oscillation. *Middle* and *Bottom*: The displacement-time curves of the oscillation extracted from the space-time image. The oscillation is analysed by fitting a damped cosine curve to the profile. The TLO is observed to damp very rapidly i.e. within a few oscillation periods. Figure from Verwichte et al. (2010).

age of 3.4 oscillation periods and were found to oscillate almost in phase with one another, indicating a simultaneous excitation. Nakariakov et al. (1999) analysed a single loop from the same event with an oscillation period of 256 s and damping time of 870 s. They paid particular attention to the rapid damping of the oscillation, suggesting that it may be a result of viscous and resistive dissipation. Using the observational results they deduced that the Reynolds and Lundquist numbers must be approximately eight and seven orders of magnitude smaller than their corresponding classical values respectively. The Reynolds (R) and Lundquist (S) numbers are defined as,

$$R = \frac{Lv}{\nu}, \tag{2.1}$$

$$S = \frac{LV_A}{\eta}, \tag{2.2}$$

where L is a global length scale, v is a typical flow velocity, V_A is the Alfvén velocity, ν is the kinematic viscosity, and η is the resistivity.

The initial observations were closely followed by a comprehensive study of 17 TRACE events occurring between 1998 and 2001 in which impulsive transverse oscillations of loops were observed after flare eruptions (Schrijver et al. 2002). It was noted that roughly only 6% of all the flares observed by TRACE had oscillating loops associated with them. From the 17 TRACE events, the oscillation parameters of 26 loops were studied in greater detail (Aschwanden et al. 2002) and oscillation periods of 137 - 694 s and damping times of 191 - 1246 s were reported. One of the TRACE events occurring on 15 April 2001 was the subject of a detailed study by Verwichte et al. (2004). In their paper they study 9 loops of a post-flare loop arcade that show transverse oscillations after a nearby prominence eruption. They find oscillation periods in the range of 200 - 450 s and damping times in the range of 800 - 1800 s, consistent with the results from Aschwanden et al. (2002). In most cases TLOs are horizontally polarised so that they appear to sway back and forth perpendicular to the loop plane. However there are two examples where TLOs displaying vertically polarised oscillations were observed. Coronal loops oscillating transversely and polarised in the loop plane were first reported by Wang and Solanki (2004). This vertically polarised TLO was observed on the solar limb and confirmed by comparing simulations of a synthetic loop oscillating in both horizontal and vertical polarisations with the TRACE images. A second vertically polarised TLO, again on the solar limb, was observed after the failed eruption of a filament (Mrozek 2011).

Other studies of TLOs include observations of multiple harmonics of loop oscillations (e.g. Verwichte et al. 2004; Van Doorsselaere et al. 2007; De Moortel and Brady 2007) and of transverse oscillations in cooling loops (Aschwanden and Terradas 2008). The longest displacement time period reported by Aschwanden et al. (2002) was less than 12 minutes, however a significantly longer period of 40 minutes was detected in a loop with a length of approximately 690 Mm by TRACE and the Extreme ultraviolet Imaging Telescope (EIT) on the Solar and Heliospheric Observatory (SOHO) (Verwichte et al. 2010). The displacement-time profile of the loop oscillation is shown in figure 2.1. TRACE was unable to observe the whole loop due to its limited field of view, however EIT was able to provide full disk observations with a cadence of 12 minutes. In this event intensity variations are observed along the loop that are in phase and have comparable periods with the displacement time series. Intensity variations that are in anti-phase with the displacement time series are also found at the loop footpoints. In this case the authors conclude that the intensity variations are most likely due to line of sight effects where the column depth of the loop, and so the observed intensity, varies as the loop undergoes a transverse

oscillation. However an alternative explanation for the intensity variations observed at the loop footpoints was put forward by Terradas et al. (2011) who suggested that they may be a result of linear coupling between the fast and slow waves due to reflection from the photosphere. Intensity variations associated with vertically polarised TLOs were reported by Wang and Solanki (2004). Here the intensity was seen to increase as the loop contracted, however the intensity amplitude was larger than expected if mass conservation is taken into account and assuming a constant loop cross section. The first example of a TLO event that showed clear intensity oscillations was studied simultaneously by both the STEREO A and B space craft (Verwichte et al. 2009). The intensity oscillations were found to be in phase with the loop displacement and were concluded to be the result of line of sight effects.

The first detailed observation of a TLO by the Atmospheric Imaging Assembly (AIA) on SDO was made by Aschwanden and Schrijver (2011). In this work they observed approximately 3.6 oscillation periods of a multi-stranded cool loop where the temperature of the loop T $\approx$ 0.5 MK. An oscillation period of 376 s was found but unusually no decay in the amplitude was observed. Wang et al. (2012) observed TLOs of a multi-stranded loop in three AIA bandpasses, 171 Å, 193 Å and 211 Å. The strands seen in 171 Å were found to have growing amplitudes suggesting that the kink oscillations in this loop are forced. The strands seen in 193 Å also showed interesting behaviour as they developed a quarter period phase delay between them, demonstrating evidence of collective loop behaviour. The normal modes of two coronal loops separated by a distance d has been studied numerically by Luna et al. (2008) in order to investigate their collective oscillatory behaviour. Recently TLOs were observed during a solar flare implosion event by Simões et al. (2013). In this case four coronal loops seen in the 171 Å, 131 Å, 193 Å and 211 Å AIA bandpasses are observed to undergo inwardly directed (towards the flare source region) oscillatory motion that is explained due to the reduction in the magnetic pressure force.

Nisticò et al. (2013a) showed both decaying and decay-less oscillations in the same loop with typical oscillation periods between 200 - 300 s and a typical decay time of 500 s. They concluded that the two different oscillation regimes are excited by a large amplitude impulsive driver in the case of the large amplitude decaying oscillations and an external non-resonant harmonic driver in the case of the low amplitude decay-less oscillations. Low amplitude (0.12 - 0.39 Mm) decay-less oscillations in four loops detected by AIA with periods between 260 - 620 s have also been observed

by Anfinogentov et al. (2013). The oscillations were detected in loops emerging from a non flaring active region and were interpreted as fundamental kink modes.

Although the majority of TLOs have been observed using EUV imaging instruments these waves have also been detected in spectral data with instruments such as the Extreme-Ultraviolet Imaging Spectrometer (EIS) (Culhane et al. 2007) on the Japanese satellite Hinode (Kosugi et al. 2007). EIS has both spectroscopic and imaging capabilities and has been utilised by Van Doorsselaere et al. (2008b) to obtain oscillatory and density information of a TLO. The transverse oscillation with a period of 300 s does not display any significant damping during the observation, similar to the TLO observed by Aschwanden and Schrijver (2011). The first observation of both transverse and longitudinal modes simultaneously excited in a coronal loop was observed by the ground based Norikura Green-Line Imaging System (NOGIS) at the Norikura Solar Observatory, National Astronomical Observatory of Japan (Hori et al. 2007). NOGIS is a 2D Doppler chronograph and measures the line of sight velocity in the Fe XIV (5303 Å) line which corresponds to a temperature of 2 MK. Multiple loops on the solar limb triggered by a CME were studied and a particular loop was found to oscillate with a period of 15.7 minutes and a damping time of 70 minutes. The oscillation was interpreted as a standing kink mode because it was not observed in the intensity variation, suggesting an incompressible oscillation, and due to its phase velocity measured as 811 kms^{-1}. TLOs have recently been associated with coronal rain, cool dense plasma seen in chromospheric lines such as Hα which appears to rain down along magnetic field lines (Antolin and Verwichte 2011). It is not clear whether the coronal rain is the cause of the TLOs observed in the loop strands, however the oscillations are only easily visible in this observation because of the cool plasma rain.

2.1.2 TLO damping

With the exception of a few cases e.g. Aschwanden and Schrijver (2011), a key feature of transverse loop oscillations is that they decay over short timescales so that only a few periods are observed before the oscillation is no longer visible above the noise level. This feature is important to study as it indicates possible heating and energy transfer into the corona. Mechanisms proposed to explain this rapid damping are phase mixing (Heyvaerts and Priest 1983), resonant absorption (Hollweg and Yang 1988; Goossens et al. 2002), wave leakage and damping due to cooling. Lateral wave leakage has been shown to be an efficient damping mechanism for vertically polarised TLOs from numerical (Brady and Arber 2005) and analytical (Verwichte

et al. 2006b) studies of a curved magnetic slab. The ratio between the damping time and the period (τ/P) of a vertically polarised TLO observed by Wang and Solanki (2004) was found to be 3.05, compared to the numerical result of 0.12 and the analytical result of 0.2-0.9. Although there is good correspondence between the simulation and the model, the ratios are significantly smaller than the observed value. In the simulations the effects of gravity are neglected and it was noted that detailed information on the internal loop structure is needed in order to fully investigate the effect of wave leakage. It was also pointed out by Verwichte et al. (2006b) that due to a data gap in the observation only 1.5 oscillation periods are observed and the damping time may be too long. They suggest that the damping time may be as short as 200 s (although it is expected to have large errors associated with it) which gives a minimum value of τ/P of 0.85, much closer to the analytical result. Wave leakage through loop footpoints due to chromospheric damping has been investigated by De Pontieu et al. (2001). Observations of cooling loops have shown that the cooling plasma can influence the oscillation properties of kink modes particularly for periods around 300s (Morton and Erdélyi 2009). Damping due to cooling was only shown to be significant on cooling timescales of approximately 900 to 2000s and the observed damping may not be completely accounted for by cooling.

2.1.3   Phase mixing and resonant absorption

Phase Mixing

Alfvén wave phase mixing as described by Heyvaerts and Priest (1983) is a mechanism for dissipating wave energy in an inhomogeneous medium and can be thought of as friction between neighbouring field lines. Equilibrium quantities, such as the density, vary in the direction perpendicular to the magnetic field which causes the Alfvén speed to vary on each field line. As a result, the wave fronts of the propagating Alfvén waves become out of phase and form large gradients in the perpendicular direction, leading to enhanced dissipation. This enhanced dissipation was initially suggested as a possible source of coronal heating in open magnetic structures with the idea being that the kinetic energy stored in the Alfvén waves is converted into heat. The effect of Alfvén wave phase mixing in a stratified open atmosphere has been investigated by De Moortel et al. (1999). Here the density was stratified in both the horizontal and vertical directions and it was found that wavelengths lengthen as the waves propagate through the plasma compared to the case with no vertical stratification. Even though phase mixing by ohmic heating was found to be less efficient at heating the corona with vertical stratification, the total energy deposited

in the plasma was not affected. For the case of strong phase mixing where the horizontal density stratification is large, it was shown that vertical stratification of the density is unimportant. This work was extended by De Moortel et al. (2000a) by including a radially diverging background magnetic field in addition to the vertical density stratification. The radially diverging magnetic field causes wavelengths to shorten as they propagate outwards, making the phase mixing more efficient as small length scales build up faster allowing the waves to be dissipated more quickly. However, for sufficiently small values of the scale height the vertical stratification of the density dominates and phase mixing is less efficient than for a non stratified atmosphere. In the context of transverse loop oscillations, adjacent coronal loops may damp via phase mixing since the Alfvén speed depends on the local density and magnetic field strength which can differ between loops. Alternatively coronal loops are often assumed to be multi-stranded structures (Schmelz et al. 2010; Brooks et al. 2012). Neighbouring loop strands may have different oscillation frequencies due to local density fluctuations, leading to large gradients and dissipation. Phase mixing was suggested as the dissipation mechanism to explain the rapid damping observed in 11 TRACE TLOs by Ofman and Aschwanden (2002) and is not ruled out as the damping mechanism for another set of TRACE observed TLOs (Verwichte et al. 2004). Ofman and Aschwanden (2002) show that for phase mixing the damping time t_d follows the scaling law,

$$t_d \sim P^{\frac{4}{3}}, \tag{2.3}$$

where P is the oscillation period. They find a scaling power of 1.30 ± 0.2 that is in good agreement with the scaling law for phase mixing, however they ignore two outlying data points.

Resonant absorption

Another consequence of an inhomogeneous plasma is resonant absorption (Ionson 1978; Hollweg and Yang 1988; Sakurai et al. 1991; Ruderman and Roberts 2002). A coronal loop can be modelled as a straight plasma cylinder with a thin inhomogeneous layer (figure 2.2) where the density transitions linearly from the outside density to the internal loop density. There exists a continuum of Alfvén frequencies which vary between the Alfvén frequency inside the tube and outside the tube, and within this Alfvén continuum there exits discrete global fast magnetoacoustic modes. For strong gradients in the density (and so frequency) the fast magnetoa-
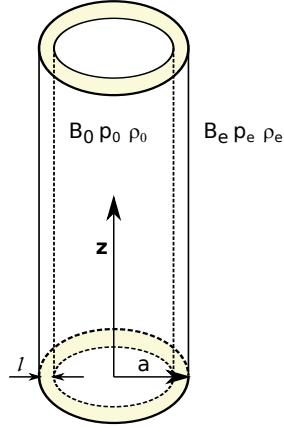
Figure 2.2: Model of a straight magnetic cylinder with a radius a and an inhomogeneous layer of width l. Quantities inside and outside the cylinder are indicated by subscripts 0 and e respectively.

coustic wave mode converts efficiently to the Alfvén wave. The fast magnetoacoustic kink mode can be considered as a global mode in the plasma structure and the Alfvén wave can be considered as a local wave on a magnetic flux surface. The frequency of the magnetoacoustic wave has to match that of the Alfvén frequency in order for mode conversion to occur. Once the fast magnetoacoustic wave has undergone mode conversion, the Alfvén wave can then form large gradients and dissipate via phase mixing. In non uniform plasmas MHD waves can often have mixed properties (Goossens et al. 2011). This leads to an alternative explanation of resonant absorption in terms of the damping of quasi-modes, rather than a global kink wave undergoing mode conversion to an Alfvén wave (Goossens et al. 2002). Quasi-modes are produced by fast discrete eigenmodes that have an eigenfrequency in the Alfvén continuum which couple to the local continuum eigenmode. Efficient conversion of the kinetic energy of the radial motions of a global fast (kink) mode to the kinetic energy of the azimuthal motions of local continuum Alfvén modes causes the quasi-modes to be damped. Lastly the Alfvén continuum oscillations are converted into heat by dissipative processes.

For a fundamental kink mode Ruderman and Roberts (2002) obtain an oscillation decay rate due to resonant absorption of,

$$\frac{\tau_d}{P} = \frac{2}{\pi} \frac{a}{l} \frac{\rho_i + \rho_e}{\rho_i - \rho_e}, \tag{2.4}$$

where a is the mean loop width and l is the width of the loop inhomogeneous layer.

The factor of $2/\pi$ indicates that there is assumed to be a sinusoidal variation in the density across the non uniform layer. By assuming that ρ_i is much greater than ρ_e and a/l is constant, Ofman and Aschwanden (2002) derive a scaling law of,

$$t_d \sim P, \qquad (2.5)$$

for the fundamental kink mode. The scaling power of 1.30 ± 0.21 found by Ofman and Aschwanden (2002) therefore appears to favour phase mixing over resonant absorption as the damping mechanism. In contrast Nakariakov and Verwichte (2005) obtain a scaling power of 1.12 ± 0.36 by including two further observations from Wang and Solanki (2004) and Verwichte et al. (2004). In this case resonant absorption appears to be the favoured damping mechanism, but phase mixing cannot be ruled out and a larger sample size is needed to further investigate the damping mechanism of transverse loop oscillations. It has been questioned whether scaling laws are able to discriminate between different damping mechanisms when coronal loop quantities such as a/l and the density contrast are unavailable from the observations (Arregui et al. 2008). The scaling law, Eq. (2.5), derived from Eq. (2.4) assumes that the right hand side is constant implying that all TLO events occur in identical loops. This is unlikely to be the case and will lead to a spread of the data. Using data produced by Eq. (2.4), Arregui et al. (2008) also demonstrate that almost any scaling law can be obtained for the damping mechanism of resonant absorption.

2.2 Coronal seismology

Coronal seismology, is a powerful technique that links observable quantities, such as the period and damping times of kink waves in coronal loops, to unknown quantities such as the magnetic field strength which is difficult to determine directly due to the thermal broadening of spectral emission lines. It was originally suggested by Uchida (1970) in the context of global waves and has since been applied to local wave modes (Edwin and Roberts 1983) such as kink and sausage waves. Transverse loop oscillations are particularly suited to this seismology technique as their periods, damping times and wavelengths can be reliably measured from EUV observations. For a fundamental TLO with a loop length L and period P, the phase speed is V_{ph} = $2L/P$. In the thin tube limit, $ka \ll 1$, the phase speed of the fast kink mode is (Nakariakov and Ofman 2001),

$$\frac{\omega}{k} \approx C_k \equiv \left(\frac{2}{1 + \rho_e/\rho_0}\right)^{1/2} V_{A0}. \tag{2.6}$$

Both the density contrast (ρ_e/ρ_0) and the internal Alfvén speed V_{A0} are unknown quantities. Since the Alfvén speed is dependent on the magnetic field strength, Eq. (2.6) can be written in terms of the magnetic field strength and the observables L and P,

$$B_0 = \frac{\sqrt{2\mu_0}L}{P}\sqrt{\rho_0\left(1 + \rho_e/\rho_0\right)}. \tag{2.7}$$

The density contrast between the external and internal plasma takes a value between 0 and 1 and in their initial analysis Nakariakov and Ofman (2001) assume a density contrast between 0 and 0.3 and obtain a range of magnetic field strengths between 4 - 30 G. For the loop studied in detail by Nakariakov et al. (1999) a loop top density was estimated as $10^{9.3}$ cm^{-3} leading to a magnetic field strength of 13 ± 9 G. Applying this method to other TRACE observations, ranges of 3 - 90 G and 9 - 46 G were found for the magnetic field strength by Aschwanden et al. (2002) and Verwichte et al. (2004) respectively.

Magnetic field estimates can be improved by obtaining a more accurate estimate of the loop length by comparing the loop in two different viewpoints. For example Verwichte et al. (2009) studied a loop using both STEREO A and B spacecraft and obtained an estimate of the magnetic field strength of 11 ± 2 G, consistent with Nakariakov and Ofman (2001). Including density diagnostics from spectroscopy instruments such as EIS on Hinode (Van Doorsselaere et al. 2008b) can also improve the accuracy of coronal seismology as often the biggest error on the magnetic field strength is due to the unknown density contrast.

Aschwanden and Schrijver (2011) found a magnetic field strength of 4 ± 0.7 G for an AIA observed TLO. They attempted to validate this result by comparing it with an average magnetic field strength estimated with a potential field model and found an average field strength of 11 G - three times greater than the seismological value. A more recent study by Verwichte et al. (2013) compared the seismologically determined Alfvén speed from observations of two coronal loops with an average Alfvén speed. The average Alfvén speed was calculated from the magnetic field strength along the loop obtained from a potential field extrapolation and the density determined from the differential emission measure along the loop. They show that

the average Alfvén speed overestimates the seismologically determined Alfvén speed and explains the discrepancy in the magnetic field strength estimate of Aschwanden and Schrijver (2011).

Three dimensional numerical simulations of a loop embedded in a magnetic arcade were performed to compare the magnetic field strength obtained from coronal seismology, i.e. Eq. (2.7), with the magnetic field strength measured in the numerical domain (De Moortel and Pascoe 2009). A fundamental kink mode was excited in the loop by a pressure pulse and a seismologically determined magnetic field range of 15 - 30 G was found. This range significantly differed from the input magnetic field strength range of 10 - 20 G. This discrepancy is not due to the effect of loop curvature which is expected to be small. Pascoe and De Moortel (2014) have shown that an external driver can excite transverse oscillations of a 3D loop embedded in a magnetic arcade where the period is essentially determined by the loop length and the external Alfvén speed rather than the kink speed. This accounts for the discrepancy in the period observed by (De Moortel and Pascoe 2009).

2.3 Coronal seismology using an inversion technique

Another method for determining unknown coronal parameters is a seismological inversion technique that was initially investigated numerically by Arregui et al. (2007) and later analytically under the thin tube, thin boundary approximation by Goossens et al. (2008). This technique combines the MHD theory of kink modes with the assumption that these modes are damped via the mechanism of resonant absorption. This inversion scheme constructs a 3D parameter space which includes information on the ranges of the density contrast, the inhomogeneity length scale and the Alfvén travel time which are compatible with observations. The transverse inhomogeneity length scale is defined as the ratio between the width of the inhomogeneous layer, l, and the mean loop radius measured at the centre of the inhomogeneous layer, R which is related to the loop radius a as $R = a - l/2$. The Alfvén travel time is defined as $\tau_A = L/V_A$.

These techniques have been applied to a selection of eleven TRACE observed loop oscillations initially reported by Aschwanden et al. (2002) and Schrijver et al. (2002) and selected by Ofman and Aschwanden (2002). In the strictest sense the analytic scheme is only valid for thin non-uniform layers ($l/R \ll 1$), which produce a weak damping of the kink mode (Goossens et al. 2008). Van Doorsselaere et al. (2004) compared damping rates of kink oscillations calculated both numerically and analytically for different values of l/R. They found that the analytical expressions for the

damping rate can qualitatively describe the damping of thick non uniform layers, however the results differ by up to 25% compared with the numerical results. Other effects not taken into account by the analytic approximation include the effects of non zero radius and of radial stratification of the period.

2.3.1 Analytical inversion

Analytical inversion seismology presented by Goossens et al. (2008) is derived from the expression for the kink frequency, ω_k, in a straight cylinder with constant magnetic field in the thin tube (TT) approximation,

$$\omega_k = \sqrt{\frac{2B^2}{\mu_0\left(\rho_i + \rho_e\right)}} \frac{\pi}{L}, \tag{2.8}$$

and the expression relating the period (P) and the damping time (τ_d) of kink waves damped by resonant absorption in the thin boundary (TB) approximation (Ruderman and Roberts 2002; Goossens et al. 2002),

$$\frac{\tau_d}{P} = \frac{2}{\pi} \frac{R}{l} \frac{\rho_i + \rho_e}{\rho_i - \rho_e}. \tag{2.9}$$

The kink mode period, P, is computed as $P = 2\pi/\omega_k$. From Eq. (2.8) and Eq. (2.9) a set of equations linking three unknown quantities, ζ, y and z are derived under the thin tube, thin boundary approximation.

Beginning with Eq. (2.8), this is written in terms of P, the internal Alfvén travel time τ_{Ai}, and ζ where ζ is the density contrast defined as ρ_i/ρ_e,

$$P = \tau_{Ai}\sqrt{2}\left(\frac{\zeta + 1}{\zeta}\right)^{1/2}. \tag{2.10}$$

Introducing $y = \tau_{Ai}/P$, Eq. (2.10) can be written as,

$$y = \frac{1}{\sqrt{2}}\left(\frac{\zeta}{\zeta + 1}\right)^{1/2}. \tag{2.11}$$

A second equation is derived by solving Eq. (2.10) for ζ and substituting $y = \tau_{Ai}/P$ so that,

$$\zeta = \frac{2y^2}{1 - 2y^2}. \tag{2.12}$$

A third equation is found by solving the expression for the damping time in Eq. (2.9) for ζ and introducing the quantities $z = l/2R$ and $C = \pi\tau_d/P$ so that,

$$\zeta = \frac{Cz + 1}{Cz - 1}. \tag{2.13}$$

The last equation is found by solving Eq. (2.9) for z such that,

$$z = \frac{1}{C}\frac{\zeta + 1}{\zeta - 1}. \tag{2.14}$$

In summary the set of equations linking ζ, y and z are,

$$y = \frac{1}{\sqrt{2}}\left(\frac{\zeta}{\zeta + 1}\right)^{1/2}, \tag{2.15}$$

$$z = \frac{1}{C}\frac{\zeta + 1}{\zeta - 1}, \tag{2.16}$$

$$\zeta = \frac{2y^2}{1 - 2y^2}, \tag{2.17}$$

$$\zeta = \frac{Cz + 1}{Cz - 1}. \tag{2.18}$$

Observations of TLOs supply values for P and τ_d and therefore a value for the constant $C = \pi\tau_d/P$. A problem with this seismic inversion scheme is that there are three unknown quantities and two observables meaning an infinite number of solutions. Figure 2.3 shows an example of a seismic inversion for a TLO with P = 272 s and τ_d = 849 s (Goossens et al. 2008). It indicates that if one of the three parameters could be accurately measured then the 3D parameter space would collapse to a single solution. To calculate the analytical inversion for a loop, one of the unknown quantities (z, ζ or y) can be varied over a particular range and the remaining two parameters calculated using the set of Eqs. (2.15) - (2.18). For example ζ must take a value between 0 and ∞ and so from Eq. (2.9), for $\zeta = \infty$, z must have a minimum value of $1/C$. The maximum of z is 1 since $l/2R = 1$ represents a fully non uniform loop and so z can be varied between $1/C$ and 1.
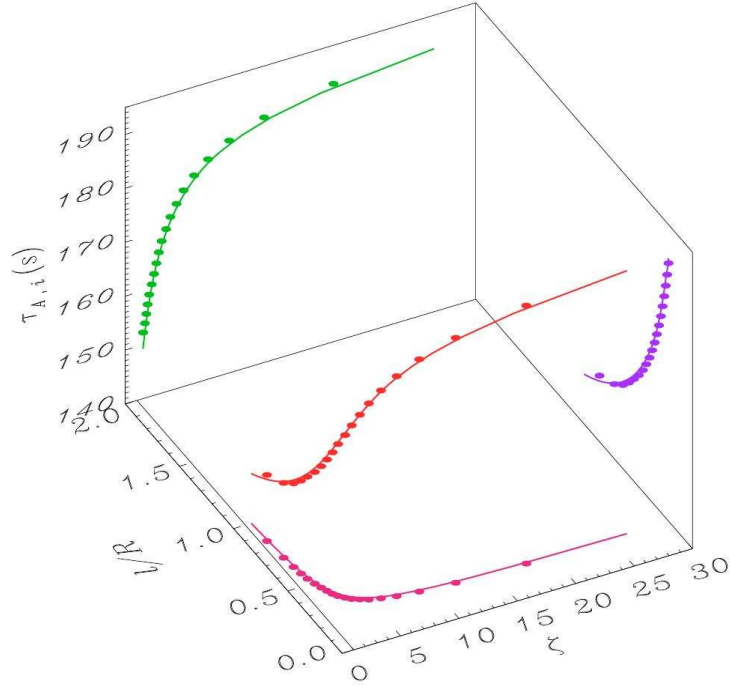
Figure 2.3: Analytic inversion seismology applied to a transverse loop oscillation with $P = 272$ s and $\tau_d = 849$ s (solid lines). The circles are seismological inversion points calculated numerically. Figure from Goossens et al. (2008).

2.4 Magnetic reconnection

Magnetic reconnection is the process by which stressed magnetic field lines undergo restructuring and in the process release energy. The release of energy stored in twisted and stressed field lines leads to plasma heating, particle acceleration and perturbations of plasma structures. These are all processes that can be observed in the solar corona with a particular example being solar flares (Priest and Forbes 2002). Solar flares are an explosive release of energy high up in the corona and indicate a dramatic change in the arrangement of the magnetic field. In 2D models, restructuring of magnetic field lines means that field lines break and reconnect in a narrow region called the diffusion region. This is a region of enhanced current density and large plasma-β ($\beta > 1$), resulting in the breakdown of the frozen-in flux approximation. Steady 2D reconnection is characterised by inwardly moving field lines above and below the diffusion region that reconnect with each other in this region, and then flow out in the horizontal direction. Two models that describe steady state reconnection in 2D are the Sweet-Parker model and the Petschek model shown in figure 2.4. Both models are analytical solutions that match the diffusion
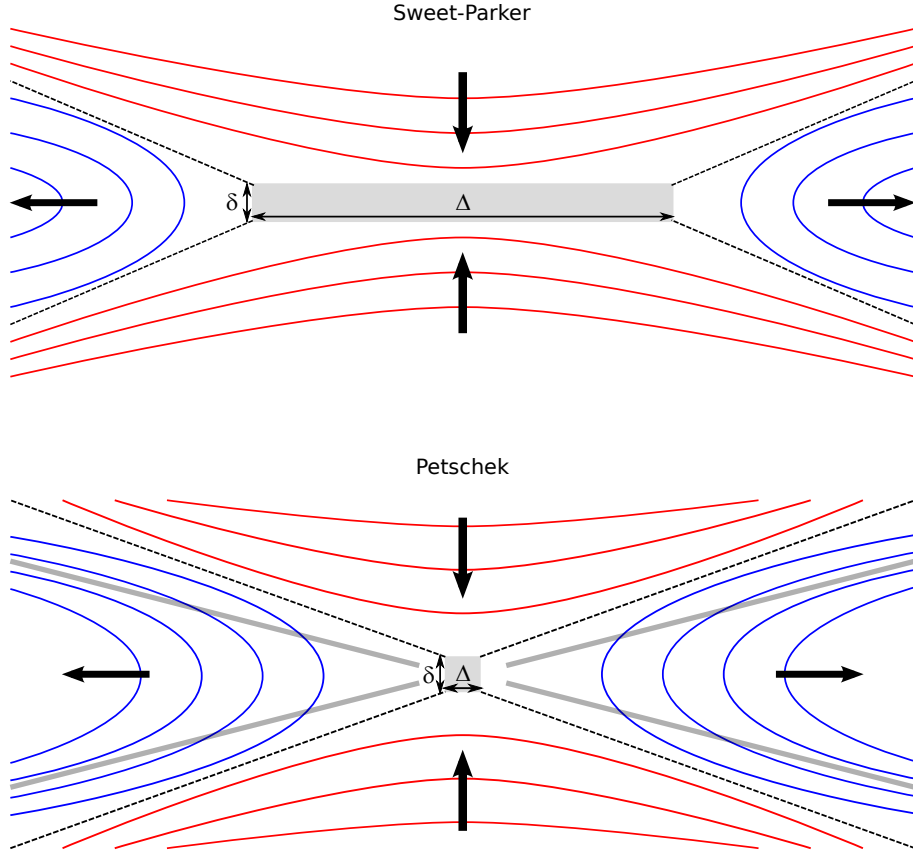
Figure 2.4: The Sweet-Parker and Petschek 2D reconnection models. The Petschek model generates slow mode shocks that are shown as grey strips in the outflow region.

region described by resistive MHD with the area surrounding the diffusion region described by ideal MHD (Aschwanden 2005; Kulsrud 2005).

2.4.1 Sweet-Parker reconnection

The Sweet-Parker model (Sweet 1958; Parker 1963) (top of figure 2.4) is characterised by a diffusion region with a length Δ, that is much greater than its width δ, so that it becomes a long thin current sheet. From the continuity of mass the incoming flux must equal the outgoing flux. Assuming that the density in the inflow and outflow regions are equal the inflow velocity v_{in} can be written in terms of the outflow velocity v_{out} and the dimensions of the current sheet,

$$v_{in} = v_{out} \frac{\delta}{\Delta}. \tag{2.19}$$

The outflow velocity has a speed that is approximately equal to the Alfvén speed

so that plasma is accelerated along the diffusion region and expelled out by the so called 'sling shot effect' due to the magnetic tension force of the strongly bent magnetic field lines leaving the diffusion region. The Sweet-Parker reconnection rate M is,

$$M = \frac{v_{in}}{v_{out}} = \frac{1}{\sqrt{S}}, \qquad (2.20)$$

where S is the Lundquist number defined as,

$$S = \frac{\mu_0 L V_A}{\eta}. \qquad (2.21)$$

S is equal to the magnetic Reynolds number and under coronal conditions is generally large with a value between approximately $10^8 - 10^{12}$. The problem with the Sweet-Parker model is that it produces reconnection times that are too long when compared to the energy release time for a solar flare, which is on the order of minutes to several hours (Aschwanden 2005).

2.4.2 Petschek reconnection

The Petschek reconnection model (Petschek 1964) has a diffusion region that is much shorter $(\Delta \approx \delta)$ compared with the Sweet-Parker model. The Petschek model also generates slow mode shocks in the outflow region, shown in the bottom of figure 2.4, because of the abrupt change from the inflow to the outflow velocities outside the diffusion region. The slow mode shocks are regions where the inflowing magnetic energy is converted to heat and kinetic energy. The reconnection rate given as,

$$M \approx \frac{\pi}{8 \ln S}, \qquad (2.22)$$

is approximately 10^4 times faster than the Sweet-Parker model (for $S = 10^{12}$) and compares much better to the energy release time of solar flares.

2.4.3 X-points and null points

Reconnection occurs in regions of enhanced current density called current layers but where do these regions form in the solar corona? 2D magnetic X-points, points where the magnetic field vanishes, are prone to collapse to form enhanced current density regions and so are obvious sites for reconnection (Pontin 2011). Figure 2.5 is a contour plot showing the 2D X-point for a magnetic field configuration of,

$$\mathbf{B} = \frac{B_0}{L} (y, x), \qquad (2.23)$$
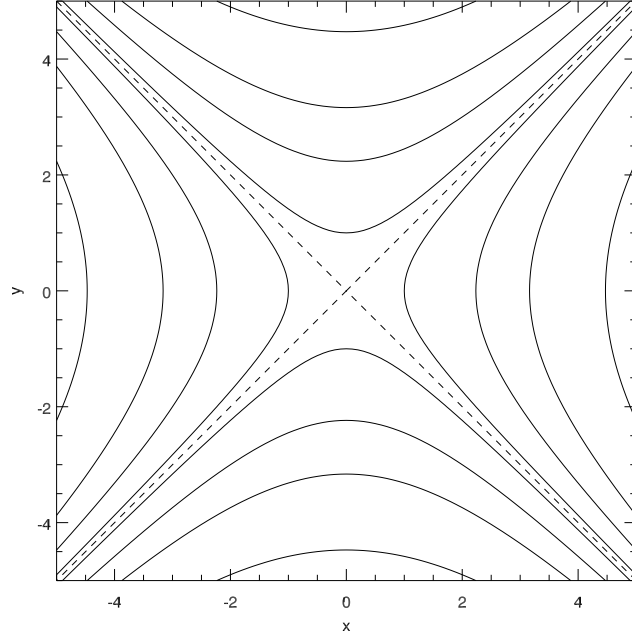
Figure 2.5: 2D X-point configuration. Solid lines are contours of the magnetic field strength and the dashed lines are the separator lines. The magnetic field vanishes at the centre of the X-point

where B_0 is the characteristic field strength and L is the length scale for field variations, both set to 1 in this example. The dashed lines crossing the origin where the magnetic field vanishes are called separator lines and these separate the different regions of magnetic flux. Figure 2.6 is another example of a 2D magnetic topology with an X-point. It shows separator curves running through the X-point that separate different topological regions of magnetic field lines. Topological regions are a collection of field lines that are connected to the same pair of magnetic polarities (Aschwanden 2005).

In 3D, points where the magnetic field completely vanishes are called null points. These are also regions where current layers form and reconnection can take place. Evidence for null points in the solar corona is obtained from magnetic extrapolation of the photospheric magnetic field into the corona. Figure 2.7 shows an example of a 3D null point which is characterised by field lines asymptotically approaching or receding from the null point to form the spine in the y-direction and the fan plane. The fan plane forms the separatrix surface which is the 3D equivalent of the 2D separator curves that separate the different topological regions. Figure 2.8 shows a 3D magnetic topology comprising of two null points separated by a separator
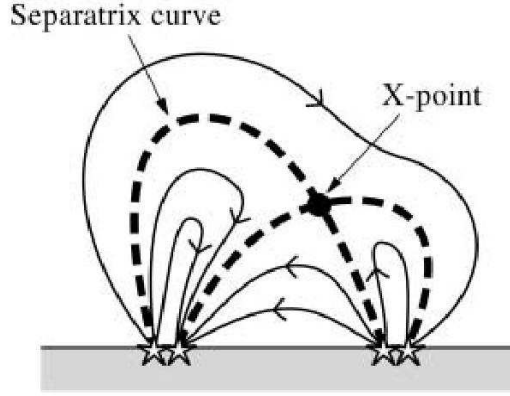
Figure 2.6: Example of a 2D magnetic field configuration with an X-point. Taken from Priest and Forbes (2002)
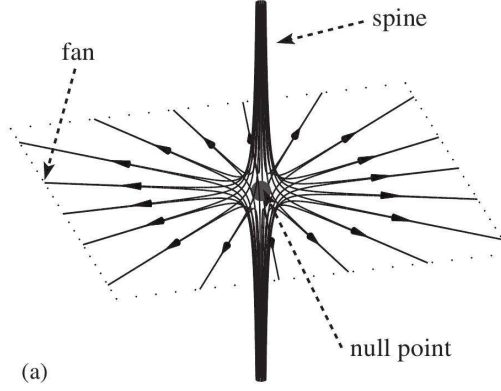
Figure 2.7: Example configuration of a 3D magnetic null point. Taken from Priest and Pontin (2009)

line. This 3D configuration also shows separatrix surfaces (dashed lines) which separate topologically distinct volumes of magnetic flux (Pontin 2011). Separator lines may also collapse to form current layers and so be possible sights of magnetic reconnection.

2.4.4 Magnetic reconnection in 3D

There are three basic regimes for 3D reconnection at a null point. These are torsional spine reconnection, torsional fan reconnection, and spine-fan reconnection (Priest and Pontin 2009; Pontin 2011). In the following discussion of these regimes the null point has the configuration shown by figure 2.7. For the torsional regimes a rotational perturbation is applied to the fan plane (for spine reconnection) or around
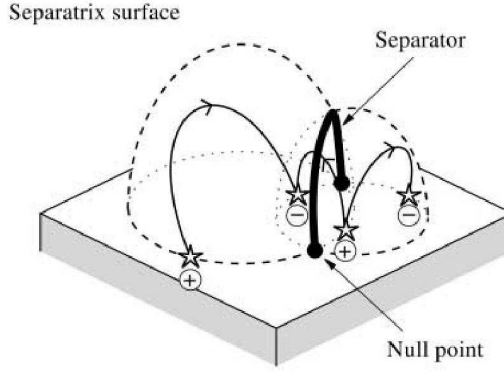
Figure 2.8: 3D configuration showing two null points separated by a separator line. Also shown is the resulting separatrix surfaces. Taken from Priest and Forbes (2002)

the spine (for fan reconnection). This perturbation causes a build up of current due to the newly twisted field lines. For the case of spine-fan reconnection a shear perturbation is applied leading to a collapse of the null point and the formation of a current layer across the spine and fan. In 3D the field lines change their connectivities through rotational slippage where they slip across the current layers and move between different topological regions. 3D reconnection does not require a magnetic null point, only a dense current layer where reconnection can take place. In non null point reconnection models, dense current layers are located at Quasi Separatrix Layers (QSLs) (Démoulin et al. 1996; Démoulin 2006). QSLs are the 3D generalisation of separatrices and are regions where there are strong gradients in the field line mapping. Separatrices are regions where the field line mapping is discontinuous as they represent a strict barrier between different topological regions.

Chapter 3

Transverse coronal loop oscillations seen in unprecedented detail by SDO/AIA

3.1 Introduction

In this chapter the study of eleven coronal loops observed in three events using data from the Atmospheric Imaging Assembly (AIA) on the Solar Dynamics Observatory (SDO) is presented. This study is the first AIA study of multiple loops displaying transverse oscillations in the same active region. The first detailed analysis of a transverse loop oscillation observed by SDO/AIA has been performed by Aschwanden and Schrijver (2011). By studying multiple loops we investigate whether the loops in a single active region have similar properties. We also expand the range of observed periods and damping times. In particular, the capabilities of the AIA instrument allow this range to be extended towards shorter time periods than have previously been observed. Finally, we show that intensity variations in transverse loop oscillations are a common feature. Observations of TLOs have shown variations in intensity with the same periodicity as the loop displacement (Wang and Solanki 2004; Verwichte et al. 2009, 2010; Mrozek 2011; Aschwanden and Schrijver 2011). They have been interpreted as due to variations in the line of sight column depth (Cooper et al. 2003; Verwichte et al. 2009), variations in density from a linearly combined fast kink and slow magnetoacoustic oscillation in a finite plasma-β loop (Terradas et al. 2011), and variations in loop length and/or cross-section in
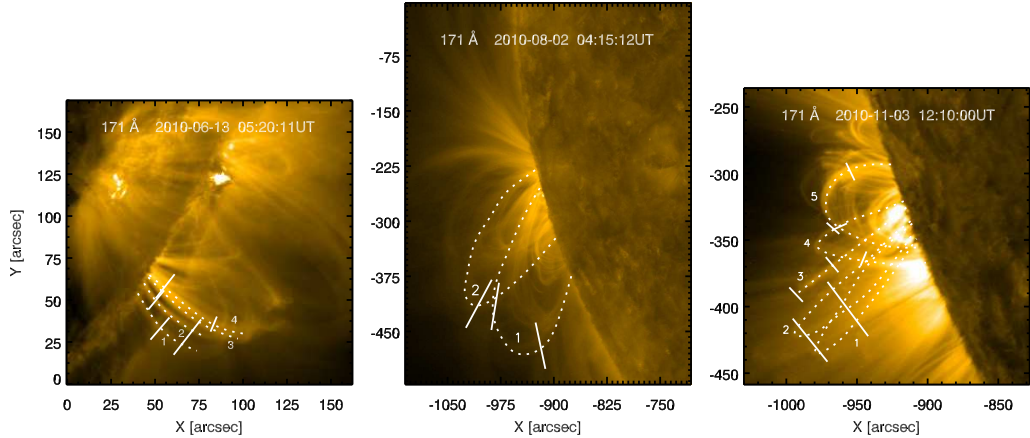
Figure 3.1: SDO/AIA 171 Å images of the three events indicating the loops of interest. Left: Event 1. White tick marks indicate the regions within which cuts are taken to study the oscillations of the four loops. Centre: Event 2 where two larger, fainter loops are studied. The three cuts taken to analyse the oscillations are displayed. Right: Event 3 where five loops are studied. Again white tick marks indicate the regions within which cuts are taken to study the oscillations.

the case of vertically polarised TLOs (Wang and Solanki 2004; Verwichte et al. 2006c; Aschwanden and Schrijver 2011). Non linear coupling of a kink mode to a slow mode also generates density perturbations but which are expected to have a different periodicity (Terradas and Ofman 2004).

3.2 Observations

Data sets from three time intervals from SDO/AIA are studied. Here the primary focus is on the 171 Å bandpass which corresponds to coronal plasma temperatures of approximately 1 MK. All data sets have a time cadence of 12 seconds and are normalised by the exposure time prior to the analysis.

Images of the three events are shown in Figure 3.1. Event 1 was observed between 05:20:11 UT and 06:19:59 UT on June 13th 2010 in active region NOAA 11079 situated on the south west limb. An M1.0 GOES class flare erupted, initially pushing the loops away from the active region and triggering oscillations which were observed to damp within 5 minutes. Four loops indicated in Figure 3.1 are studied. Event 2 was observed between 04:15:12 UT and 05:29:48 UT on August 2nd 2010 in active region NOAA 11095 situated on the south east limb. A dynamic event occurring at approximately (918″E , 261″S) relative to the Sun centre perturbed the loops and

the oscillations of loops indicated in Figure 3.1 are studied. These loops are much larger, have a lower contrast to the background plasma and oscillate more gently than the loops studied in the other two events. Event 3 was observed between 12:10:00 UT and 13:09:48 UT on November 3rd 2010 in active region NOAA 11121. This event has previously been studied by Reeves and Golub (2011); Foullon et al. (2011); Cheng et al. (2011). Following a C4.9 GOES flare and associated CME, transverse loop oscillations are observed, which have not yet been investigated. Of these, five loops are studied which, similar to the other events, display short damping times on the order of 3 to 7 minutes.

Where possible data from SDO/AIA is complemented with data from the Extreme Ultraviolet Imager (EUVI) instrument on board the STEREO spacecraft in the 171 Å and 195 Å bandpasses in order to obtain an estimate of the 3D loop geometry. Comparing the 3D loop geometry also allows an estimate of the loop length to be made. The EUVI instrument observes the Sun in four bandpasses with a pixel size of $1.6''$ and a circular field of view of 1.7 solar radii (Howard et al. 2008).

3.3 Displacement time series analysis

Time series analysis of the transverse coronal loop oscillations is performed by examining image cuts in each of the data sets. Cuts are made across the oscillating loops parallel to the projected displacement direction of the loops. For each cut, a two-dimensional time-distance image is created where the spatial x-coordinate represents the distance along the cut. The cut data has been averaged over the width of the cut, i.e. 11 pixels, to increase signal to noise. Figure 3.1 indicates the regions within which the oscillations are investigated for Events 1 and 3 and the location of the cuts used for the analysis of the loops in Event 2. The number of cuts made in Events 1 and 3 differ for each loop depending on how clear the oscillations are observed.

Loop features in the time-distance images are enhanced by filtering with a two-dimensional continuous wavelet transform using the Mexican hat mother wavelet function (Witkin 1983). The Mexican hat wavelet is the negative Laplacian of a Gaussian shape and enhances intensity ridges in images. It is therefore well suited to enhance the location of solar features including coronal loops (Delouille et al. 2005). The continuous Mexican hat wavelet transform for L_1 norm is defined as,
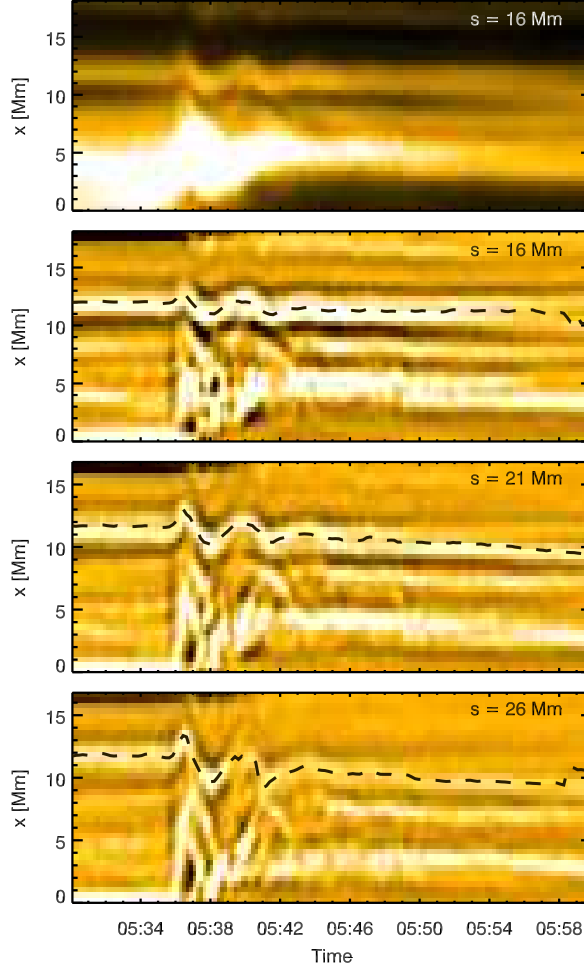
Figure 3.2: Time distance images extracted from cuts taken to analyse loop 2 in Event 1. The top cut shows an example of the time distance images before a 2D Mexican hat wavelet transform has been applied to enhance oscillatory features, as shown by the bottom three cuts. The automatically determined time series from the Gaussian plus background fit for loop 2 has been plotted on the wavelet enhanced cuts.

$$CWT(I)(\vec{b}, a) = -\int_{-\infty}^{+\infty} I(\vec{r})\, \nabla^2 \left(e^{-\frac{|\vec{r}-\vec{b}|^2}{2a^2}} \right) d\vec{r}$$
$$= -\int_{-\infty}^{+\infty} \nabla^2 I(\vec{r})\, e^{-\frac{|\vec{r}-\vec{b}|^2}{2a^2}}\, d\vec{r}\,. \qquad (3.1)$$

From Eq. (3.1) it can be seen that the Mexican hat wavelet transform represents a Gaussian blurring of the Laplacian of the image signal.

Figure 3.2 shows an example of one of the cuts used in the analysis and three time distance images for loop 2 from Event 1 after the application of the wavelet transform. Loop 2, indicated by the dashed line, is clearly visible in the cuts. However, loops 3 and 4 form part of a bundle of loops below loop 2 and are much more difficult to identify due to the overlapping loops and loop strands.

To extract displacement time series information a Gaussian plus second order polynomial function for the background is fitted to each time slice in the time distance images to determine the exact position of the loops. The intensity profile of a loop is well represented by a Gaussian shape (Carcedo et al. 2003). For an isolated loop with no or few interactions with other loops and a high contrast with the background this method is successful in automatically extracting the loop location. However, for many of the loops the time series had to be determined manually by eye. Figure 3.2 shows the automatically determined time series points plotted on the cuts for loop 2 in Event 1. To check that an extracted time series correctly matches to a loop in the SDO data set, a marker is placed on each image corresponding to the determined location of a particular loop. As the images of the event are consecutively displayed, the marker can be observed to follow a loop as it oscillates back and forth. Once the time series has been determined a 3rd order polynomial trend is subtracted from the series and a damped cosine function of the form,

$$\xi(t) = \xi_0 \exp\left(\frac{-(t-t_0)}{\tau}\right) \cos\left(\frac{2\pi}{P}(t-t_0) - \phi\right), \qquad (3.2)$$

is fitted. Where ξ is the amplitude, τ is the damping time, P is the period, ϕ is the phase and t_0 is the reference time. This Levenberg-Marquardt least squares fitting was performed using the function MPFIT (Markwardt 2009) in the Interactive Data Language (IDL). The parameter uncertainties are estimated by scaling the 1 sigma parameter errors computed from the covariance matrix by the measured chi 1/N squared value, assuming that the reduced chi-squared value is one. The error in the loop location is estimated as the width of the Gaussian function fitted to each of the time slices and is approximately one Mm. For manually determined loop locations the Gaussian width is assumed to be one Mm. Figure 3.3 shows the displacement
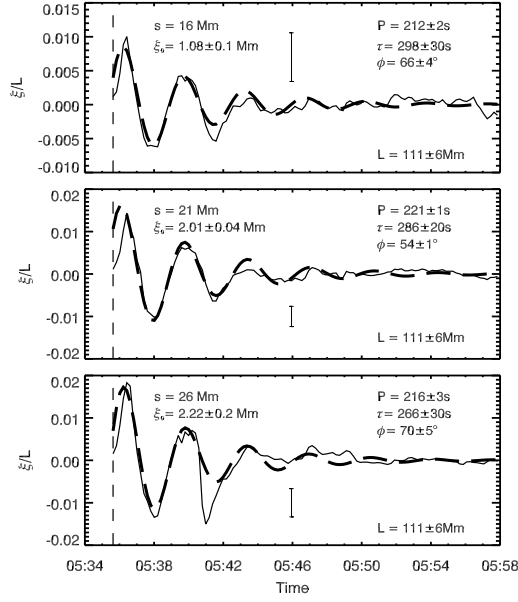
Figure 3.3: Automatically determined time series (solid line) for three of the cuts taken to analyse loop 2 in Event 1 fitted with a damped cosine function (thick dashed line). Top: s = 16 Mm. Centre: s = 21 Mm. Bottom: s = 26 Mm. The errors on the fitting parameters are the errors given by the fitting technique. The error bars on each plot show the typical size of the error in the loop position. The displacement amplitude has been normalised by the loop length. The vertical dashed line indicates the start of the oscillation at $t_0 = 05:35:59$ UT.

time series for loop 2 in Event 1 which has been normalised by the loop length, L, and fitted with the damped cosine curve, Eq. 3.2. The typical size of the error is indicated by the error bars in the figure. The loop length is determined by either assuming that the height of the loop is equal to the radius of a semi circle or by comparing the 3D loop geometry with STEREO as discussed in Section 3.4. It is expected that the error on the loop length is approximately 10% in line with previous studies (Van Doorsselaere et al. 2007). Figure 3.3 shows that the damped cosine function fits well to the period of the oscillation. There is a greater uncertainty in the damping time. This is to be expected because as the oscillation is damped it becomes more difficult to identify peaks and troughs due to the resolution. The time series clearly show that the loop is damped on a short time scale, within a few periods. As the distance along the loop, s, increases towards the apex, the displacement amplitude also increases.

Table 3.1 shows the oscillation parameters determined from the time series analysis of the eleven loops studied in the three events. In some cases the loop oscillations are observed to begin at slightly different times in the time distance images, either

50

because of a slight delay in the excitation at different points along the loop or because the oscillations are not reliably identified until a later time. The amplitudes recorded are the maximum amplitudes determined for each loop from the damped cosine fits. They do not necessarily represent the maximum amplitudes found at the apex position. The errors quoted for the periods, damping times and phases are determined by taking the standard deviation of the parameters obtained in each cut because the values from the different cuts do not lie within each others error bars (Verwichte et al. 2004; Van Doorsselaere et al. 2007). For loop 1 in Event 2 only one cut is analysed therefore the parameter errors quoted are those returned by the parameter fitting technique. Phase speeds are also calculated since $V_{ph} = 2L/P$ for a fundamental of the kink mode where L is the loop length. For the phase speed calculations a 10% error on L was assumed. The loop lengths that have quoted errors have been determined by comparing EUVI with AIA data (see Sect. 3.4). In these cases the error is a measure of the precision of the method repeated several times rather than a measure of the accuracy and so a 10% error was used for the phase speed calculations. For the remaining loops the length has been determined by assuming that the height of the loop is equal to the radius of a semi circle. We now discuss each event in more detail.

3.3.1 Event 1

Three cuts are made to analyse loops 1 and 3, five cuts are made to analyse loop 2 and two cuts are made to analyse loop 4. The periods observed are between 3.5 and 3.75 minutes and the damping times, which are close in value to the periods, show that these loops undergo rapid damping. Problems were encountered when trying to obtain the time series for loops 3 and 4 as these loops appear to be part of a loop bundle consisting of several overlapping loops or loop strands with slightly different periods. To identify these loops and to obtain an estimate of the loop parameters, the method described above of plotting a marker on each of the images was applied. Estimating the loop length from the height of the loop for loops 1, 2 and 4 gives values of 132 Mm, 126 Mm and 132 Mm respectively. This corresponds to percentage differences of 8%, 13% and 16% with the estimates from the EUVI/AIA comparison shown in Table 3.1. Using these lengths, the phase speeds become 1170 ± 240 km s^{-1}, 1170 ± 120 km s^{-1} and 1220 ± 210 km s^{-1} respectively. It is expected that the lengths obtained using the EUVI/AIA comparison are more accurate than those from the height estimates because the loops are observed on the limb and the lengths are determined using information of the 3D loop geometry.

Table 3.1: Displacement oscillation parameters of the eleven loops studied, determined from the damped cosine fitting.

Event	Loop	L (Mm)	θ (°)	t_0 (UT)	P (s)	τ (s)	ϕ (°)	ξ_0 (Mm)	V_{ph} (km s^{-1})
1	1	121 ± 2	38 ± 3	05:35:59	225 ± 40	240 ± 50	150 ± 70	3.26 ± 0.3	1080 ± 220
	2	111 ± 6	26 ± 5		215 ± 5	293 ± 20	69 ± 10	2.76 ± 0.2	1030 ± 110
	3	132	...		213 ± 9	251 ± 40	80 ± 10	1.92 ± 0.1	1240 ± 140
	4	113 ± 4	12 ± 3		216 ± 30	230 ± 20	121 ± 20	4.99 ± 0.3	1050 ± 170
2	1	396	...	04:24:12	520 ± 5	735 ± 50	194 ± 3	1.88 ± 0.1	1520 ± 150
	2	374	...		596 ± 50	771 ± 340	170 ± 30	3.00 ± 0.1	1260 ± 160
3	1	279 ± 3	27 ± 1	12:13:36	212 ± 20	298 ± 30	20 ± 20	5.97 ± 0.3^a	2630 ± 360
	2	240 ± 4	29 ± 1		256 ± 20	444 ± 110	107 ± 20	7.76 ± 0.5^a	1880 ± 250
	3	241	...		135 ± 9	311 ± 90	155 ± 60	3.40 ± 0.4^a	3570 ± 430
	4	159 ± 6	-17 ± 1		107 ± 10	195 ± 10	110 ± 50	2.54 ± 0.3	2970 ± 450
	5	132	...	12:14:36	103 ± 8	242 ± 110	135 ± 30	2.01 ± 0.4	2560 ± 330

[a]Indicates recorded amplitudes that are at the approximate loop apex positions.

3.3.2   Event 2

Two larger loops with periods of just under 10 minutes and damping times of just under 13 minutes are observed. Because of the low contrast of the loops with the background and the gentle oscillations, the results are only obtained from one cut for loop 1 and two cuts for loop 2. Figure 3.4 shows the cuts and the displacement time series fitted with a damped cosine curve for both loops. The error on the loop length is expected to be at least 10% because the height of the loop was difficult to estimate and a comparison with EUVI data could not be performed as the loops are not observed in these images. Periods, damping times, and phases of the two loops are similar to each other. There have been few observations of loops with periods around 10 minutes but the results of Event 2 are consistent with these previous studies (Aschwanden et al. 2002; Verwichte et al. 2009). There are several loops in this event that have not been analysed because of the gentle nature of the oscillations causing oscillation amplitudes that are not large enough to be observed clearly in the time distance images.

3.3.3   Event 3

Five loops are observed and studied. Similar to the other two events strong damping is observed and the phase speeds are noted to be 2-3 times larger than the other two events. Significantly periods of less than two minutes are observed for loops 4 and 5 which is only possible to detect because of the short time cadence of SDO/AIA. Figure 3.5 shows an example cut and corresponding displacement time series for each of the loops in Event 3. The displacement time series shown in the figure are analysed at a slightly later time than the corrected times shown in Table 3.1 so that the best damped cosine fit possible can be achieved. The phase information is then corrected back to the earlier reference time so that it can be compared with the other cuts. All of the loops seem to be close in phase however the corrected time for loop 5 is different from the other loops because the oscillations are observed to begin slightly later. Similar to Event 1, estimates of the length for loops 1, 2 and 4 from assuming the height is equal to the radius of a semi circle gives values of 248 Mm, 264 Mm and 168 Mm. This corresponds to percentage differences of 12%, 10% and 6% respectively with the EUVI/AIA comparison estimates. Using these lengths, the phase speeds are calculated to be 2340 $\pm$ 320 km s^{-1}, 2060 $\pm$ 260 km s^{-1} and 2920 $\pm$ 300 km s^{-1} respectively. Again it is expected that the lengths obtained using the EUVI/AIA comparison are more accurate than those from the height estimates.
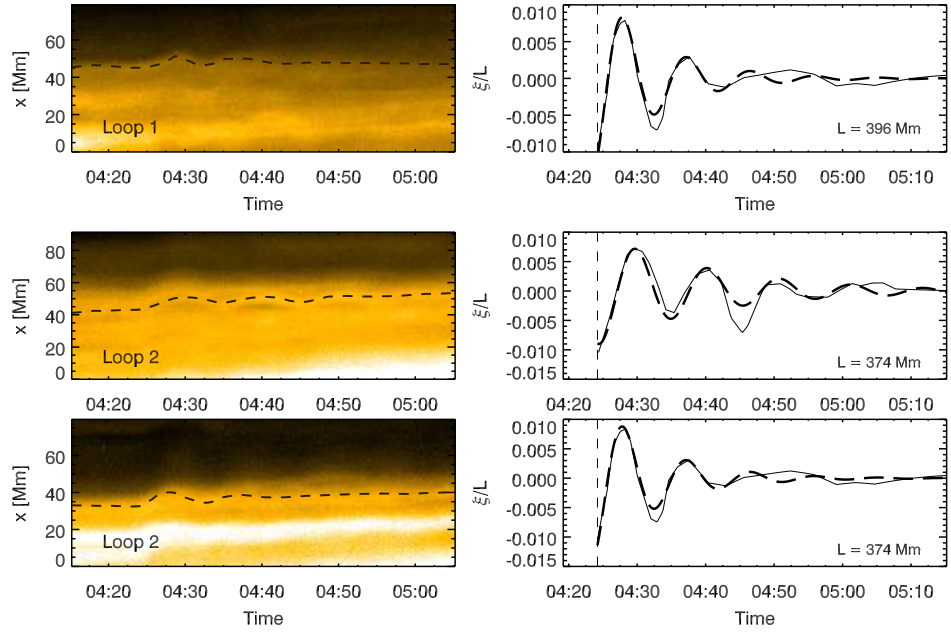
Figure 3.4: Left: Time distance images extracted from cuts taken to analyse the two loops in Event 2. Oscillatory features have not been enhanced with a 2D wavelet function due to the low contrast and gentle nature of the oscillations. The time series determined by eye have been plotted on the cuts. Right: The time series (solid line) determined from the cuts are fitted with a damped cosine function (thick dashed line). The displacement amplitude has been normalised by the loop length. The vertical dashed line indicates the start of the oscillations at $t_0 = 04{:}24{:}12$ UT.
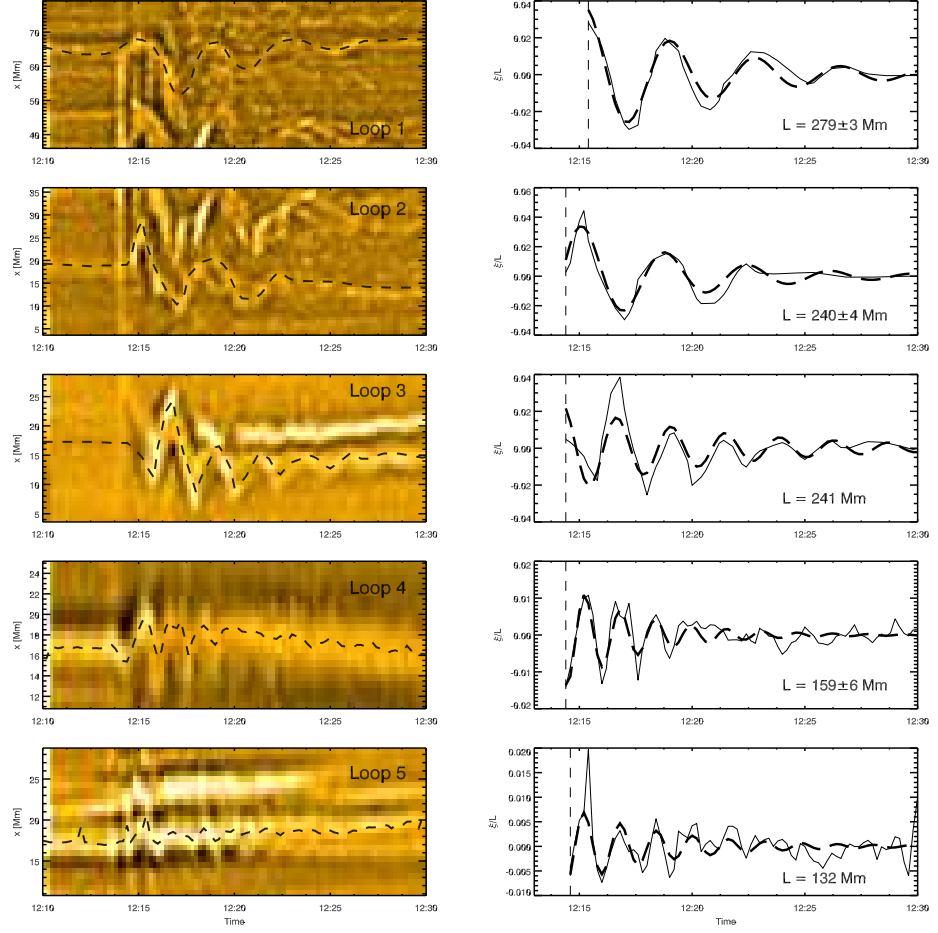
Figure 3.5: Left: Example time distance images extracted from cuts taken to analyse the loops in Event 3. Oscillatory features have been enhanced by applying a 2D wavelet function to the cuts. The time series determined by eye for loops 1, 2, and 3 and the automatically determined time series for loops 4 and 5 from the Gaussian plus background fit have been plotted on the cuts. Right: The time series (solid line) are fitted with a damped cosine function (thick dashed line). The displacement amplitude has been normalised by the loop length. The vertical dashed line indicates the start of the oscillations in the cuts.
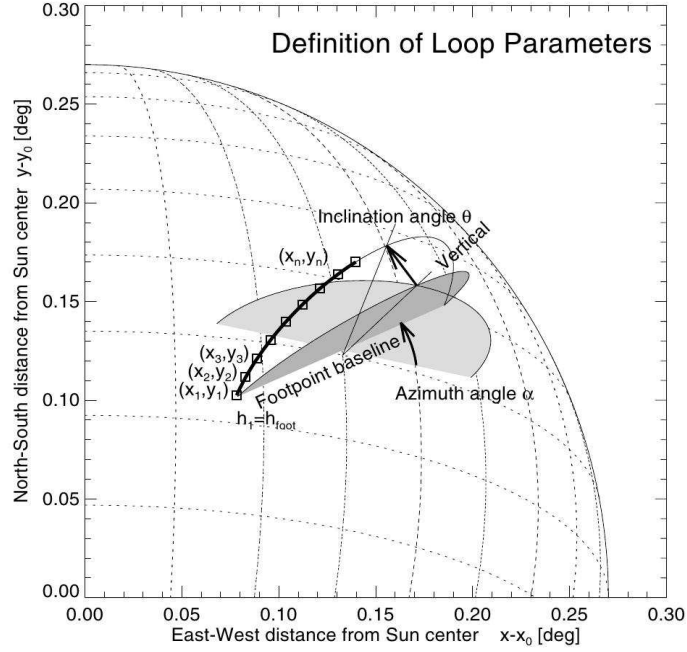
Figure 3.6: Figure showing 2D projected loop parameters as seen on solar image data. θ is the inclination angle, α is the azimuthal angle and (x_i, y_i) are the image coordinates relative to the disk centre in degrees. Taken from Aschwanden (2005).

3.4 Comparison of STEREO/EUVI and SDO/AIA

A comparison is made between STEREO/EUVI and SDO/AIA data to determine where possible the 3D loop geometry and to simulate the polarisation of the kink mode. We construct a three dimensional loop model from the two dimensional projected loop coordinates by assuming a planar loop, which is inclined with respect to the photospheric normal by an angle θ (Verwichte et al. 2010). Figure 3.6 shows 2D projected loop parameters of a planar loop as seen on solar image data.

2D Image coordinates, X_i, Y_i of a projected loop path where $i = 0 \ldots N$ are found relative to the disk centre (X_c) in units of the solar radius, $x_i = (X_i - X_c)/R_S$ and $y_i = (Y_i - Y_c)/R_S$. R_S is the radius of the Sun in pixels. The vectors at the two loop footpoints where $i = 0$ and $i = N$ are,

$$
\begin{aligned}
\mathbf{r_I} &= (x_0, y_0, z_0) \\
\mathbf{r_{II}} &= (x_N, y_N, z_N) \,,
\end{aligned}
\tag{3.3}
$$

where

$$z_0 = \sqrt{\left(1 - x_0^2 - y_0^2\right)}$$
$$z_N = \sqrt{\left(1 - x_N^2 - y_N^2\right)}.$$

(3.4)

The midpoint along the loop baseline connecting the two footpoints is,

$$\mathbf{r_m} = \left(\mathbf{r_I} + \mathbf{r_{II}}\right)/2\,.$$

(3.5)

A local coordinate system that has unit vectors $\mathbf{e_b}$, $\mathbf{e_n}$ and $\mathbf{e_t}$ with the origin at $\mathbf{r_m}$ is defined where,

$$\mathbf{e_b} = \left(\mathbf{r_{II}} - \mathbf{r_I}\right)/\left|\mathbf{r_{II}} - \mathbf{r_I}\right|$$
$$\mathbf{e_n} = \mathbf{r_m}/\left|\mathbf{r_m}\right|$$
$$\mathbf{e_t} = \mathbf{e_b} \times \mathbf{e_n}\,.$$

(3.6)

The loop plane is defined by the three points $\mathbf{r_I}, \mathbf{r_{II}}$ and $\mathbf{r_{III}}$ where,

$$\mathbf{r_{III}} = \mathbf{r_m} + \mathbf{e_n} + \mathbf{e_t}\tan\theta,$$

(3.7)

and θ is the inclination of the plane with respect to the photospheric normal.

In this chapter the loops are assumed to be planar so that the depth coordinate z_i of each loop point will lie within the plane if,

$$\begin{vmatrix} x_i & y_i & z_i & 1 \\ x_I & y_I & z_I & 1 \\ x_{II} & y_{II} & z_{II} & 1 \\ x_{III} & y_{III} & z_{III} & 1 \end{vmatrix} = 0\,.$$

(3.8)

z_i is then eliminated from equation 3.8 and a 3D loop shape with a user defined inclination angle is obtained.

By comparing the loop projections from two viewpoints (e.g. SDO and STEREO), θ can be constrained. To compare the events in the two different instruments, chosen loop image coordinates in EUVI are converted to heliographic Cartesian and then to heliocentric Aries ecliptic (HAE) coordinate systems. These coordinates are then converted back into the AIA coordinate system and displayed on an AIA image. The heliographic coordinate system co-rotates with the solar surface and describes a feature on the Sun in terms of its latitude and longitude. The latitude is measured from the solar equator and the longitude is defined westward from the solar prime meridian. This system can be extended to three dimensions by including the radial distance of the feature from the Sun's centre. The heliocentric Aries ecliptic

coordinate system is a right handed system that is fixed with respect to the distant stars. The Z axis is perpendicular to the plane of the Earths orbit around the Sun (positive North) and the X axis is towards the first point of Aries. The first point of Aries, or vernal equinox, is the intersection between Earth's equatorial plane and its plane of orbit around the Sun (the ecliptic plane) (Hapgood 1992; Fränz and Harper 2002; Thompson 2006).

The loop image coordinates x_i, y_i and z_i are renamed so that x is the direction pointing towards the observer and z points to North i.e. $(x_i, y_i, z_i) \rightarrow (y_i, z_i, x_i)$. Firstly the coordinates are converted to heliographic Cartesian coordinates by rotating x and z relative to the disk centre latitude B_0,

$$
\begin{pmatrix} y_i' \\ z_i' \\ x_i' \end{pmatrix} = \begin{pmatrix} 1 & 0 & 0 \\ 0 & \cos B_0 & \sin B_0 \\ 0 & -\sin B_0 & \cos B_0 \end{pmatrix} \begin{pmatrix} y_i \\ z_i \\ x_i \end{pmatrix}.
\tag{3.9}
$$

The first observers position (for this work it is STEREO) in HAE coordinates are found in the data header files (e.g. $x_{HAE} = $ -hdr.HAEX_OBS). The values of the heliocentric latitude (θ_{HAE}) and longitude (ϕ_{HAE}) are calculated by,

$$
\theta_{HAE} = \arctan \left(\frac{z_{HAE}}{\sqrt{x_{HAE}^2 + y_{HAE}^2}} \right)
\tag{3.10}
$$

$$
\phi_{HAE} = \arctan \left(y_{HAE}, x_{HAE} \right).
$$

The x, y and z loop coordinates are then rotated to the new heliocentric coordinate system via the rotation,

$$
\begin{pmatrix} y_i' \\ z_i' \\ x_i' \end{pmatrix} = \begin{pmatrix} \cos \phi_{HAE} & 0 & \sin \phi_{HAE} \\ 0 & 1 & 0 \\ -\sin \phi_{HAE} & 0 & \cos \phi_{HAE} \end{pmatrix} \begin{pmatrix} 1 & 0 & 0 \\ 0 & \cos \theta_{HAE} & -\sin \theta_{HAE} \\ 0 & \sin \theta_{HAE} & \cos \theta_{HAE} \end{pmatrix} \begin{pmatrix} y_i \\ z_i \\ x_i \end{pmatrix}.
\tag{3.11}
$$

Next θ_{HAE} and ϕ_{HAE} are calculated for the second viewpoint, in this case SDO, and the reverse rotation transform is applied,

$$
\begin{pmatrix} y_i' \\ z_i' \\ x_i' \end{pmatrix} = \begin{pmatrix} \cos \phi_{HAE} & 0 & -\sin \phi_{HAE} \\ 0 & 1 & 0 \\ \sin \phi_{HAE} & 0 & \cos \phi_{HAE} \end{pmatrix} \begin{pmatrix} 1 & 0 & 0 \\ 0 & \cos \theta_{HAE} & \sin \theta_{HAE} \\ 0 & -\sin \theta_{HAE} & \cos \theta_{HAE} \end{pmatrix} \begin{pmatrix} y_i \\ z_i \\ x_i \end{pmatrix}.
\tag{3.12}
$$
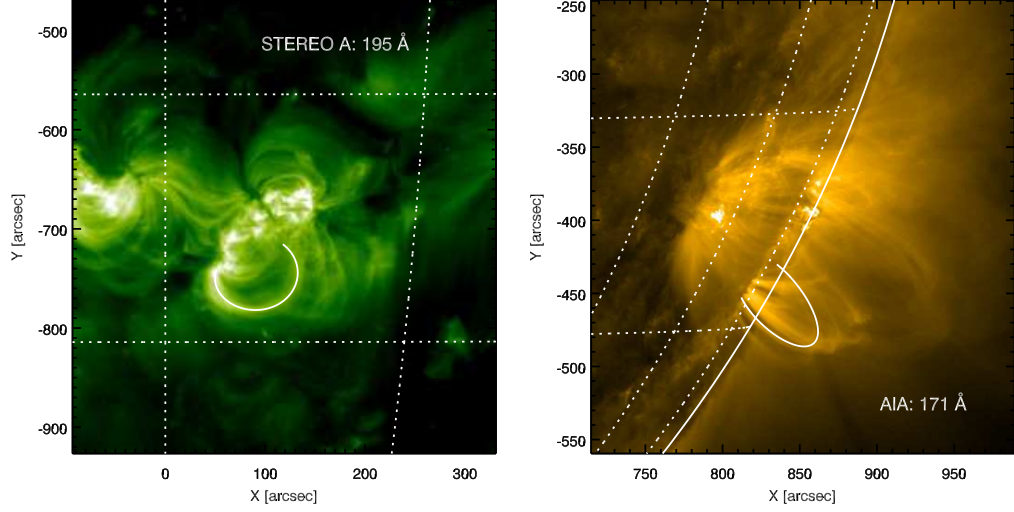
Figure 3.7: Left: EUVI 195 Å image from STEREO A showing loop points chosen on active region NOAA 11079, Event 1. Right: SDO/AIA 171 Å image showing the projected loop coordinates chosen on the EUVI image to compare the 3D loop geometry. The inclination and azimuthal angles are $\theta = 26°S$ and $\alpha = 69°$ anticlockwise from north respectively.

Before converting the coordinates back to the heliographic system the change in longitude due the difference in time between the SDO and STEREO images must be taken into account. The x and y coordinates are rotated through the change in longitude L_0,

$$\begin{pmatrix} y'_i \\ z'_i \\ x'_i \end{pmatrix} = \begin{pmatrix} \cos L_0 & 0 & \sin L_0 \\ 0 & 1 & 0 \\ -\sin L_0 & 0 & \cos L_0 \end{pmatrix} \begin{pmatrix} y_i \\ z_i \\ x_i \end{pmatrix}. \qquad (3.13)$$

The last step is for the new coordinates to be converted from the heliocentric system to the heliographic system using the disk centre latitude value from AIA,

$$\begin{pmatrix} y'_i \\ z'_i \\ x'_i \end{pmatrix} = \begin{pmatrix} 1 & 0 & 0 \\ 0 & \cos B_0 & -\sin B_0 \\ 0 & \sin B_0 & \cos B_0 \end{pmatrix} \begin{pmatrix} y_i \\ z_i \\ x_i \end{pmatrix}. \qquad (3.14)$$

The loop coordinates projected onto the new viewpoint image are inspected to see if it matches well with the observed loop and the inclination is varied to ensure that the best possible match is made.

Figure 3.7 shows an example of loop points chosen in an EUVI image converted and displayed on an AIA image for Event 1 for the optimal inclination angle, $\theta = 26°S$.
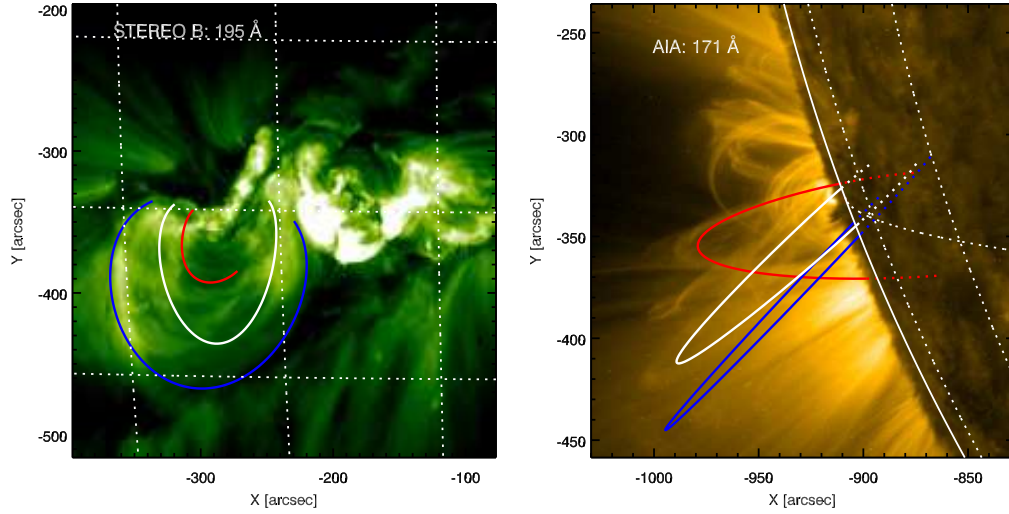
Figure 3.8: Left: EUVI 195 Å image from STEREO B showing loop points chosen on active region NOAA 11121, Event 3. Right: SDO/AIA 171 Å image showing the projected loop coordinates chosen on the EUVI image to compare the 3D loop geometry for loops 1 (blue), 2 (white), and 4 (red). The inclination and azimuthal angles for the loops 1,2, and 4 are $\theta = 27°$S, 26°S, and -17°S and $\alpha = 100°$, 90°, and 153° anticlockwise from north respectively.

The reverse process from AIA to EUVI can also be performed however this does not always work because of the uncertainty in the footpoint locations for the events on the limb. Figure 3.8 shows examples of the 3D geometry acquired for three loops (1,2, and 4) in Event 3. Loop coordinates are determined for a chosen inclination angle and then compared to the loops displayed in the images to see if there is a close match. Table 3.1 shows the estimated loop lengths, L, and inclination angles, θ, determined using this method. The errors on the loop lengths and inclination angles are given by the standard deviations of repeated measurements and are a measure of the precision of the method using the planar loop model. It is expected that there is an error on the loop length of at least 10%. Directly comparing the loops in the EUVI and AIA images is difficult because EUVI has a worse spatial resolution than AIA and there is an uncertainty in distinguishing the loops from one another. For Event 2 it is not possible to distinguish and identify the individual loops in the EUVI image because of poor contrast against the solar disk. Therefore, this method gives here an estimate of the general loop arcade geometry rather than a detailed fit to each loop separately.

Other methods that reconstruct a 3D loop shape have also been developed. Stereo-scopic methods which rely on an accurate co-alignment between two images have

been used in a number of studies. Dynamic stereoscopy (Aschwanden et al. 1999a) takes advantage of the solar rotation so that observations of a loop structure seen by the same instrument at two different times (typically separated by a day) can be compared to give a 3D structure. Stereoscopic methods have also been used to reconstruct a loop seen by both the STEREO-A and STEREO-B spacecraft (Aschwanden et al. 2008). Alissandrakis et al. (2008) used SUMER observations of a loop to estimate a 3D loop geometry. Here they combine the plane of sky projected loop points with the Doppler shift in velocity observed along the loop length. Assuming a planar loop and including the inclination as a free parameter they reconstructed the flow velocity for each inclination angle from the observed Doppler shift and chose an inclination angle using the condition of continuity of the flow velocity. A different approach using bézier curves was presented by Gary et al. (2013). This manual technique uses only four points per loop to obtain 2D projected loop coordinates from solar images. This method can then be generalised to 3D with two additional scalar height parameters. An advantage of this method is that the interactive computer process developed uses co-spatial magnetogram and EUV images allowing loop footpoints to be more accurately located. Lastly Nisticò et al. (2013b) use the principle component analysis to determine the 3D loop shape from stereoscopic measurements. This method has the advantage that a relatively small number of data points are needed (10-20) and interpolation of the data points is not required before further steps to determine the loop shape are carried out.

3.5 Intensity variations

Intensity variations are reliably observed in the time distance images for six of the loops, loops 2 and 3 in Event 1 and loops 1,2,3 and 5 in Event 3. Figure 3.9 shows intensity variations observed in three of the cuts for loop 2 in Event 1. The images have been saturated to clearly show the variations in intensity. The intensity at each time series point is recorded and the extracted relative intensity time series are analysed using the same procedure of subtracting a background and fitting a damped cosine function as discussed above for the displacement time series analysis. The extracted intensity time series does not always display clear oscillations that can be fitted with the damped cosine function. Figure 3.10 shows the intensity time series for loop 2 in Event 1 fitted with the damped cosine function. The intensity has been normalised by the subtracted background intensity. It shows that there are significant intensity variations of between approximately 10% and 30% of the background intensity, which are in anti-phase with the displacement oscillation. As
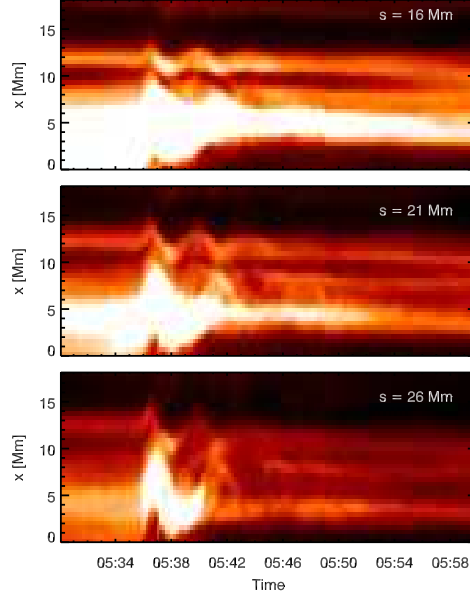
Figure 3.9: Time distance images taken from three cuts used to analyse loop 2 in Event 1. The images have been saturated to highlight the intensity variations along the loop. Loop 2 is the isolated loop above the bundle of loops.

the distance along the loop increases from the footpoint to the apex, the intensity amplitude increases. This suggests that the intensity amplitude scales with the displacement amplitude. Figure 3.11 shows the intensity time series for loops 2,3 and 5 in Event 3 which correspond to the displacement time series cuts shown in Figure 3.5. Transverse loop oscillations interpreted as kink MHD waves are quasi-incompressible and as a result are not expected to produce variations in the intensity. However there are mechanisms such as non linear and linear coupling to slow MHD modes and line of sight effects which may explain the intensity oscillations observed in some of the loops.

Table 3.2 shows the results for the intensity time series analysis of the three events. The results include the analysis of intensity variations that are less reliably observed due to the contrast with the background plasma but for which an extracted time series can be fitted with a damped cosine function. For all except loop 1 in Event 2 the intensity and displacement oscillations are observed to be in phase or in anti-phase. As the choice of direction of the cut across the loop is arbitrary, this means that the two types of oscillation are in phase. The phases have been corrected to the same reference times and the errors have been calculated in the same way as the time series analysis. The results show intensity periods that are similar to the displacement time periods except for loop 1 in Event 3. Figure 3.12 shows
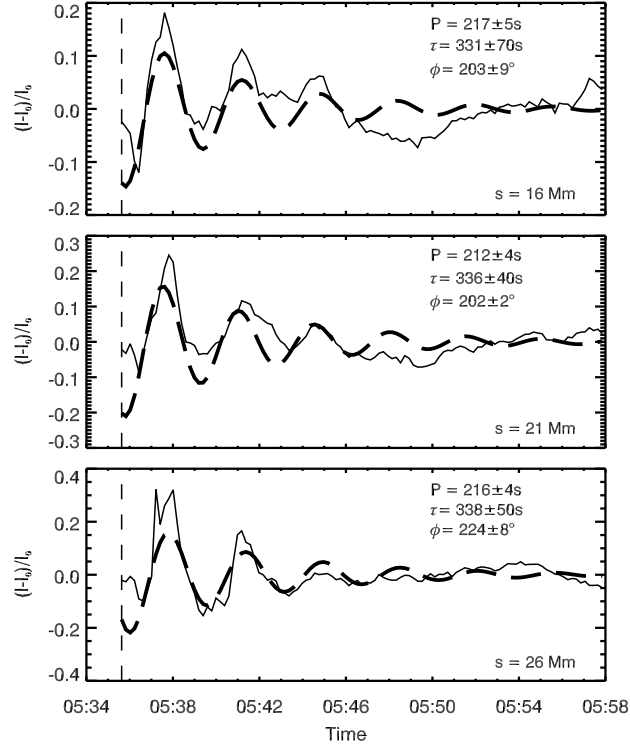
Figure 3.10: Intensity time series analysis for loop 2 in Event 1. The solid line shows the intensity time series which has been fitted with a damped cosine function (thick dashed line). The background subtracted intensity amplitude has been normalised by the background. Top: $s = 16$ Mm. Centre: $s = 21$ Mm. Bottom: $s = 26$ Mm. The errors on the fitting parameters are the errors given by the fitting technique. The vertical dashed line indicates the reference time of 05:35:59 UT.
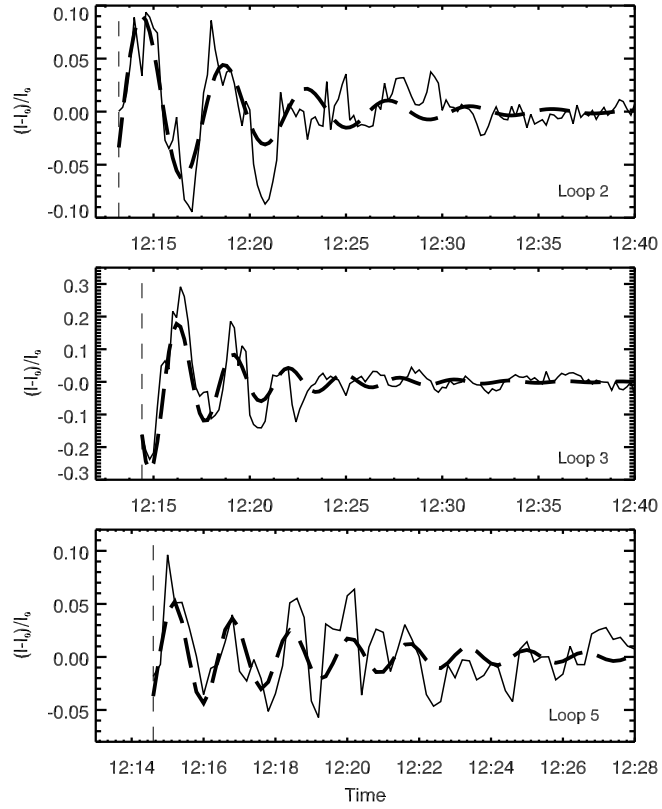
Figure 3.11: Intensity time series analysis for loops 2, 3 and 5 in Event 3. The solid line shows the intensity time series which has been fitted with a damped cosine function (thick dashed line). The background subtracted intensity amplitude has been normalised by the background. The vertical dashed line indicates the reference time for each cut.
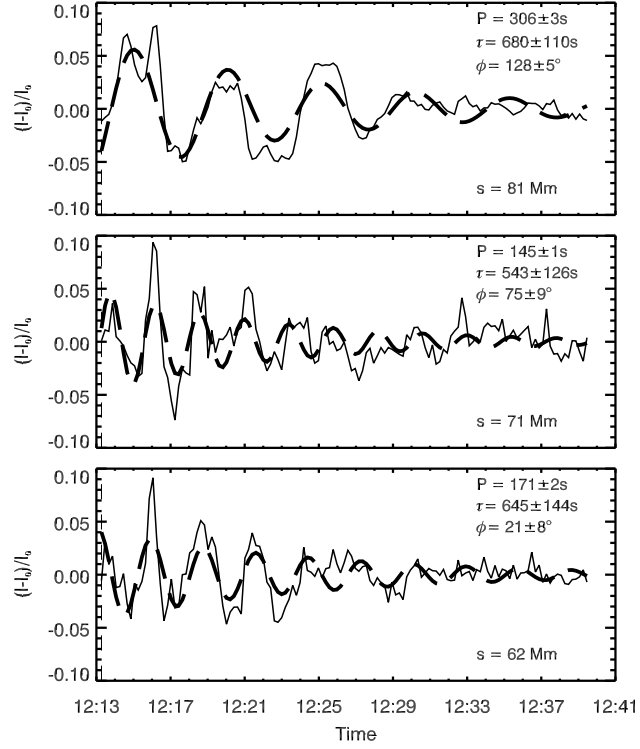
Figure 3.12: Intensity time series analysis for loop 1 in Event 3 showing the variation of the period with the loop distance coordinate s. Top: s = 81 Mm. Centre: $s = 71$ Mm. Bottom: $s = 62$ Mm. The errors on the fitting parameters are the errors given by the fitting technique. The solid line shows the intensity time series which has been fitted with a damped cosine function (thick dashed line). The background subtracted intensity amplitude has been normalised by the background. The vertical dashed line indicates the reference time of 12:13:36 UT.

65

Table 3.2: Intensity oscillation parameters determined for each event

Event	Loop	I_A [a]	P (s)	τ (s)	ϕ (°)
1	2	0.22 ± 0.02	215 ± 2	350 ± 30	213 ± 10
	3	0.22 ± 0.02	247 ± 40	313 ± 20	184 ± 70
2	1	(0.06)	(550)	(552)	(126)
	2	(0.05)	(612)	(422)	(300)
3	1	0.06 ± 0.01	306 ± 3	623 ± 70	75 ± 50
	2	0.16 ± 0.02	235 ± 20	407 ± 160	90 ± 40
	3	0.27 ± 0.02	148 ± 40	224 ± 60	114 ± 10
	4	(0.22)	(130)	(180)	(50)
	5	0.10 ± 0.02	99 ± 2	314 ± 140	94 ± 30

[a] The intensity amplitude I_A is the background subtracted intensity that has been normalised by the background. It is the maximum intensity given by the damped cosine fit. Intensity variations for the loops with parameters in brackets were not reliably observed in the time distance images. The period for loop 1, Event 3 is for the case s = 81 Mm.

the intensity time series plots for loop 1 which shows that the period significantly changes along the loop. This may indicate that the intensity variations are resulting from a line of sight effect caused by loop paths crossing. Except for loop 1 of Event 3, the periods of the displacement and the intensity variations match within 2σ.

3.5.1 Simulations of the intensity variations from the horizontally polarised mode

With an estimate of the 3D loop geometry from the AIA-EUVI comparison, the intensity variations observed in loop 2, Event 1 shown in Figure 3.10 are investigated further. The modelled loop is given a volume and a density contrast of 10 with the background and the loop radius is assumed to be 1 Mm. To simulate the motion the loop is perturbed as,

$$\vec{r}_{loop} = \vec{r}_{loop,0} + \xi_0 \cos\left(\phi\right) \sin\left(\frac{n\pi}{L}s\right) \vec{e}_\perp, \qquad (3.15)$$

where $\vec{r}_{loop,0}$ is the loop position at rest, ξ_0 is the amplitude (estimated to be 5.7 Mm), ϕ is the phase, n indicates the harmonic, s is the loop distance coordinate and L is the loop length. The unit vector $\vec{e}_\perp$ is defined as,

$$\vec{e}_\perp = -\vec{e}_n \sin(\theta) + (\vec{e}_b \times \vec{e}_n) \cos(\theta), \qquad (3.16)$$
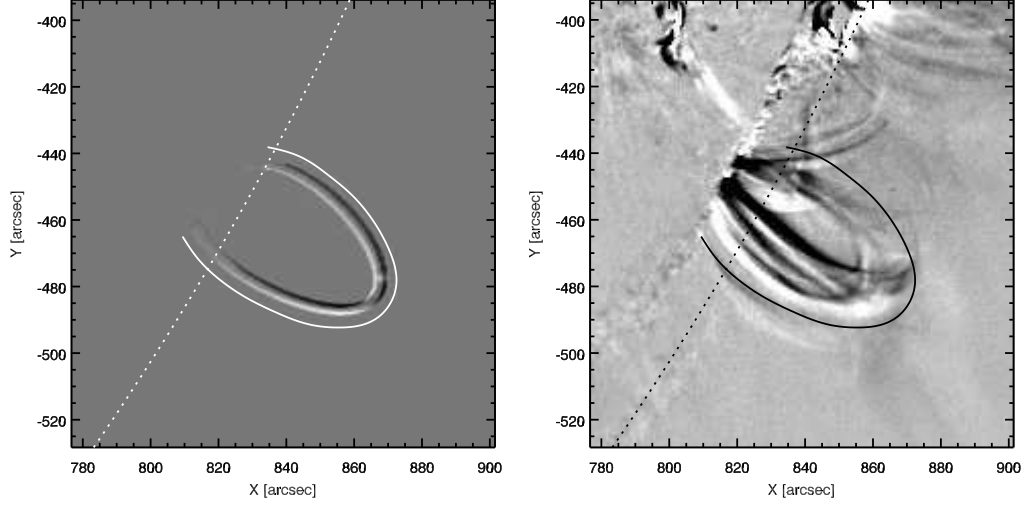
Figure 3.13: Left: Simulated difference image for the modelled horizontally polarised loop 2 from Event 1. Right: Difference image of Event 1 co-structured by subtracting the image taken at 5:40:23 UT from the one at 5:38:23 UT. The dotted line indicates the solar limb.

where $\vec{e}_n$ is the photospheric normal unit vector and $\vec{e}_b$ is the unit vector parallel to the loop footpoints. A movie of the loop motion can be constructed in 3D and projected onto the image plane where the loop is uniformly filled and then analysed in the same way as the observational data set.

Figure 3.13 shows a difference image for the modelled horizontally polarised loop and a difference image from two AIA images. This and visual inspection of the AIA movie shows that the oscillation is horizontally polarised. (Therefore, the simulations are focused on this mode rather than the vertically polarised mode). The pattern on the bottom leg of the simulated loop is matched by the difference image of the observed data set. Figure 3.14 shows the time distance images taken of the simulation data set. The three central figures correspond to the same position along the loop as for the cuts in Figure 3.2. Figure 3.15 shows the automatically determined displacement time series of the simulations. As expected they show that as the distance along the loop increases towards the apex the displacement amplitude also increases. Figure 3.16 shows the corresponding intensity time series. Here, clear intensity variations are observed, which can also be seen in the time distance images. In the simulations the intensity variations can only be due to variations in the line-of-sight column depth. The amplitude of the intensity variation at each location along the loop depends on the amount of displacement but also on the angle of the local loop axis unit vector and the line-of-sight. This explains what

we observe. First, comparing Figures 3.15 and 3.16 shows that towards the loop apex ($s \geq 21$ Mm) the intensity amplitude indeed increases with the displacement. The exact match of the ratio of intensity and displacement amplitudes between observation and simulation depends on the size and structure of the loop cross-section (Verwichte et al. 2009). Towards the nearest footpoint ($s < 21$ Mm), the simulation shows an increase in intensity variations. There, the loop axes is oriented near the line-of-sight so that we look almost down onto the footpoint. Therefore, the integrated intensity there has an increased sensitivity to displacements that changes the orientation of the loop axis.

3.5.2 Discussion of the intensity variations

From the comparison between EUVI and AIA data including the simulations of loop 2 in Event 1, and the fact that the displacement and intensity amplitudes are observed to increase with distance along the loop towards the loop apex (see Figure 3.3, 3.10), it is expected that the intensity oscillations are due to line of sight effects of the horizontally polarised kink mode (Cooper et al. 2003; Verwichte et al. 2009, 2010).

The intensity variations due to line of sight effects arise because as the loop oscillates, the column depth of a given loop segment in the line of sight changes. The intensity of the emission is proportional to the column depth l and the square of the loop density ρ_0,

$$I \propto \rho_0^2 l, \tag{3.17}$$

so that an oscillating loop that has a varying column depth in the LOS will produce an oscillation in the intensity emission.

Other mechanisms such as non linear (Terradas and Ofman 2004) and linear coupling effects (Terradas et al. 2011) which can cause intensity variations would not be expected to cause the variations here.

For the case of non linear coupling, ponderomotive forces generated by large amplitude kink oscillations cause a longitudinal flow along the loop leading to the generation of density perturbations at the loop top. The period of the kink mode P_k would approximately relate to the period of the slow mode P_s as $P_k / P_s \cong 2 C_s / C_k$ which under coronal conditions is expected to be much less than one. Observed intensity variations have periods that are similar to the displacement periods which would rule out non linear coupling for these cases.

In the linear coupling case, assuming line tied boundary conditions and a small plasma-β, an MHD standing kink mode will have a large v_x velocity component and
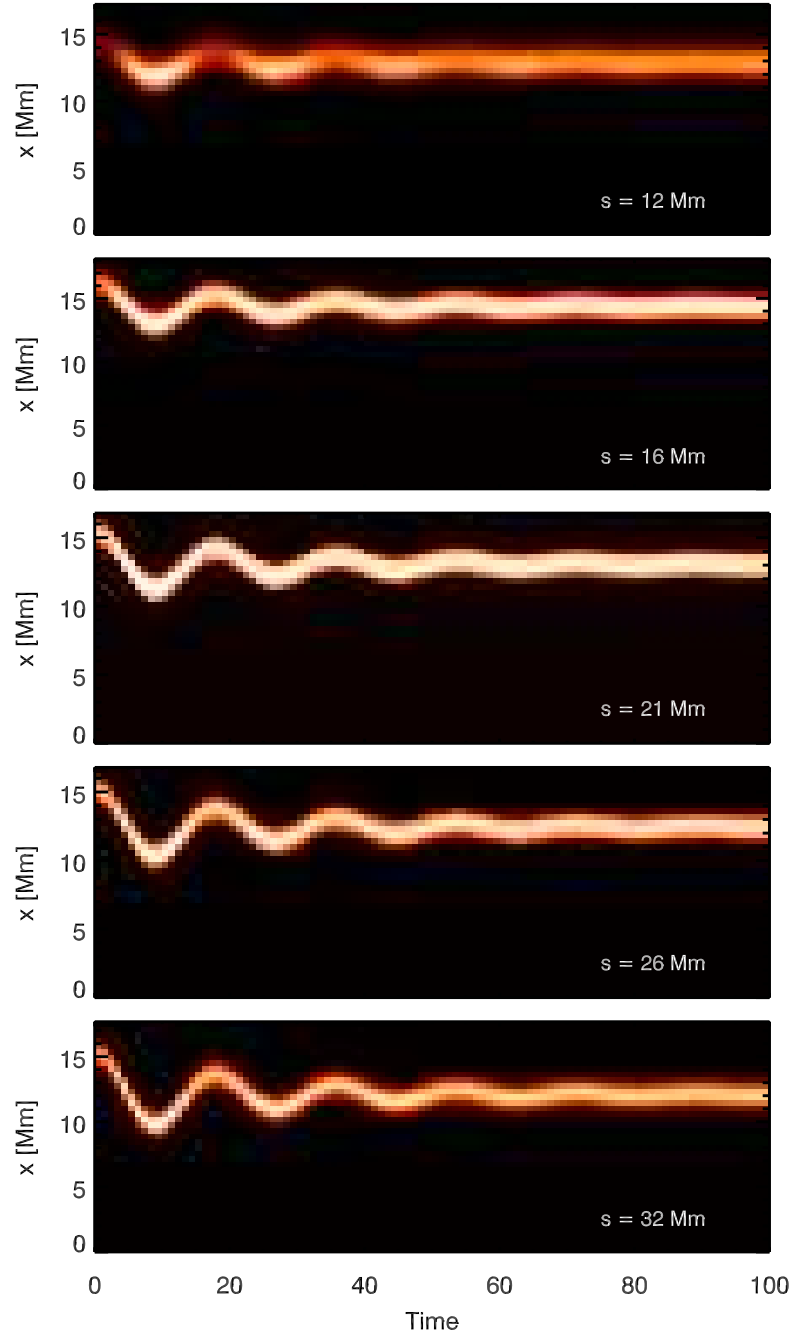
Figure 3.14: Time distance images obtained from five cuts used to analyse the horizontally polarised simulations of loop 2 from Event 1. The s distance along the loop corresponds to the position of the cuts relative to the observed loop in the AIA image.
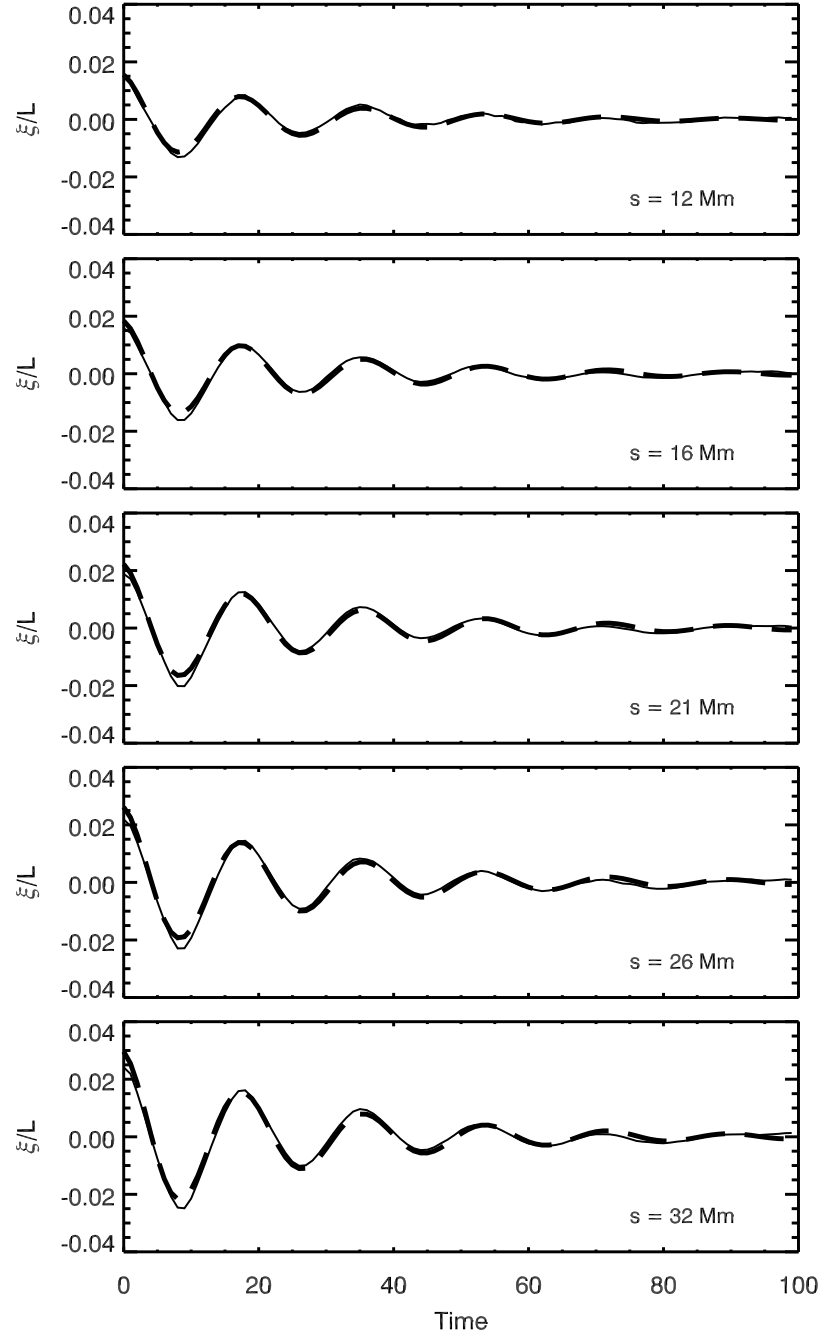
Figure 3.15: Automatically determined time series (solid line) for the cuts displayed in Fig. 3.14 fitted with a damped cosine function (thick dashed line). The displacement amplitude has been normalised by the loop length. The s distance along the loop corresponds to the position of the cuts relative to the observed loop in the AIA image.
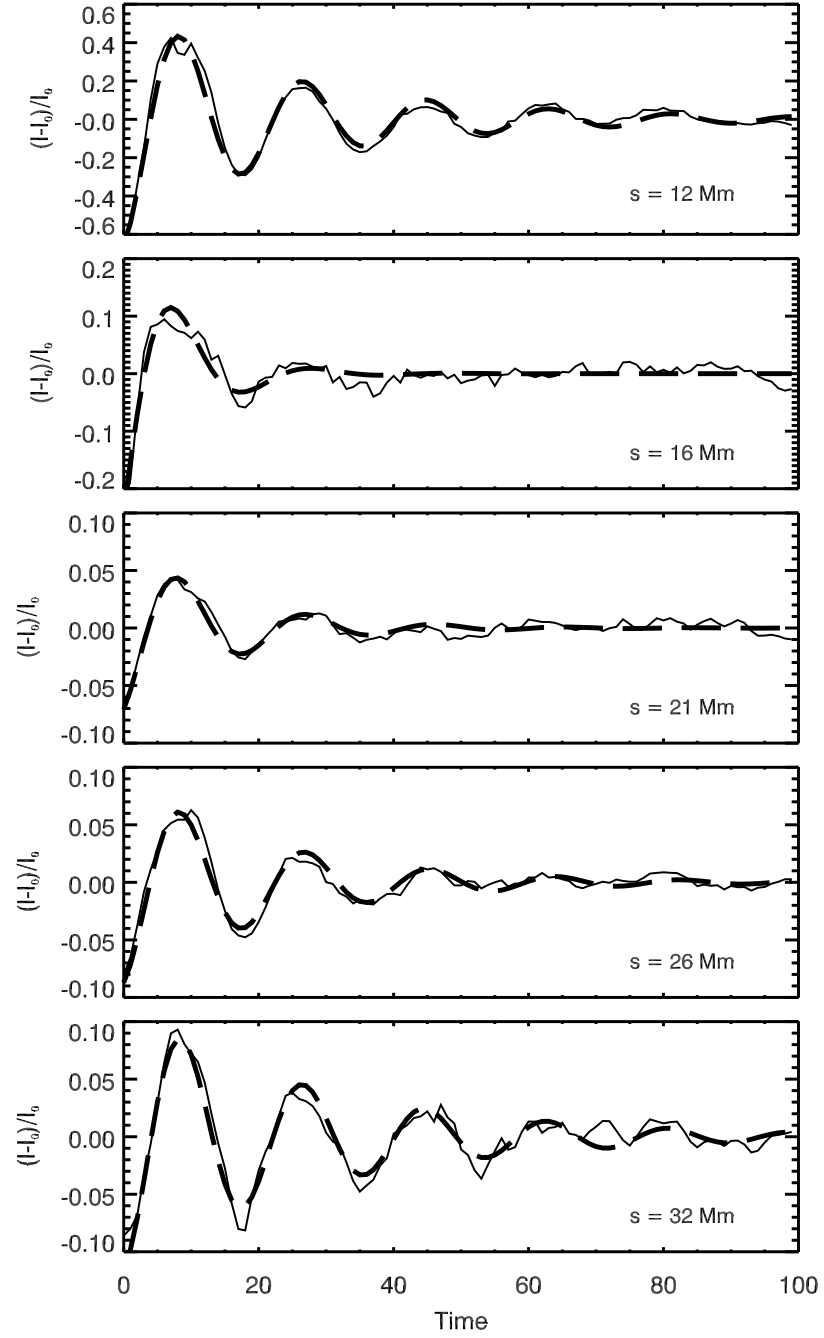
Figure 3.16: Intensity time series analysis of the simulations of loop 2 from Event 1 assuming a horizontally polarised mode. The intensity time series (solid line) has been fitted with a damped cosine function (thick dashed line). The background subtracted intensity amplitude has been normalised by the background. The s distance along the loop corresponds to the position of the cuts relative to the observed loop in the AIA image.

a small v_z velocity component. To satisfy the boundary conditions a slow magnetoacoustic mode with a dominant v_z component is added. This slow mode leads to propagating density fluctuations which have the same frequency as the standing kink mode and are strongest at the loop footpoints. Intensity perturbations observed at loop footpoints by Verwichte et al. (2010) may be an example of linear coupling between fast and slow MHD modes although the authors suggest the intensity variations are due to line of sight effects. The strength of the linear coupling depends on the plasma-β and in active region loops with lengths of 100-200 Mm the plasma-β is expected to be small. For linear coupling the wavelength of the slow magnetoacoustic mode λ_s would approximately relate to the wavelength of the kink mode λ_k under coronal conditions as $\lambda_s \cong (C_s/C_k)\lambda_k \cong 0.15\lambda_k = 0.3L$. We have not observed variations in the intensity over such short distances along the loops.

The variations in intensity of loop 1 in Event 3 is an intriguing case as these are not easily explained by wave coupling or line of sight variations of the oscillating loop. Another potential explanation could be in terms of independently running slow waves. However, these would have short wavelengths and we would have observed phase shifts between different cuts, which we do not. It is possible that we see periods in intensity variations of approximately half the displacement periods if the variations were due to the loop periodically overlapping another structure. During each oscillation cycle we would then see two intensity enhancements. However, for this observed loop the poor intensity contrast does not allow us to make a definite conclusion.

3.6   Application of coronal seismology

For the MHD kink mode in the long wavelength and zero plasma-β limit, the phase speed is equal to the kink speed, C_k, which can be written as $C_k = (2/(1 + \rho_e/\rho_0))^{1/2}V_{A0}$ (Edwin and Roberts 1983) where ρ_e and ρ_0 are the external and internal densities and V_{A0} is the internal Alfvén speed. Assuming that the density contrast ρ_e/ρ_0 has extremes of 0 and 1 then the range of the internal Alfvén speed is given by the inequality $V_{A0} \leq V_{ph} \leq \sqrt{2}V_{A0}$ (Nakariakov and Ofman 2001). Following this, the range of the magnetic field can be written as,

$$\frac{V_{ph}}{\sqrt{2}}\sqrt{\mu_0\tilde{\mu}m_pn_e} \leq B \leq V_{ph}\sqrt{\mu_0\tilde{\mu}m_pn_e}, \tag{3.18}$$

where μ_0 is the permeability, $\tilde{\mu}$ is the effective particle mass with respect to the proton mass (m_p) and has a value of 1.27 in the solar corona. The electron number density, n_e of the loops has an assumed value of 10^{15} m^{-3}. If we assume the os-

Table 3.3: Seismology parameters

Event	Loop	Minimum V_{A0} (kms^{-1})	B (G)
1	1	761 ± 155	3.9 - 5.6
	2	730 ± 75	3.8 - 5.3
	3	876 ± 95	4.5 - 6.4
	4	740 ± 118	3.8 - 5.4
2	1	1077 ± 108	5.6 - 7.9
	2	887 ± 116	4.6 - 6.5
3	1	1861 ± 256	9.6 - 13.6
	2	1326 ± 175	6.8 - 9.7
	3	2524 ± 303	13.0 - 18.4
	4	2100 ± 318	10.9 - 15.4
	5	1812 ± 230	9.4 - 13.2

cillation is damped by resonant mode conversion then the lower limit of the phase speed can be higher (Goossens et al. 2008). Table 3.3 shows the minimum internal Alfvén speed and the range of the magnetic field calculated from the analysis of the kink oscillations of the eleven coronal loops studied. The magnetic field estimates display a narrow range that are consistent with the range of 4 to 30 G predicted by Nakariakov and Ofman (2001). The uncertainty in the magnetic field values is calculated by $\delta B = B \left(\delta V_{ph} / V_{ph} \right)$. This gives an uncertainty of less than 21% for all values of the magnetic field. One of the main challenges for determining the magnetic field is estimating the density contrast between the loops and the background corona. This is especially challenging for on limb events where the column depth is larger than for on disk events. The largest magnetic field strengths are observed for loop 3 in Event 3. This could be a result of this loop being less dense.

3.7 Coronal seismology using the analytic inversion technique

The analytic seismology inversion scheme introduced by Goossens et al. (2008) is applied to the three events. Values of the damping time τ_d and the period P are known from the observations and z must take a value between $1/C$ and 1. Figures 3.17, 3.18 and 3.19 show the analytical curves produced relating ζ, the inhomogeneity length scale (l/R) and τ_{Ai} for each of the three events. They show a clear need to be able to obtain reliable, accurate estimates of at least one of the parameters
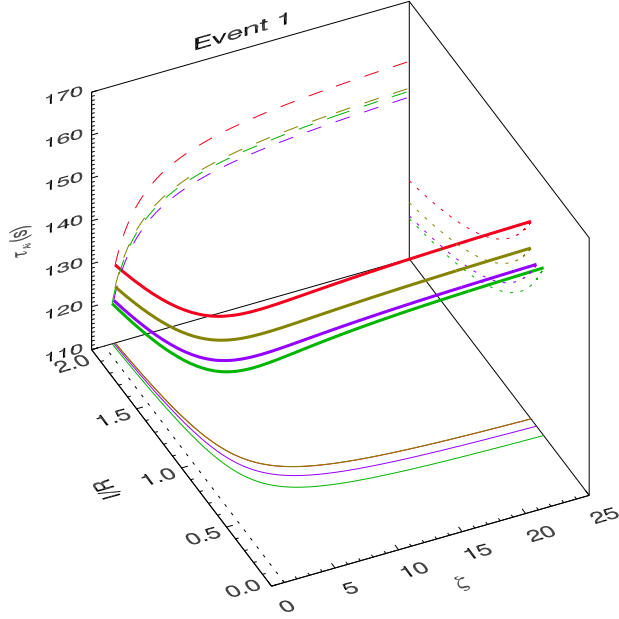
Figure 3.17: Analytic approximate seismology of Event 1. Loop 1 (red), loop 2 (green), loop 3 (purple), loop 4 (gold). Loop 1 overlaps with loop 4 on the l/R - ζ plane.

in order to narrow down parameter ranges. We also note that, as seen before, τ_{Ai} is relatively confined however the other two parameters, l/R and ζ can take a wide range of values.

The analytical curves for Event 1 (Figure 3.17) have comparable values for τ_{Ai}, however on the l/R - ζ plane only three curves are observed. Here the curves for loops 1 and 4 are plotted on top of one another, indicating that they have close to or the same damping ratios (P/τ_d). From the observational results given in Table 3.1, the damping ratio for loops 1 and 4 are 0.938 and 0.939 respectively. These are indeed similar, leading to similar analytical curves. The analytical curves demonstrate that for the loops in this active region their observational and seismological values are comparable to one another. This suggests the similarity of the loops and the surrounding loop environments.

Figure 3.18 shows the analytical curves for Event 2. The damping ratios are 0.707 and 0.773 for loops 1 and 2 respectively and the $\tau_{A,i}$ values are larger than those found in Events 1 and 3. This suggests that these two loops are similar to one another but that they may be entirely different to the loops and/or loop environments from events 1 and 3. This should come as no surprise since in comparison to the other

74
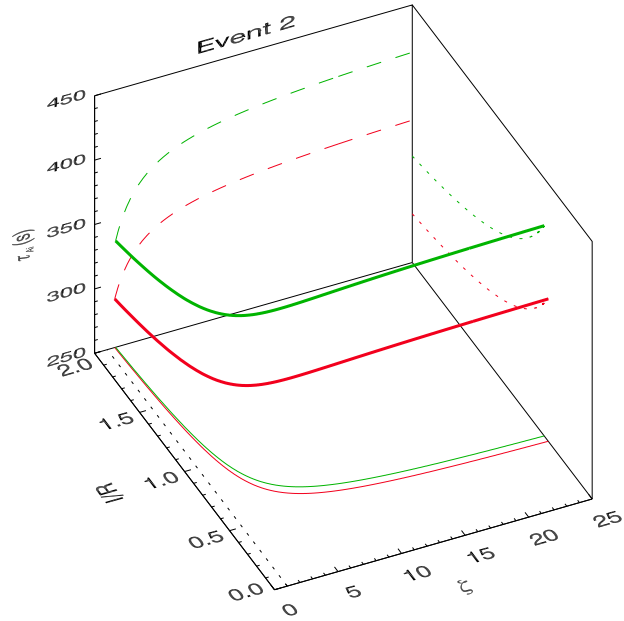
Figure 3.18: Analytic approximate seismology of Event 2. Loop 1 (red), loop 2 (green).
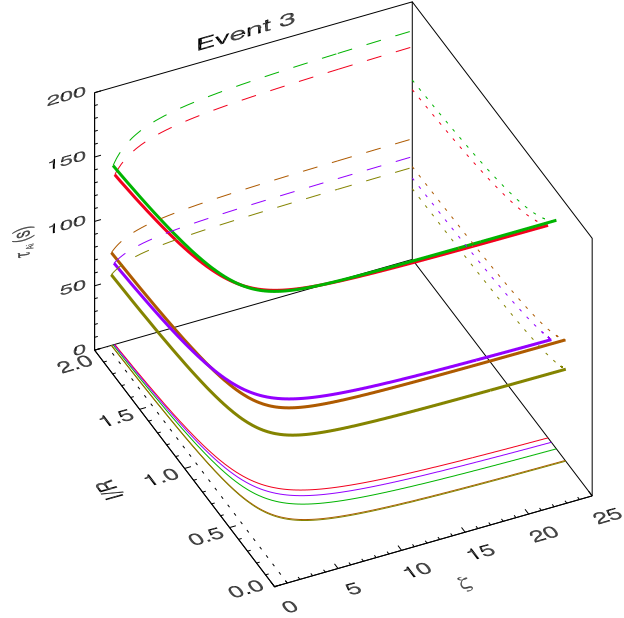
Figure 3.19: Analytic approximate seismology of Event 3. Loop 1 (red), loop 2 (green), loop 3 (orange), loop 4 (purple), loop 5 (gold). Loop 5 overlaps with loop 3 on the l/R - ζ plane.

events, Event 2 consisted of a smaller flare event and more gentle loop oscillations with a lower contrast to the background plasma.

Figure 3.19 shows the analytical curves for Event 3 which shows two distinct groups of loops in terms of τ_{Ai}. Loops 1 and 2 display values of τ_{Ai} around 170 s while loops 3, 4 and 5 display values of τ_{Ai} below 100 s. These values are comparable with those from Event 1. Loops 1 and 2 have longer periods compared to the other loops and from the observations appear to be in a similar loop plane that is different from the other loops. As in Event 1, two of the curves (loops 3 and 5) overlap each other on the l/R - ζ plane. Again this suggests that these two loops have comparable damping ratios and are in a similar environment.

Analytical inversion curves allow comparisons of loops in a single active region and between different active regions to be made. This technique can be used to highlight similarities and differences within active regions and help to distinguish the environments of the loops from one another. A limitation of this technique is that the errors on the observational quantities are not taken into account.

3.7.1 Bayesian inversion

Although the analytical technique provides a relatively confined value for the Alfvén travel time, in general neither the inhomogeneity length scale or the density contrast can be constrained without some estimate of one of the three parameters. Other limitations of this technique such as not taking into account the errors on the observational results can be overcome by applying a Bayesian inversion scheme (Arregui and Asensio Ramos 2011). In Arregui and Asensio Ramos (2011) a Markov Chain Monte Carlo method was used to sample the posterior distribution when a prior probability distribution for each of the three parameters had been provided. If an estimated value and the uncertainties of, e.g., the density contrast are known then a Gaussian prior probability distribution could be used which would allow all parameters to be constrained. Unfortunately estimating a precise value of the density contrast in coronal structures is challenging. Aschwanden et al. (2003) attempted to determine values of the density contrast and the inhomogeneity length scale of the eleven loop oscillations selected by Ofman and Aschwanden (2002). The method they use is to forward fit cross sectional flux profiles to the observed loop flux. Their values for the density contrast were then input back into the Bayesian technique with a Gaussian prior probability distribution by Arregui and Asensio Ramos (2011) to more accurately determine the remaining two parameters.
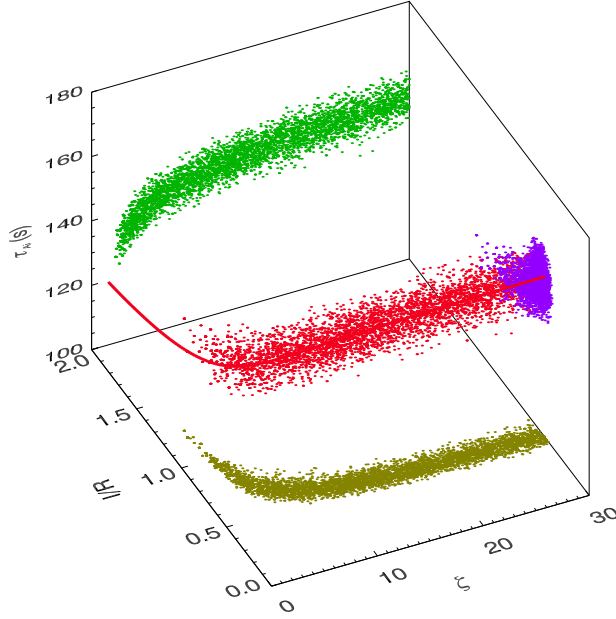
Figure 3.20: Bayesian seismology applied to loop 2, Event 1. A uniform prior probability distribution is used for the density contrast.

3.7.2 Bayesian inversion applied to the observational results

The observations presented in this chapter also include error estimates on the parameter values which should be taken into account when performing seismological inversion. Therefore we apply a Bayesian seismology technique (Arregui and Asensio Ramos 2011) to these results. The Bayesian scheme enables us to propagate the errors of the observed quantities to the seismologically determined quantities. This takes into account the errors on the period and damping times and a Markov Chain Monte Carlo method (code by Asensio Ramos et al. (2007)) is used to perform the inversion. In our analysis we use both a uniform and a Jeffreys prior probability distribution profile for ζ. The Jeffreys prior probability distribution is (Arregui and Asensio Ramos 2011),

$$p(\zeta) = \left[\zeta \log\left(\frac{\zeta_{max}}{\zeta_{min}}\right)\right]^{-1}, \tag{3.19}$$

where ζ_{max} and ζ_{min} are the maximum and minimum values of ζ respectively.
The other two parameters, l/R and τ_{Ai}, are given a uniform prior probability distribution. Arregui and Asensio Ramos (2011) comment that ζ of the loops is more likely to take lower values than the higher values more typically associated with, for
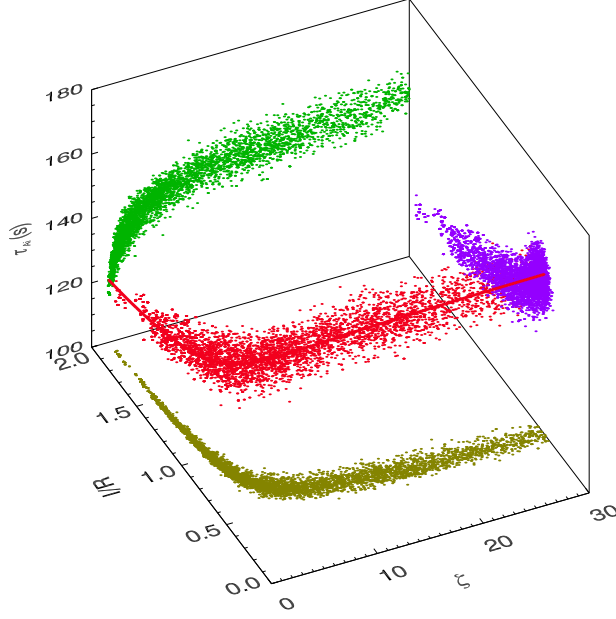
Figure 3.21: Bayesian seismology applied to loop 2, Event 1. A Jeffreys prior probability distribution is used for the density contrast.
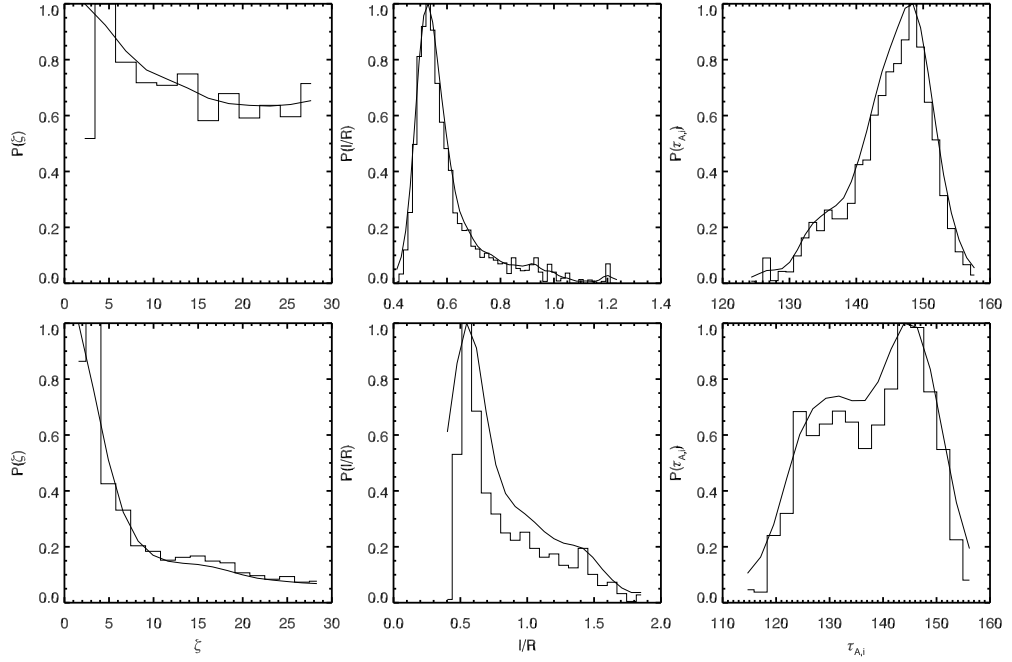
Figure 3.22: Marginalised posterior distributions for loop 2, Event 1. Top: A uniform prior probability distribution for the density contrast is used. Bottom: A Jeffreys prior probability distribution for the density contrast is used.

Table 3.4: Results of Bayesian inversion applied to the observed loops

	Uniform Profile		Jeffreys Profile	
Loop	l/R	$\tau_{A,i}$	l/R	$\tau_{A,i}$
1	$0.82\ ^{+0.38}_{-0.23}$	$155.3\ ^{+28.3}_{-27.7}$	$1.00\ ^{+0.53}_{-0.35}$	$148.8\ ^{+28.4}_{-30.4}$
2	$0.56\ ^{+0.14}_{-0.06}$	$145.9\ ^{+4.8}_{-7.4}$	$0.71\ ^{+0.51}_{-0.20}$	$138.5\ ^{+9.6}_{-12.3}$
3	$0.70\ ^{+0.25}_{-0.14}$	$144.2\ ^{+7.5}_{-9.1}$	$0.91\ ^{+0.54}_{-0.29}$	$137.1\ ^{+10.7}_{-12.6}$
4	$0.74\ ^{+0.20}_{-0.14}$	$146.9\ ^{+21.5}_{-20.5}$	$0.96\ ^{+0.58}_{-0.30}$	$138.7\ ^{+21.4}_{-22.7}$
5	$0.54\ ^{+0.12}_{-0.06}$	$354.4\ ^{+6.9}_{-15.2}$	$0.74\ ^{+0.68}_{-0.22}$	$327.8\ ^{+24.4}_{-32.3}$
6	$0.91\ ^{+0.57}_{-0.39}$	$404.8\ ^{+36.3}_{-37.7}$	$1.03\ ^{+0.52}_{-0.45}$	$389.1\ ^{+41.3}_{-42.1}$
7	$0.56\ ^{+0.20}_{-0.09}$	$143.1\ ^{+15.2}_{-15.8}$	$0.78\ ^{+0.63}_{-0.28}$	$134.4\ ^{+17.9}_{-17.2}$
8	$0.55\ ^{+0.34}_{-0.17}$	$173.3\ ^{+15.8}_{-15.8}$	$0.72\ ^{+0.56}_{-0.30}$	$163.6\ ^{+18.3}_{-17.9}$
9	$0.45\ ^{+0.42}_{-0.17}$	$90.9\ ^{+7.4}_{-8.2}$	$0.62\ ^{+0.58}_{-0.29}$	$85.9\ ^{+8.9}_{-9.8}$
10	$0.54\ ^{+0.19}_{-0.11}$	$78.3\ ^{+2.1}_{-3.5}$	$0.69\ ^{+0.60}_{-0.23}$	$74.5\ ^{+4.6}_{-7.8}$
11	$0.71\ ^{+0.70}_{-0.39}$	$69.6\ ^{+6.1}_{-6.4}$	$0.79\ ^{+0.65}_{-0.42}$	$66.5\ ^{+7.2}_{-7.6}$

example, thin threads of solar prominences. Here a Jeffreys profile may be more appropriate as the distribution is skewed towards loops with a lower contrast. We were unable to use a Gaussian prior probability distribution as this requires precise information on one of the three parameters which we do not have. For example obtaining an accurate estimate of the density contrast in the solar corona is challenging.

Figures 3.20 and 3.21 show the results of applying the Bayesian seismology technique to loop 2 from Event 1. Over plotted on the figures are the analytically determined curves. They show that changing the prior probability distribution on the density contrast from a uniform (Figure 3.20) to a Jeffreys distribution (Figure 3.21) changes the distribution of elements in the chain from a roughly uniform distribution along the inversion curve to a slightly more localised distribution around lower ζ values. The Bayesian results closely follow the analytical results. Figure 3.22 shows the posterior distributions for this loop showing that in general ζ cannot be constrained but that both l/R and τ_{Ai} can be constrained.

Table 3.4 shows the results for all eleven loops given either a uniform or Jeffreys prior probability distribution. The values in table 3.4 are given by the mean of the posterior distributions and the error bars are given at the 68% confidence level.
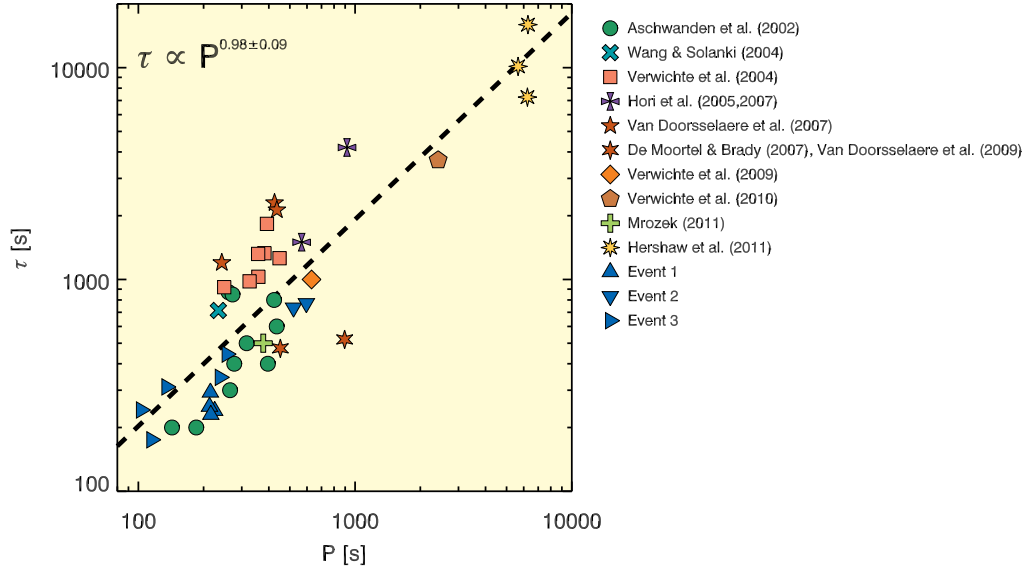
Figure 3.23: A comparison of the periods and damping times of Events 1, 2 and 3 with previous studies of transverse coronal loop oscillations and one prominence oscillation.

3.8   Summary

In this study the detailed analysis of eleven coronal loops observed in three events has been performed. The displacement time series analysis revealed periods between 1.7 and 10 minutes which are consistent with previous studies. Spatial observations of periods below 2 minutes have not been reported before as their detection requires instruments with short cadence times such as SDO/AIA. This study helps to build up a statistical picture of the behaviour of transverse loop oscillations which, along with coronal seismology provide a vital tool for coronal plasma diagnostics. The application of coronal seismology techniques of the MHD kink mode reveals magnetic field strengths in the range of 3 to 19 G which are consistent with expectations. Narrowing down the range of the density contrast would provide a more accurate value for the magnetic field however the main contribution to the uncertainty in most cases is the large error on the loop length. Scaling relationships between the damping time and the period have been derived for the damping mechanisms of resonant absorption and phase mixing. Figure 3.23 shows a comparison between the results from the three events studied in this paper with previous studies of coronal loop oscillations and one prominence oscillation. Not only do the results from this study increase the number of reported events by about a third but they also extend the range to shorter periods and damping times than have previously

been observed. Figure 3.23 gives a relationship between the damping time and period of $\tau = P^{0.98 \pm 0.09}$. Such a scaling can be reproduced by a resonant absorption damping mechanism, however this scaling should not be directly compared to the theoretical scaling because detailed information on loop properties is unavailable (Arregui et al. 2008). Directly comparing the damping time and periods of several events has been discussed by Hershaw et al. (2011). It was noted that the loops are not necessarily directly comparable because of the dependence on the damping time of the loop width and the thickness of the inhomogeneous layer which varies between loops. Nevertheless it shows that there is a relationship between the period and damping time of the loops. It is also noted that the damping times for Verwichte et al. (2004) may be biased towards longer damping times due to being semi driven by a prominence eruption close by. There have been recent reports of intensity variations in transverse loop oscillations which are also observed in this study. The intensity oscillations are found to have similar periods to the displacement time oscillations except for loop 1 in Event 3. In this case the period was observed to vary along the loop with intensity periods differing from the time series periods. We conclude that the intensity variations are due to variations in the line of sight column depth of a horizontally polarised transverse loop oscillation.

Chapter 4

First observation of a transverse vertical oscillation during the formation of a hot post-flare loop

4.1 Chapter overview

In this chapter, we present the first analysis of a higher-harmonic transverse oscillation in a hot loop observed with SDO/AIA. This observation is particularly interesting as the loop oscillates with a dominant higher-harmonic vertical mode and shows little evidence of a fundamental mode. Furthermore, it is only observed in the 131 Å (∼10 MK) and 94 Å (∼6.3 MK) bandpasses. This is an important observation as there are few spatially observed TLOs displaying higher order harmonics and this is the first example of a TLO to be observed in such hot bandpasses.

4.2 Introduction

4.2.1 Oscillations in hot flare lines

Coronal oscillations in hot flare lines such as Fe XIX (6.3 MK) and Fe XX (8 MK) have been observed with the Solar Ultraviolet Measurements of Emitted Radiation (SUMER) spectrometer on SOHO (Kliem et al. 2002; Wang et al. 2002, 2003a,b). The SUMER line-of-sight Doppler-shift observations of 27 events originating from limb active regions performed by Wang et al. (2003b) revealed oscillations with

periods between 7 min and 31 min and in a few cases intensity variations that lagged behind the Doppler shift velocities by a quarter period. Other observations utilising crystal spectrometers have also detected oscillations in flare regions. During the decay of a limb flare, Seely and Feldman (1984) detected a damped oscillation with a period of about 10 min with the solar flare X-rays (SOLFLEX) crystal spectrometer (Ca XIX line) on the P78-1 satellite. Heavily damped oscillations with periods of 3.9 min and 3.6 min and damping times of 3.5 min and 4.3 min observed with the Bragg Crystal Spectrometer (BCS) on Yohkoh were also reported (Mariska 2005). Both the SUMER and BCS oscillations were interpreted as standing slow magneto-acoustic modes because (i) the estimate of the phase speed was close to the value of the sound speed, (ii) in a few cases associated intensity variations were found to lag the Doppler shift velocities by roughly a quarter period and (iii) average oscillation periods were found to be significantly longer than transverse oscillations observed by the Transition Region and Coronal Explorer (TRACE), suggesting that they constitute a different type of oscillation. We refer to Wang (2011) for a detailed review of standing slow modes in hot coronal loops.

The SUMER observations share some features with transverse oscillations, such as their impulsive excitation, short damping times, and associated intensity variations. The BCS oscillations have periods and damping times consistent with those for transverse loop oscillations (TLOs). Transverse oscillation periods longer than 10 min have been observed (Hori et al. 2005; De Moortel and Brady 2007; Van Doorsselaere et al. 2009; Verwichte et al. 2009, 2010), which puts them in the range of those periods observed with SUMER. Tothova et al. (2011) detected in combined TRACE and SUMER observations the co-presence of slow and transverse standing modes, which manifested themselves as oscillations in Doppler velocity in an emission line sensitive to hot plasma of 6 MK. Although the evidence presented suggests that the coronal oscillations observed in hot flare lines are slow magneto-acoustic modes, instruments with high spatial resolution e.g. AIA that are able to make observations in hot coronal lines, may be able to confirm this or to provide a new interpretation for such hot oscillations.

4.2.2   Higher order harmonics of transverse loop oscillations

To date, there have been few observations of TLOs displaying higher harmonics. The first observation of higher harmonics in a coronal loop arcade was made by Verwichte et al. (2004). Here both the fundamental mode and the second harmonic were observed in a wavelet spectrum and the amplitude signatures were found to be consistent with two different periodicities. This first observation was followed by

analytic and numerical studies of the density stratification in coronal loops (Andries et al. 2005a,b; McEwan et al. 2006; Dymova and Ruderman 2006). In particular, the density stratification inside coronal loops is related to the ratio of the fundamental period (P_1) to the period of the second harmonic (P_2). For a uniform loop, P_1/P_2 is exactly 2, however this ratio can deviate from this value if there are longitudinal density variations along the loop. Another observation of higher order harmonics in TLOs was made by De Moortel and Brady (2007) for which a repeat analysis was conducted by Van Doorsselaere et al. (2009). This spatially resolved TRACE observation allowed three periodicities to be detected (which were identified as the fundamental mode and both the first and second harmonics). A third example of a higher harmonic TLO (Van Doorsselaere et al. 2007) identified both the fundamental mode and the first harmonic, which were detected in the signal residues.

Questions arising from the study of higher order harmonics include (1) why are the majority of observed TLOs excited as the fundamental mode and (2) what is the excitation method responsible for higher order harmonics? SDO/AIA provides new insights into coronal phenomena by increasing both the time and spatial resolutions. As coronal features such as TLOs are studied in ever greater detail (White and Verwichte 2012), signatures of higher harmonics may become easier to observe. The SDO may also provide further opportunities to study the exact nature of oscillations in hot coronal loops.

4.3   Event overview

The event occurred between 12:10:09 UT and 13:09:57 UT on the 3 November 2010 and has previously been studied in the context of the coronal mass ejection (CME) (Reeves and Golub 2011; Cheng et al. 2011; Bain et al. 2012), Kelvin-Helmholtz instability on the flank of the CME (Foullon et al. 2011), and transverse coronal loop oscillations (White and Verwichte 2012, Chapter 3). Further studies conducted after the observation presented in this chapter include studies of the reconnection inflow and outflow (Savage et al. 2012), investigation into the multi-thermal characteristics of the event (Hannah and Kontar 2013) and further work on the Kelvin-Helmholtz instability on the CME flank including numerical simulations (Foullon et al. 2013; Nykyri and Foullon 2013). During this event, a CME associated with a C4.9 class flare observed by the Geostationary Operational Environmental Satellite (GOES), peaking at 12:21 UT, was observed. A large loop oscillating exclusively in the 131 Å (Fe VIII/XXI) and 94 Å (Fe XVIII) bandpasses, appears near the south-east solar limb south of the CME ejecta after the peak of the hard X-ray flare. The left
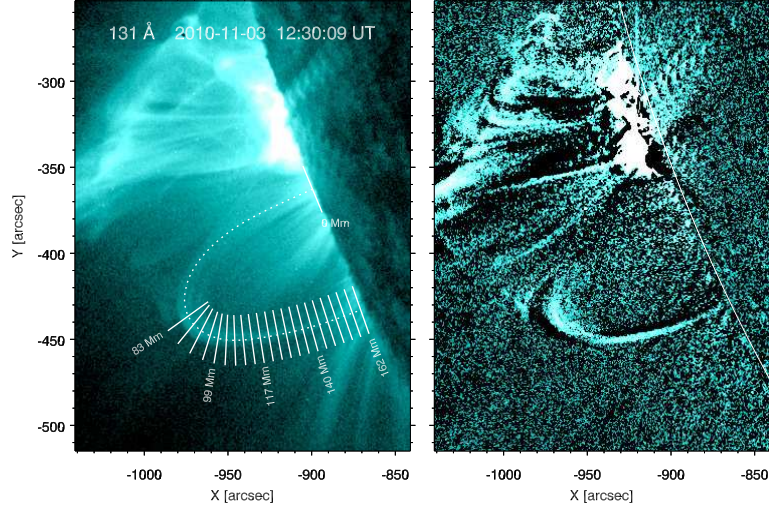
Figure 4.1: SDO/AIA 131 Å image of the November 3 event. *Left*: Image of the event outlining the position of the hot loop below the CME ejecta. Cuts taken to analyse the oscillation are displayed and are separated by ~ 4 Mm. The distance co-ordinate s begins at the top leg and ends at the bottom leg. *Right*: A difference image highlighting the loop oscillation, which was produced by subtracting the image taken at 12:20:57 UT from the one at 12:22:57 UT. The solar limb is indicated by the solid white line.

panel of Figure 4.1 shows an image of the event in the 131 Å bandpass where a loop structure can be seen off the limb below the flare/CME site. The 131 Å emission corresponds to plasma temperatures around 11 MK and just under 1 MK. The 94 Å bandpass corresponds to temperatures around 9 MK and 1 MK. As this loop is not observed in any other of the AIA bandpasses e.g. 171 Å ($\sim$ 1 MK), we expect this loop to be filled with hot plasma.

The right panel of Figure 4.1 shows a difference image in the 131 Å bandpass, which highlights the oscillating loop. During the observation, the loop appears to oscillate in a harmonic overtone, i.e. there is a node along the loop around which the legs of the loop oscillate in anti-phase to one another. The difference image suggests that there is a node at a position of approximately (955″E, 450″S) relative to the Sun centre about which the loop oscillates in anti-phase. We introduce a projected length coordinate s that runs along the loop in the image from the northern to the southern footpoints (as seen in the left panel of Figure 4.1). Figure 4.2 shows time-distance images from cuts made along the loop (see Figure 4.1 left for the cut locations) and a clear phase change is observed with increasing s. Figure 4.2 suggests that the node must lie between approximately $s=103$ Mm and $s=114$ Mm. The node is situated on the southern leg close to the loop top as observed in the
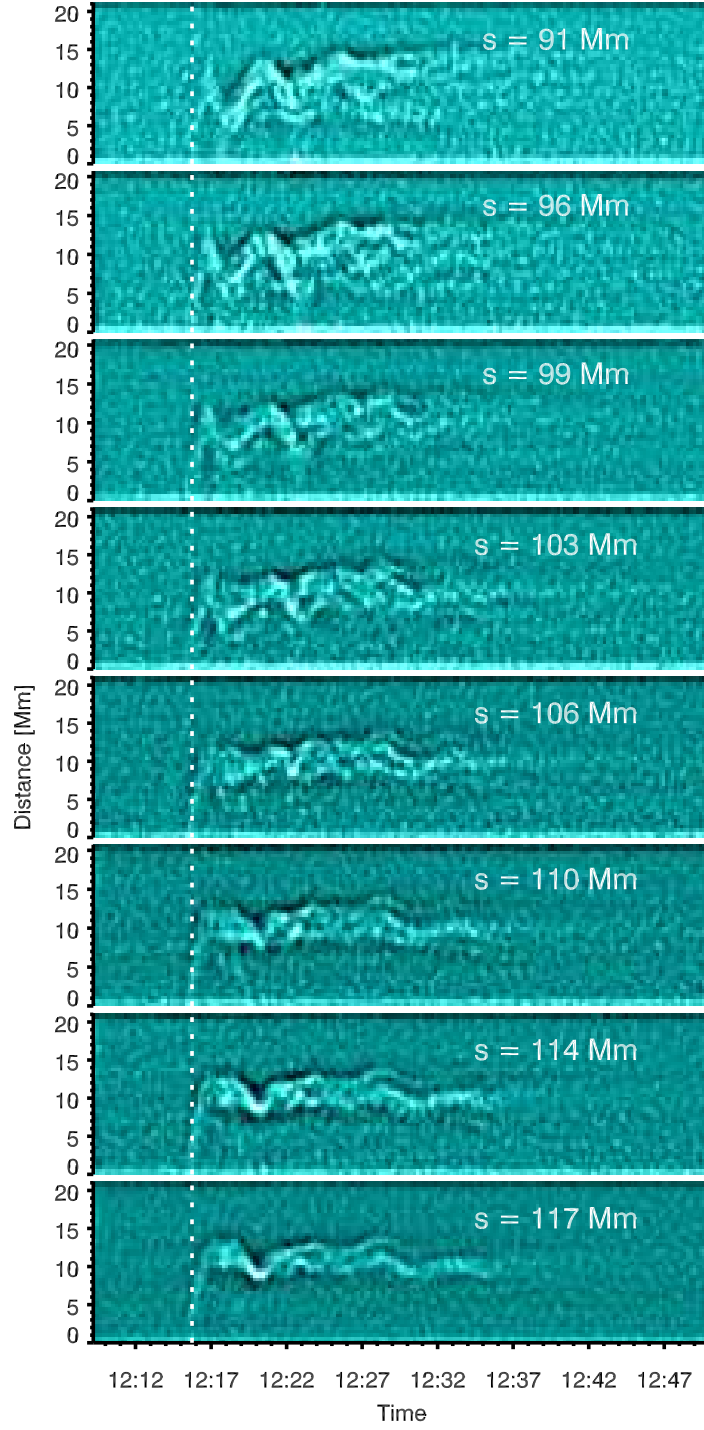
Figure 4.2: Time-distance images extracted from cuts taken along the loop to analyse the oscillation. The cuts span the region where it is expected a node lies. The loop oscillations are observed to undergo a 180° shift in phase in the region between s=103 and s=114 Mm. The vertical dotted line indicates the reference time of 12:16:33 UT.
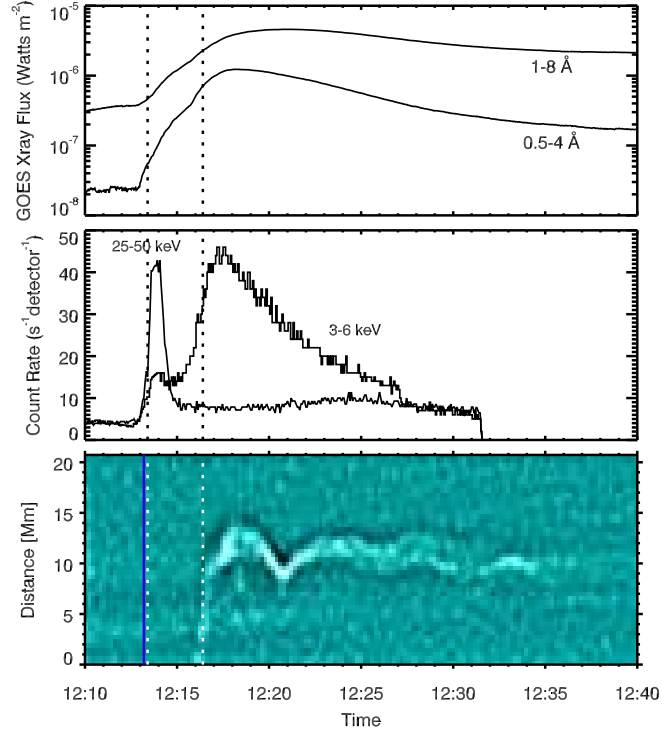
Figure 4.3: *Upper*: GOES (1-8 and 0.5-4 Å) soft X-ray flux. *Middle*: RHESSI (3-6 and 25-50 keV) X-ray flux. The 25-50 keV curve has been scaled by 0.25. *Lower*: An example time-distance cut of the 131 Å loop oscillation. Times of different events are indicated. Blue solid line: approximate start of CME eruption at 12:13:21 UT. Dotted lines indicate the reference times of the oscillations, 12:13:36 UT for the 171 Å loops from White and Verwichte (2012) and 12:16:33 UT for the 131 Å loop.

images. This further suggests that, if this is a second harmonic, the southern loop footpoint is situated behind the solar limb since a node would be expected at the loop top. Because the loop is likely to be partly occulted by the solar disk, using the height above the limb to estimate the radius and hence length of a circular loop will lead to a gross underestimation of the real loop length.

Figure 4.3 shows when the loop oscillation occurred with respect to the flare observed in both hard and soft X-rays (by the Reuven Ramaty High Energy Solar Spectroscopic Imager (RHESSI) and the GOES satellites), in addition to the CME. Table 4.1 lists the events and the time at which they were observed. The peak of the RHESSI hard X-ray flare (25-50 keV) occurs at 12:14 UT, which is just after the start of the oscillations in the 171 Å bandpass. The soft X-ray flare peaks at 12:17:30 UT (RHESSI 3-6 keV) and 12:21 UT (GOES 1-8 Å), where both times are after the start of the 131 Å loop oscillation. The loop appears in the EUV images

Table 4.1: Sequence of events in active region NOAA 11121 on November 3 2010.

Event type	Time (UT)	Instrument
CME	12:13:21	AIA
1 MK loop oscillations	12:13:36	AIA 171 Å
Flare peak	12:14	RHESSI 25-50 keV
Hot loop oscillation	12:16:33	AIA 131 Å
Flare peak	12:17:30	RHESSI 3-6 keV
Flare peak	12:21	GOES-14 1-8 Å

around 12:16:09 UT and is no longer visible by 12:50:09 UT, although the loop fades after approximately 12:40 UT. We do not see any evidence of hot downflows. In addition, we do not observe the loop appearing in colder coronal bandpasses, though there is much line-of-sight confusion that prevents us from being absolutely certain. There is evidence of cool downflows, visible in 304 Å, that may be located in part of the northern leg of the loop which is not visible in the hot coronal bandpasses.

4.4 Time series analysis

Our time series analysis of the loop is performed using the same method as described in Chapter 3. Here cuts are made along the loop, in the direction perpendicular to the loop axis, to extract time-distance images. Any transverse oscillations present will show up in these images, with the clearest results being attainable from cuts that are parallel to the projected oscillation displacement. Time series analysis is performed for the cuts displayed in Figure 4.1 (left). Results for the northern loop leg as observed in the images are not obtained because of the low loop contrast with the background plasma. This means that oscillations are not observed in the time-distance images for this loop leg. The angle of the cuts is varied to check that these cuts are the best, i.e. that they are parallel to the projected displacement direction so that they give the clearest images with the largest oscillation amplitude. A two-dimensional (2D) wavelet transform using the Mexican hat wavelet (Witkin 1983) is used to improve the contrast of the images and distinguish multiple loop strands from one another. A Levenberg-Marquardt least-squares fitting method (Markwardt 2009) is used to fit a damped cosine function to the background-subtracted time series, which in all cases is estimated by eye. The reliability of the time series curves is checked by plotting a marker on the AIA images corresponding to the loop location and playing the images as a movie. The marker can then be observed to follow the
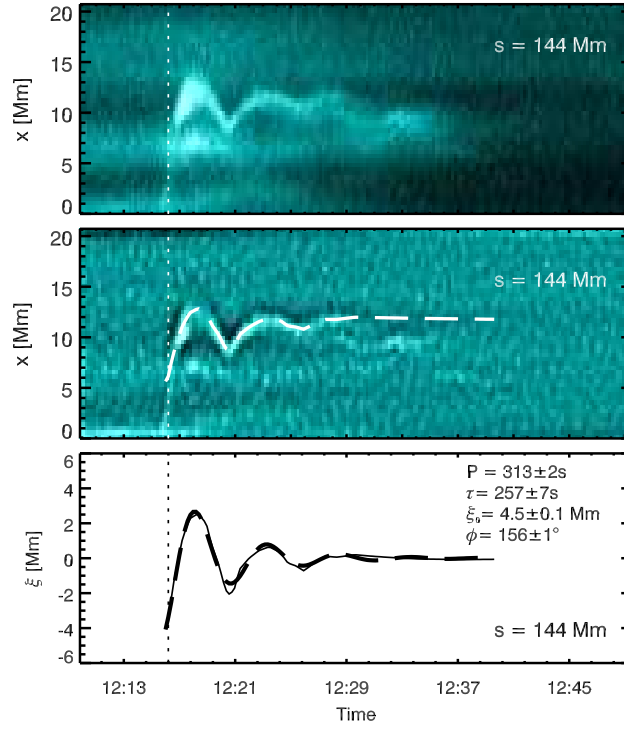
Figure 4.4: *Upper*: Time-distance image extracted from a cut at $s = 144$ Mm. *Middle*: A 2D Mexican hat wavelet transform has been applied to the extracted image to highlight the oscillations present. *Lower*: The time series was de-trended and fitted with a damped cosine function to give information on the amplitude, period, damping time, and phase. The vertical dotted line indicates the reference time of 12:16:33 UT.
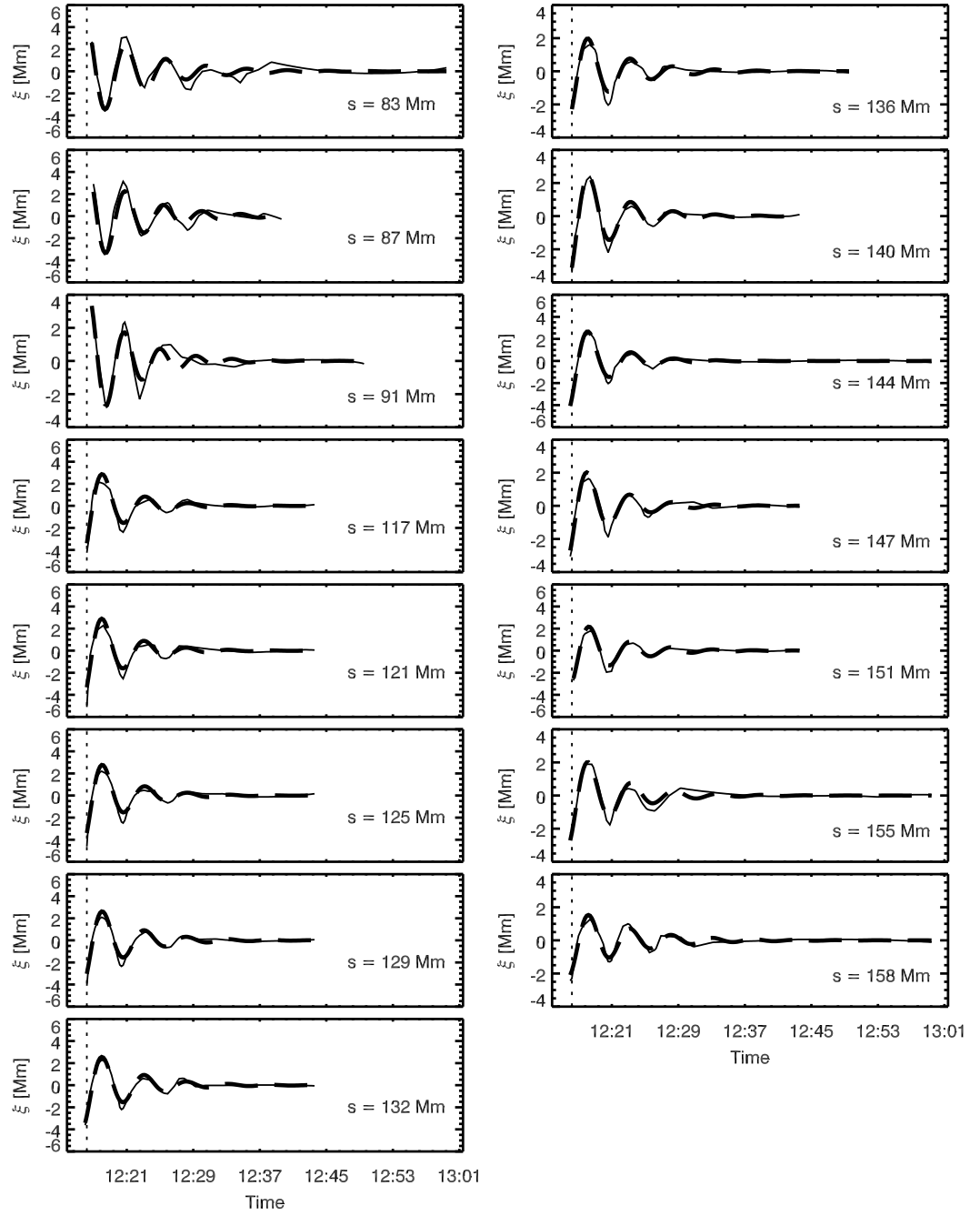
Figure 4.5: Displacement time series curves extracted from the time-distance images for each cut where a damped cosine curve could be reliably fitted. Each time series is de-trended and fitted with a damped cosine function to give information on the amplitude, period, damping time, and phase. The vertical dotted line indicates the reference time of 12:16:33 UT. The s position of the cuts is indicated in each panel.
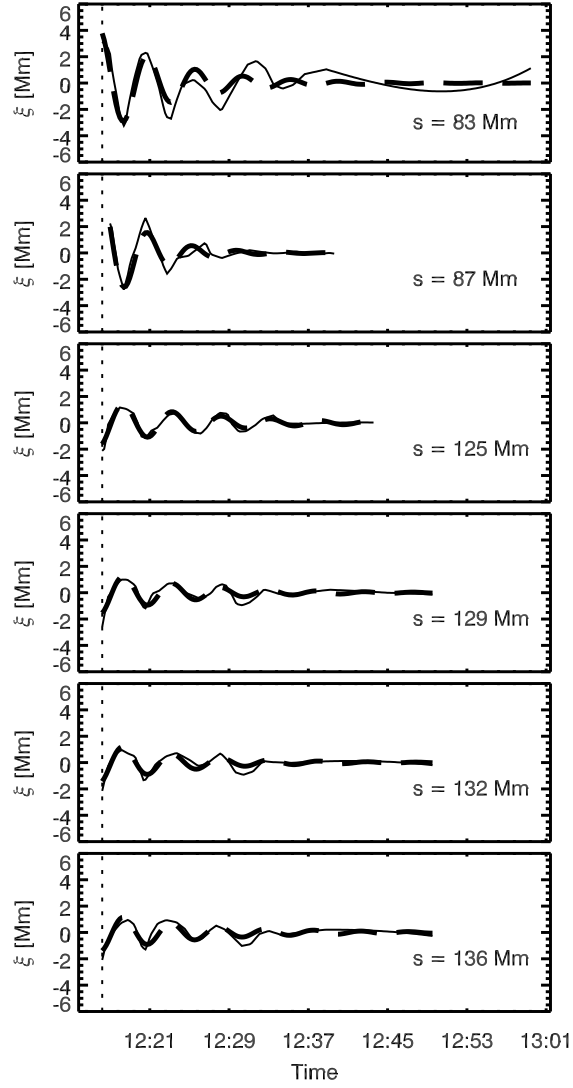
Figure 4.6: Displacement time series curves fitted with a damped cosine curve for the second loop strand observed in six of the time-distance images. Each time series is de-trended and fitted with a damped cosine function to give information on the amplitude, period, damping time, and phase. The vertical dotted line indicates the reference time of 12:16:33 UT. The s position of the cuts is indicated in each panel.

loop as it oscillates. A time series analysis is only performed for cuts taken from the 131 Å bandpass owing to the low contrast of the loop in the 94 Å bandpass, which makes the extraction of oscillatory information unreliable. Figure 4.4 shows an example of the time series analysis method for a cut taken at $s = 144$ Mm. The upper panel of Figure 4.4 shows a time-distance image displaying a damped oscillation, which is highlighted further in the middle panel after the application of the wavelet transform. A displacement time-series is then estimated by eye as shown by the dashed line. This analysis is performed for all cuts shown in Figure 4.1, except for six cuts between 96 Mm and 114 Mm where a node is expected and the oscillation in the cuts is not easily observable. Each of the displacement time curves extracted from the time-distance images that are fitted with a damped cosine curve, are shown in Figure 4.5. In six of the time-distance images, two loop strands are observed. In these cases, oscillatory information for both strands is extracted. The time displacement curves overplotted with a damped cosine fit for the six second strands are shown in Figure 4.6. The lower panel of Figure 4.4 (and Figures 4.5, 4.6) shows an example of the background-subtracted time series that is fitted with a damped cosine curve to determine the oscillation parameters of the period (P), damping time (τ), amplitude (ξ), and phase (ϕ). Figure 4.7 shows the resulting loop parameters P, τ, ϕ, and ξ_0 with respect to s along the loop. The triangles show the results for the second loop strand (observed in six of the time-distance images). The error bars display the errors returned by the fitting routine. Displayed in the figures for τ and P are the mean and standard deviations for the first strand. The time series analysis for the first (second) strand gives a period of $P = 302 \pm 14$ s (291 ± 9 s) and a damping time of $\tau = 306 \pm 43$ s (487 ± 125 s). The errors were determined from the standard deviation in the results.

The upper panel of Figure 4.7 shows that ϕ undergoes a 180° phase shift along the loop, which is a clear signature that what we observe is a harmonic overtone. We would expect the amplitude of the oscillation to decrease as we go towards the node position, although the oscillations in the cuts close to the node appear messy in the time-distance images with overlapping loop strands. Therefore, reliable time-series information around the node position is not obtained. Figure 4.2 shows time-distance slices close to the node point (between approximately 103 Mm and 114 Mm). This figure shows that the oscillations do not completely die away but that the amplitude does decrease and oscillations are harder to extract from the images. It may be that there are still some amplitude signatures from the fundamental mode (which would be a maximum at the loop top, i.e. a maximum at the second harmonic node) or other higher harmonics that do not allow the amplitude to go to
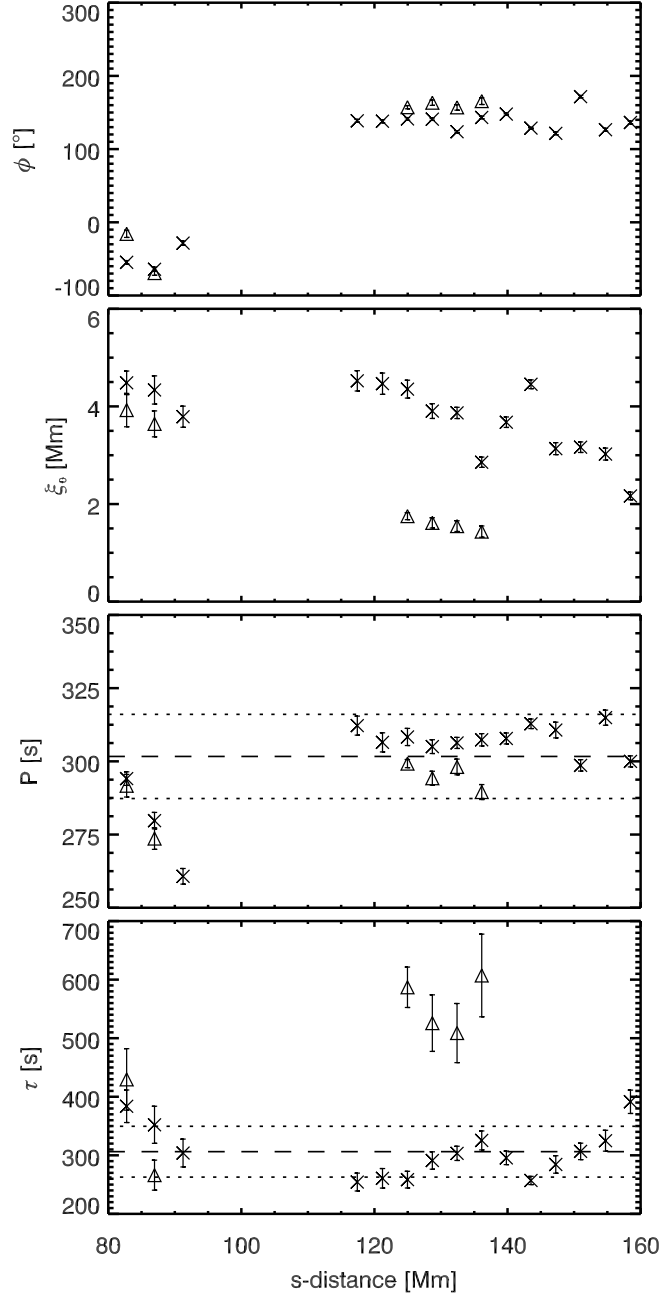
Figure 4.7: Oscillation parameters, phase (ϕ), projected displacement amplitude (ξ), period (P), and damping time (τ) plotted as a function of s along the loop. The triangles show the results obtained for the second loop strand observed in six of the time-distance images. The error bars show the errors given by the fitting technique. The horizontal dashed line in the bottom two plots indicate the mean value of P and τ for the first loop strand and the horizontal dotted lines indicate the standard deviation. The reference time is 12:16:33 UT.

93

zero at this point. The observations indicate that the southern footpoint is situated behind the solar limb. The amplitude does decrease as would be expected towards the southern footpoint. The period and phase of the second strand (indicated by the triangles) are consistent with those of the first strand. The periods and damping times are mostly within one standard deviation of the mean.

4.5   Loop intensity

To investigate any variations in the intensity of the loop oscillation, intensity is extracted at each point along the displacement time-series for each of the cuts. Figure 4.8 shows examples of the extracted intensity as a function of time for different values of s, and at a first glance resembles the signatures of flare light-curves. The intensity rises sharply and then diminishes more slowly. It also seems to diminish more slowly towards the loop top compared to lower down the southern loop leg towards the footpoint. Oscillatory signatures can also be seen in the extracted intensity, particularly at $s = 158$ Mm.

The oscillations present in the intensity are investigated further by de-trending the intensity and fitting a damped cosine curve using the same method as for the time series analysis. Figure 4.9 shows this analysis performed for cuts located at $s = 87$ Mm and $s = 158$ Mm (a damped cosine could not be fitted to the de-trended intensity from cuts at any other values of s). Here the location of the time series has been overplotted on the time-distance images (panels a, c) with the extracted intensity time-series displayed below (panels b, d). The intensity time-series is background-subtracted and then normalised by the background. Panels b and d show significant intensity variations with respect to the background intensity, between 10% and 30% for the peaks of the oscillations. The periods of both these intensity oscillations, 318 ± 4 s and 275 ± 3 s, lie just outside the displacement time-series period of 302 ± 14 s and hence are broadly consistent. The intensity oscillations are approximately in anti-phase with the displacement time-series analysis for their respective cuts. This means that as the loop displacement is upwards (downwards), the intensity decreases (increases).

We also investigate the intensity along the loop axis as a function of time as shown in Figure 4.10. The cut has a width of 81 pixels ($48.6''$) which ensures that the whole of the loop oscillation is captured at each time. The time-distance cut is averaged over this width to increase the signal to noise. The raw time-distance image is averaged in time and then this average intensity is subtracted from the raw time-distance image. This helps to highlight any features that may be present. Figure 4.10 shows

94
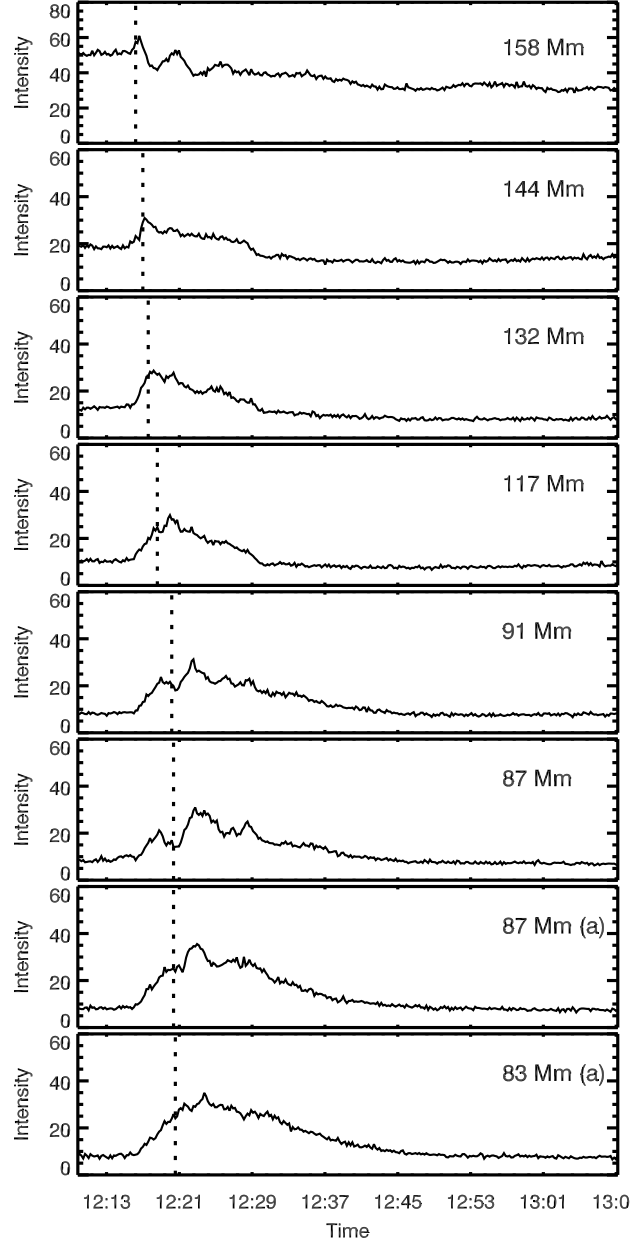
Figure 4.8: Intensity along the loop oscillation path extracted from time-distance images by taking the intensity at each point along the displacement time curves for eight values of s along the loop. (a) indicates that the intensity is extracted from the second strand which was observed in six of the time-distance images, the results of which are represented as triangles in Figure 4.7. The vertical dotted line represents the position in time of the linear fit to the intensity shown in Figure 4.10.

95
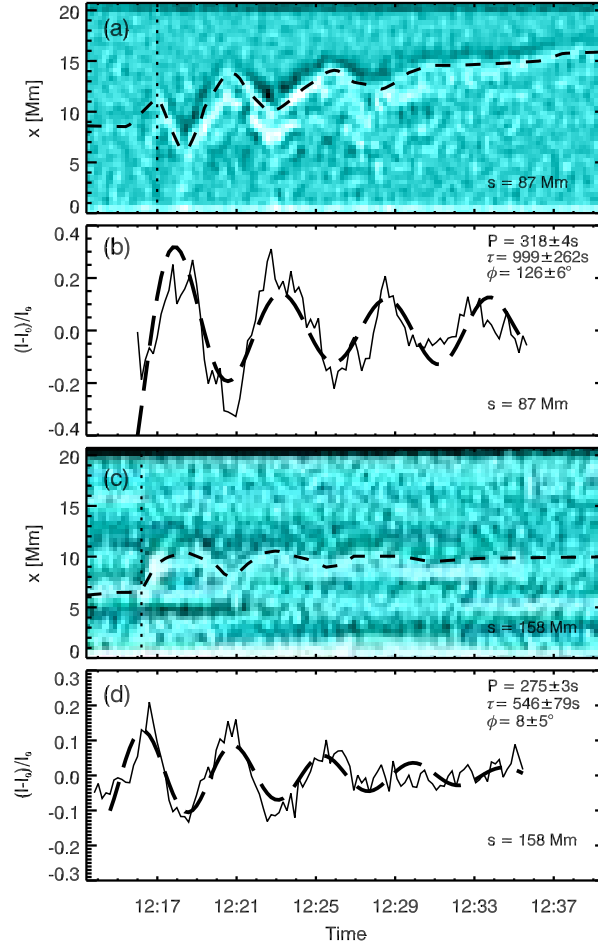
Figure 4.9: Analysis of the intensity time-series for cuts at $s = 87$ Mm (a, b) and $s = 158$ Mm (c, d). (a) and (c) show the time-distance images with the oscillation time-series overplotted. The vertical dashed lines indicate the start of the oscillation. (b) and (d) show the intensity time-series extracted from the time-distance images. The thick dashed line is the damped cosine fit to the intensity.

96
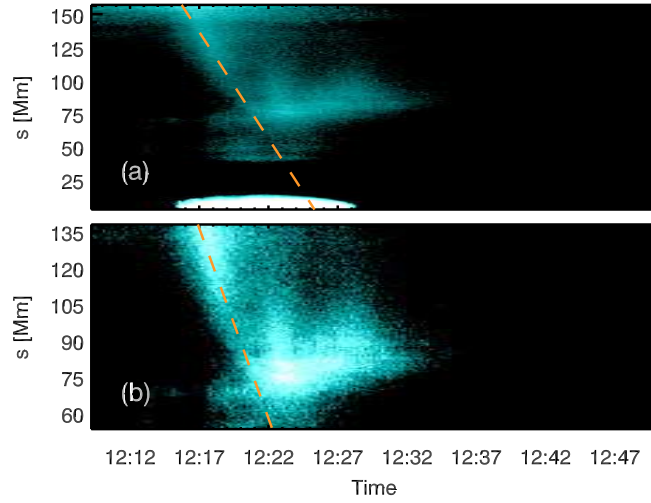
Figure 4.10: Intensity along the loop plotted as a function of time. The intensity averaged in time has been subtracted from each time slice. (a) The linear trend (orange dashed line) gives a projected speed of 212 km s^{-1}. (b) Zoomed-in version of the top figure giving a projected speed of 206 km s^{-1}. This speed can be approximately corrected for the projection using the 3D estimate of the loop from the STEREO-B/SDO comparison to give a speed of approximately 470 km s^{-1}, close to the sound speed of 500 km s^{-1} at 11 MK.

that intensity first appears near the southern footpoint and then 'flows' along the loop towards the top. The loop has then almost disappeared by 12:40 UT. A linear trend is fitted to the intensity brightening (dashed orange line in Figure 4.10) with the gradient of the intensity front giving projected speeds of 212 km s^{-1} (panel a) and 206 km s^{-1} for a shorter path (panel b).

4.6 Loop geometry and mode modelling

Comparing the loop observed from the viewpoint of SDO with that from another viewpoint, such as the Solar Terrestrial Relations Observatory (STEREO), can allow the 3D loop geometry to be estimated. Loop points are chosen in the STEREO-B viewpoint with the Extreme Ultraviolet Imager (EUVI) (Howard et al. 2008), which are then projected onto the other SDO/AIA viewpoint assuming a planar loop model. By comparing the projected loop points for the two viewpoints with an imposed (user-defined) inclination angle (θ) with respect to the photospheric normal, θ can be constrained. In this observation, the loop is only seen in the 131 Å and 94 Å AIA bandpasses and not observed in the EUVI channels, although possible footpoint locations are identified in the EUVI images. By comparing the
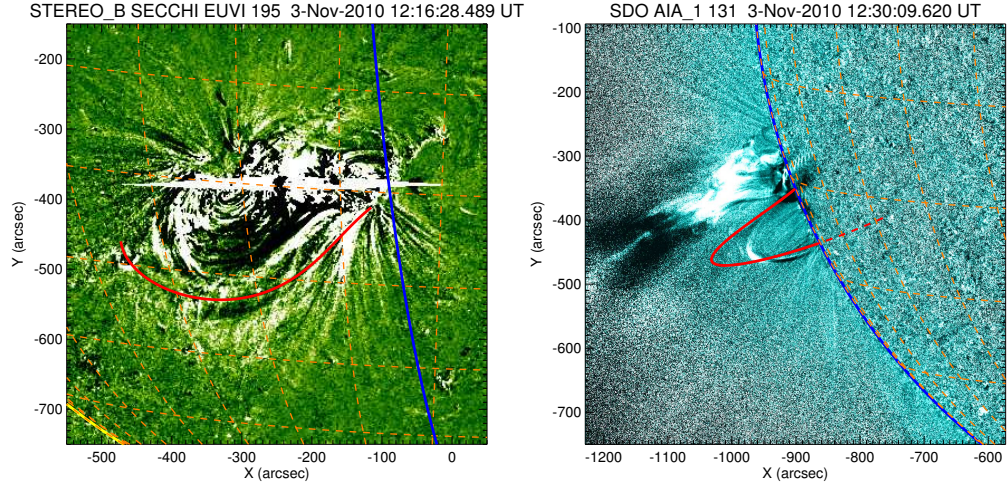
Figure 4.11: *Left*: STEREO-B EUVI 195 Å difference image (at the time indicated with respect to 12:11:28 UT). *Right*: SDO AIA 131 Å image ratio (at the time indicated with respect to a previous image at 12:18:57 UT). Overlaid are the loop trace (red thick line with dashed lines for portion behind the limb in *Right* panel), the SDO limb (blue) and heliospheric grid lines spaced by 10 degrees (orange dashed lines).
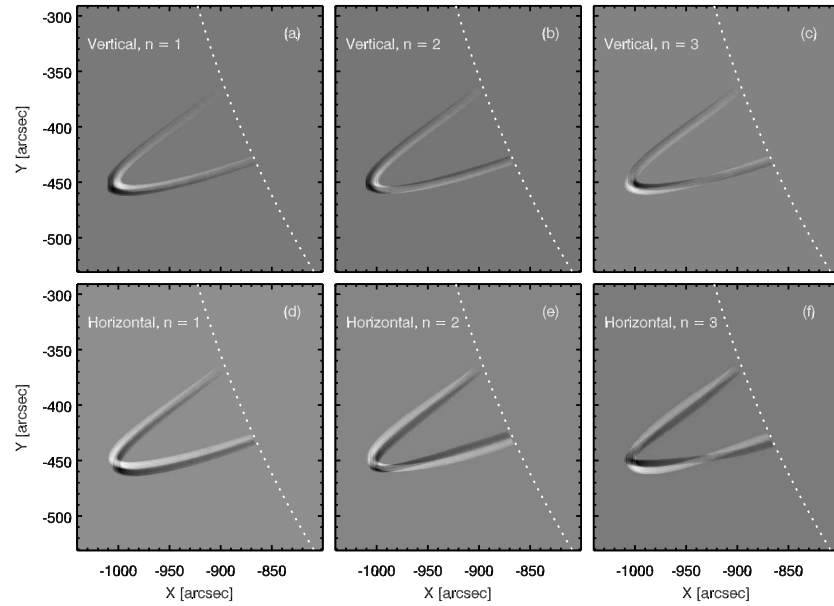
Figure 4.12: Difference images of the modelled horizontally and vertically polarised transverse modes in the AIA viewpoint. *Top*: Vertically polarised a) first harmonic, b) second harmonic, c) third harmonic. *Bottom*: Horizontally polarised d) first harmonic, e) second harmonic, f) third harmonic. The dotted line indicates the solar limb.

geometry of the CME (observed in both the cooler and hotter bandpasses) in both AIA and EUVI and knowing the position of the loop relative to the CME in the AIA images, an estimate of the geometry of the hot loop is obtained. Figure 4.11 shows the estimated loop geometry from both the STEREO and SDO viewpoints which does not represent a good fit to the observed loop, however it is the best estimate available for this example. Since the loop is not observed in the EUVI images and its geometry is inferred from that of the CME, this geometry is the most likely one and not an absolute model of the loop. Using this technique, an optimal inclination angle of $-6°$ and a loop length of 466 Mm is found. Figure 4.11 shows that the 3D geometry estimate does not precisely match the loop observed in the AIA images. This is to be expected since, although reliable estimates for the footpoint locations are found, it is difficult to follow a loop path in the STEREO images. In addition a planar loop model is assumed, which may not be an accurate assumption in this case.

With an estimate of the 3D geometry, different modes of transverse oscillations are modelled to see whether any of them match the observed loop motion. The loop is modelled for the AIA viewpoint and is uniformly filled to a radius of 3 Mm and a contrast of 10 with the background. Details of the modeling procedure are given in Section 3.5.1. The first three harmonics of both the horizontally and vertically polarised kink modes are modelled with an amplitude of 4.7 Mm. Figure 4.12 shows the difference images for each of the modelled modes. In the AIA difference image (right panel of Figure 4.1), one node is clearly observed on the southern leg of the loop, although the northern leg is not observed because of the poor contrast. The modelled modes that most closely match the observations are the n=2 and n=3 vertically polarised modes (Figure 4.12b, c). The observation along with the forward modelling suggests that this loop is oscillating as a vertically polarised second or third harmonic. If it is a third order harmonic, there should be a node situated on the northern leg, which is not visible as the contrast between the loop and the background plasma diminishes.

4.7 Discussion

Vertically polarised TLOs were previously reported by Wang and Solanki (2004), Mrozek (2011), and Aschwanden and Schrijver (2011). Key questions from this observation are (1) what are the conditions and/or mechanisms behind the excitation of this oscillation? (2) why is a vertical harmonic overtone selected as the mode of oscillation? and (3) why is the loop only observed in the hot bandpasses?
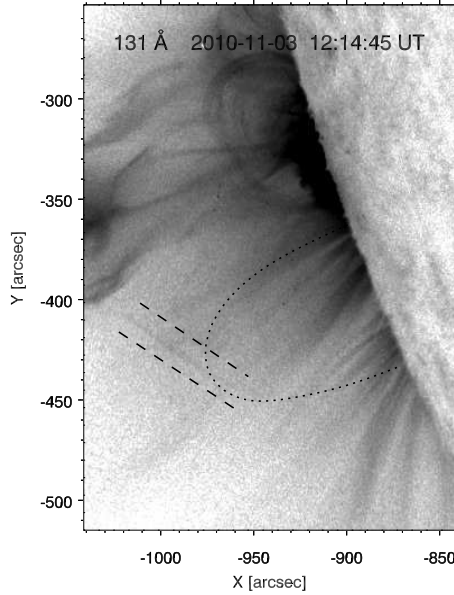
Figure 4.13: An AIA image taken at 12:14:45 UT on 3 November showing a strand that appears to connect the CME with the region where the hot loop appears a short time later. The loop position at a time of 12:30:09 UT is indicated by the dotted line and the strand is located between the two dashed lines.

4.7.1 Loop generation and excitation

Both the CME ejecta and the loop are observed in the 94 Å and 131 Å bandpasses suggesting that they are directly linked to one another and that the loop is generated by the CME. Figure 4.13 shows a strand originating from the direction of the CME towards the location of the loop just before the loop appears at about 12:16 UT. The position of the loop inferred from Figure 4.1 is indicated by the dotted line. The strand appears to link the location of the top of the loop, as observed with AIA, to the CME. This may indicate that the loop is directly formed by the CME as a result of reconnection processes forming and releasing field lines that are then filled with hot plasma at the footpoints.

Figure 4.10 shows that hot plasma is injected into the loop from the southern footpoint, allowing it to become visible in the hot AIA channels. This asymmetric plasma heating of the loop has a projected speed of about 210 km s^{-1}. Using the 3D loop geometry found in Section 4.6, this speed can be approximately corrected for the projection since in the AIA image the distance to the loop top is 80 Mm, whereas in the modelled loop it is about 180 Mm. This gives a corrected speed of approximately 470 km s^{-1}, which is close to the sound speed of 500 km s^{-1} for an 11 MK plasma. We might then expect the hot plasma to cool in time and become

100

visible in the cooler AIA bandpasses, but this is not observed. It may be that the plasma cools on a timescale that is much shorter than can be observed owing to a thermal instability and becomes directly visible in cooler bandpasses such as 304 Å. We conclude that the upflow is consistent with explosive chromospheric evaporation and there is some evidence at 304 Å of gentle, cool condensating downflows (e.g. Fisher et al. 1985; Milligan et al. 2006; Milligan and Dennis 2009). Explosive chromospheric evaporation occurs when the chromosphere is impulsively heated by non thermal electrons that are accelerated down magnetic field lines during the impulsive phase of a flare. The electrons will collide with the dense chromospheric plasma and loose their energy via coulomb collisions resulting in plasma heating. This rapid heating up to coronal temperatures causes the plasma to expand into the corona at velocities on the order of hundreds of km s^{-1} (Fisher et al. 1985).

The observed hot plasma injected can be expected to excite a fundamental slow magneto-acoustic oscillation in the loop (Wang et al. 2003b; Nakariakov et al. 2004; Tsiklauri et al. 2004). For a loop length of $L = 466$ Mm and sound speed of $C_s = 500$ km s^{-1}, we found a period of approximately 30 min, which is longer than the duration of the observation when the loop is effectively visible. Therefore, we found no evidence of a slow wave in this loop.

The excitation time of the transverse loop oscillation corresponds to the gradual phase of the flare rather than the earlier impulsive phase of the flare (see Figure 4.3). A possible explanation for the excitation of this TLO may therefore be as follows. Field lines form from a reconnection process creating a loop structure that is held at the loop top. The top is then released (or even pushed down) causing the loop to oscillate as a vertical TLO. This is a more likely scenario than the loop being hit by the blast wave (as for the TLOs observed in 171 Å) as the loop appears to be released from the top rather than be hit from the side. The 3D forward-mode modelling (Figure 4.12) also supports this interpretation, suggesting that the loop is a vertical mode oscillating as a second or third harmonic. The numerical simulations of a CME eruption from an anemone active region (a unipolar region embedded in the opposite polarity open field region) by Lugaz et al. (2011) shows a two-stage reconnection process that includes the formation of post flare loops (see their figure 5). Although there are differences between the numerical simulation and this observation, a comparison shows that reconnection could play an important role in the formation and wave excitation of the hot loop.

Numerical simulations of vertically polarised modes have been conducted where a pulse is generated below the loop, often modelled in slab geometry (Selwa et al. 2006; Gruszecki et al. 2006; Wasiljew and Murawski 2009). This results in fundamental or

Table 4.2: Summary of the properties and wave speeds of the two loop strands for both a second and third order harmonic TLO

Harmonic		First strand	Second strand
	P	302 ± 14	291 ± 9
	τ	306 ± 43	487 ± 125
n = 2	V_{ph}	1540 ± 170	1600 ± 170
	V_{A0}	1090	1130
	β	0.3	0.2
n = 3	V_{ph}	1030 ± 110	1070 ± 110
	V_{A0}	730	760
	β	0.6	0.5

[a] Parameters listed in the table: period (P), damping time (τ), phase speed (V_{ph}), minimum internal Alfvén speed (V_{A0}). P and τ have units of s and all speeds have units of km s^{-1}.

second-harmonic vertical modes (depending on the location of the generated pulse), or even mixed modes of both vertical and horizontal polarisations. This observation differs from previous simulations in that the excitation of this loop comes from above rather than below the loop. It is possible that what we observe is a mixed mode oscillation but that it is dominated by the vertically polarised second or third harmonic. That the loop oscillation amplitude does not diminish completely to zero at the node point (see Figure 4.2) also supports this interpretation.

4.7.2 Wave speeds

Assuming a loop length $L = 466$ Mm with a nominal 10% error, the phase speed and the minimum value for the internal Alfvén speed can be estimated for different order harmonics. Table 4.2 gives a summary of the wave speeds calculated for both loop strands, assuming either a second or third order harmonic. The phase speed was calculated as $V_{ph} = 2L/nP$, where n is the order of the harmonic and an estimate of the minimum value for the internal Alfvén speed is given by $V_{A0} = V_{ph}/\sqrt{2}$ assuming that V_{ph} is equal to the kink speed. For a sound speed of 500 km s^{-1} and an 11 MK plasma, the maximum plasma-β is given by $\beta = (2/\gamma(C_s^2/V_{A0}^2) \approx 0.6$ for the first strand (n=3). Here both V_{ph} and V_{A0} are above the sound speed for an 11 MK plasma.

4.7.3 Intensity variations

There are various possible explanations for the intensity variations shown in Figure 4.9. Firstly, intensity variations may be caused by line-of-sight effects either as a result of the oscillating loop overlapping static background structures or the change in column depth of the loop along the line of sight as it oscillates back and forth (Cooper et al. 2003; Verwichte et al. 2009, 2010; White and Verwichte 2012). This may be particularly true for the case $s = 158$ Mm as this cut is taken close to the solar limb where several structures can be seen extending radially outwards. The forward modelling of the oscillating 3D loop based on a uniformly filled loop does show some variations in intensity that would support this explanation. Secondly, the mode may couple linearly with a slow mode of the same period (Terradas et al. 2011). For this, we would expect the wavelength of the slow mode to be $\lambda_s = C_s(2L/3V_{ph}) = 160$ Mm. We do not detect spatial intensity variations on this length-scale along the loop. Thus, we rule out linear coupling in this case. Finally, a vertically polarised mode inherently perturbs the density as both the loop length and loop cross-section vary (Wang and Solanki 2004; Verwichte et al. 2006a,c; Díaz 2006). Verwichte et al. (2006a) showed that the intensity perturbation for small amplitude oscillations averaged over the loop width is related to the radial displacement as $\delta I/I_0 \approx -4\xi/R$. For a radial displacement of 4-6 Mm, an approximate loop radius of $R=L/\pi=150$ Mm, this predicts a relative intensity variation of $\delta I/I_0 = $ -0.1-0.2. The observations indeed show an intensity oscillation that is in anti-phase with the displacement with a relative amplitude between 0.1-0.3. We therefore conclude that the detected intensity oscillations are consistent with a vertically polarised TLO.

Chapter 5

Anti-phase signature of flare generated transverse loop oscillations

5.1 Chapter Overview

In this chapter an SDO/AIA observation of transverse loop oscillations (TLOs) displaying anti-phase oscillations that are initially directed inwards towards each other after an impulsive flare event is presented. This is an unusual observation because from previous studies (e.g. Aschwanden et al. 2002; White and Verwichte 2012) we would expect the loops to begin oscillating in phase. The local magnetic topology of the active region is investigated to help explain the origin of these unusual oscillations and show that TLOs are a potential tool for identifying dynamic reconnection processes in active regions.

5.2 Introduction

Traditionally it has been believed that TLOs are excited by an impulsive event such as a solar flare which can produce a blast wave, perturbing the surrounding corona (Aschwanden et al. 1999b; Nakariakov et al. 1999; Hori et al. 2005; Van Doorsselaere et al. 2009; Verwichte et al. 2010; Tothova et al. 2011; Wang et al. 2012). However, as discussed in Chapter 4, a TLO observed in a post flare hot (> 10 MK) loop was proposed to have a different excitation mechanism where the reconnection processes are thought to play an important role in both the formation of the loop and the perturbation of the transverse oscillation. Impulsively excited

TLOs are usually observed to have their initial displacement away from the source of excitation and then to damp rapidly back to an equilibrium which may or may not be aligned with their initial start position e.g. White and Verwichte (2012). Anti-phase transverse oscillations in coronal loops have been observed by Schrijver and Brown (2000). They observe transverse oscillations which occur after a flare with the Transition Region and Coronal Explorer (TRACE) spacecraft. To explain the anti-phase behaviour of the oscillations they suggest that the magnetic topology of the active region plays an important role. They describe how a small shift of a null point will cause a field line passing close by to experience a considerable change in position, where the direction of motion of the field line will be affected by the direction of shift of the null point. In general the magnetic topology of active regions has not been of interest when discussing TLOs and their excitation, however the local magnetic topology might also help to explain why some active region loops oscillate while other loops in the same active region do not (the so called 'selectivity problem') even though they appear to be similar structures. Anti-phase oscillatory signatures have also been detected in Solar Ultraviolet Measurements of Emitted Radiation (SUMER) spectral data during a solar flare on the east solar limb by Kliem et al. (2002). They observe coronal material in hot lines (Fe XXI formed at $\sim 10^7$ K) and cool lines (C II formed at $\sim 2 \times 10^4$ K) that show anti-phase behaviour in their Doppler line shifts. Like TLOs, these Doppler shift oscillations are observed to damp on short time-scales, however they rule out TLOs as an explanation in this case because the anti-phase Doppler line shifts are observed at low coronal heights with amplitudes that were three times larger than the largest TLO amplitudes detected by TRACE (Aschwanden et al. 2002). Large displacements associated with TLOs have since been reported by Verwichte et al. (2010). Alternative explanations in terms of impulsively generated propagating waves or relaxation oscillations of flows were proposed instead as the cause of the anti-phase oscillations observed in the different temperature lines.

5.3 Overview of the observations

We study transverse loop oscillations (TLOs) present in active region NOAA 11476 on 2012 May 8. The active region is situated on the NE solar disk and produced a number of flares over several hours including an M1.4 GOES class flare peaking at 13:08 UT in the soft X-ray channel. The flaring associated with the most energetic particles peaked at 13:07 UT (N13° E44°) as recorded in Hα ground-based observations (San Vito, Italy) and as measured in hard X-rays (25-50 keV) by the Reuven
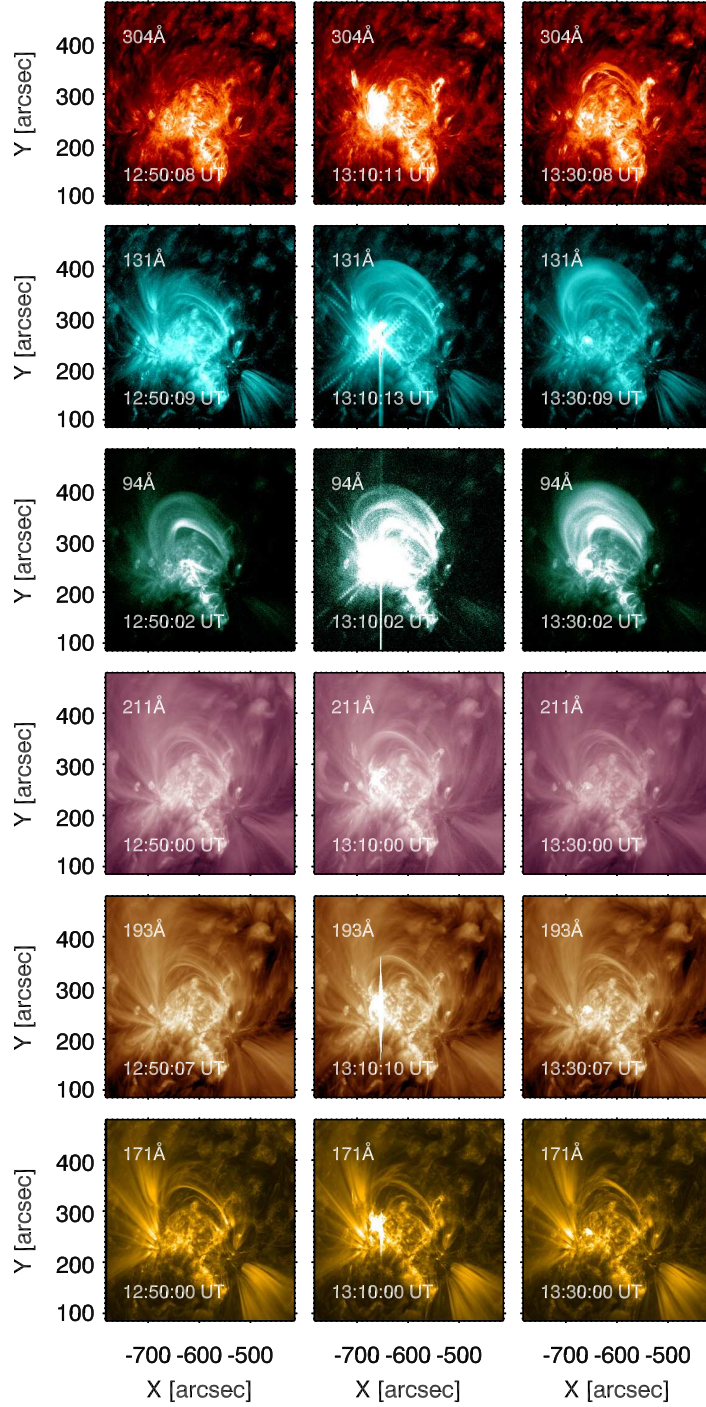
Figure 5.1: Active region 11476 on 2012 May 8 displayed in six extreme-ultraviolet SDO/AIA bandpasses for three different times covering the duration of the flare and transverse loop oscillations. *Left*: 12:50 UT, *Middle*: 13:10 UT and *Right*: 13:30 UT. Transverse loop oscillations are reliably observed in the 171 Å, 193 Å and 211 Å bandpasses.
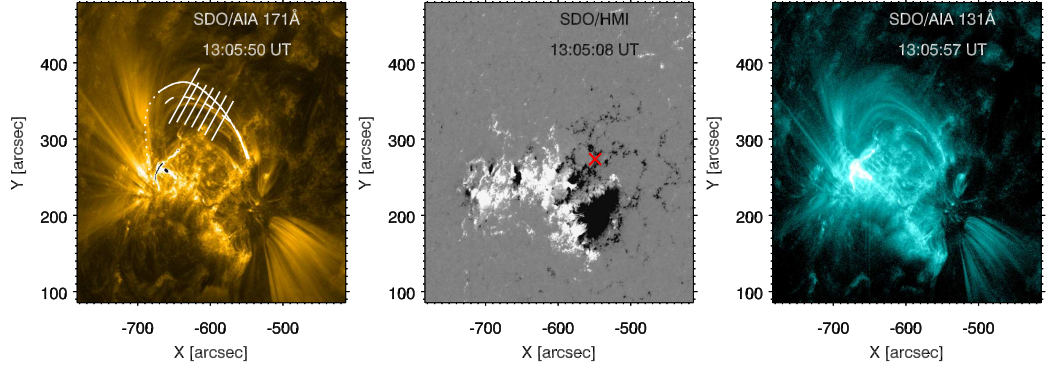
Figure 5.2: *Left*: 171 Å AIA image of the active region. The loops studied in three SDO/AIA bandpasses for their transverse oscillations are indicated by the curved lines; 171 Å (dashed line), 193 Å (solid line) and 211 Å (solid and dotted line). The straight solid lines are the cuts taken to analyse the transverse oscillations. *Middle*: SDO/HMI Magnetogram showing the line of sight magnetic field at the photosphere. The red cross marks the position of the western loop footpoints. *Right*: 131 Å AIA image. The flare ribbons make an inverted Y shape.
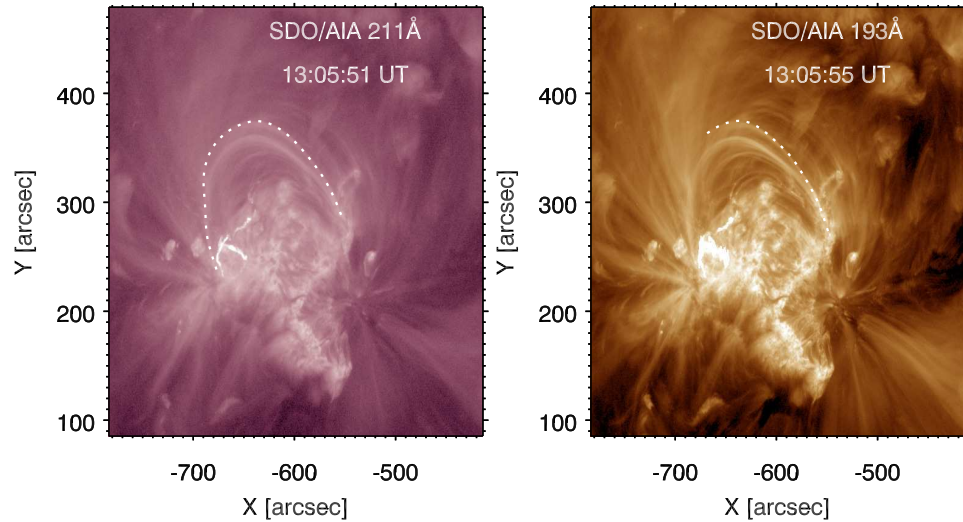
Figure 5.3: *Left*: 211 Å and *Right*: 193 Å AIA images of the active region. The loops studied for their transverse oscillations are indicated by the dotted lines.

Ramaty High Energy Solar Spectroscopic Imager (RHESSI). The event is observed by SDO/AIA and is shown in six of the AIA channels (171 Å, 193 Å, 211 Å, 131 Å, 94 Å and 304 Å) in Figure 5.1. Three images of the active region in each of the bandpasses are displayed before (12:50 UT) and after the flare peak (13:10 UT, 13:30 UT). AIA's unique capabilities allow the event to be observed in a wide temperature range with time cadence of 12 s and a pixel resolution of 0.6″. Loop structures are visible in all bandpasses and a band of hot emission in the vicinity of the loops in the 131 Å and 94 Å channels is observed. In addition this hot emission is seen in Hinode X-ray Telescope (XRT) images both before and after the flare eruption. Fan like structures are visible in multiple AIA channels either side of the loop structures which exist before and after the eruption. The active region is also visible on the limb with the Extreme Ultraviolet Imager (EUVI) on the Solar Terrestrial Relations Observatory (STEREO) B spacecraft (Howard et al. 2008) however individual loops observed by AIA are difficult to identify in the EUVI images. The field of view of the EUV imaging spectrometer (EIS) on Hinode was just below the loop structures so spectral information of the loops is not available.

Figure 5.2 shows the active region before the flare peak in the 171 Å (Left panel) and 131 Å (Right panel) AIA bandpasses. Both images show fan (with respect to the field of view of the figure) and closed loop structures situated above a complex (Hale sunspot classification of $\beta\gamma/\beta\gamma$) magnetic field configuration shown by a Magnetogram from the Helioseismic and Magnetic Imager (HMI) on SDO (Middle panel). The flare is located at position (-660″E, 260″N) and during the eruption, flare ribbons create an inverted Y shape structure that is seen in the EUV images. The HMI Magnetogram indicates that the flare ribbons are located on or close to polarity inversion lines, in a region where there is negative flux surrounded by positive flux. Figure 5.3 shows the active region and the loops studied in the 193 Å and 211 Å bandpasses.

The flare eruption excites several loops to oscillate with transverse motions which we study in more detail. Paths showing the loop positions are shown in Figure 5.2. The lower loop indicated by the dashed line is observed particularly strongly in the 171 Å bandpass while the loop above this indicated by the solid and dotted lines is seen most clearly in the 193 Å and 211 Å channels respectively. The loop paths indicate how much of the loop is visible in the images before the line of sight confusion renders it too difficult to identify individual loops. The loops observed in 193 Å and 211 Å have overlapping loop paths and displacement time series positions. This suggests that they are likely to be the same loop structure that has multi-thermal components. The western loop foot points appear to be the same for each
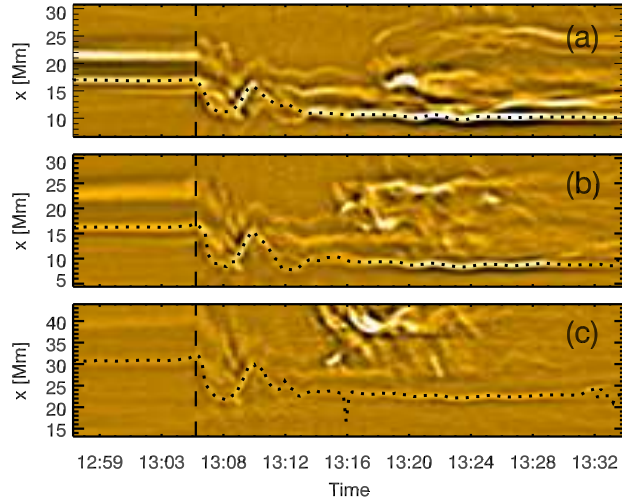
Figure 5.4: Example space-time images from a cut taken across the transversely oscillating loops is shown for the 171 Å bandpasses. The images have been wavelet filtered using the Mexican hat wavelet. The reference times of 13:06 UT shown by the vertically dashed lines indicates the start of the oscillations. a-c correspond to cuts 3-1. The cuts run from no. 1 on the left to no. 7 on the right in Figure 5.2.

of the loops and originate in a region of negative polarity above the large sunspot region (indicated by the red cross in figure 5.2), however the location of the eastern foot points are hidden by many other intense structures in the line of sight. From studying the data we expect the eastern foot points to lie close to the site of the EUV flare emission. The TLOs fit the typical characteristics of previously observed TLOs i.e. an impulsive trigger and short damping time-scales. During the flare, material visible in all AIA channels is ejected and observed to follow field line trajectories, flowing along and then back down towards the chromosphere. Interestingly the loop observed in the 193 Å and 211 Å channels displays impulsive oscillations that are initially directed south in the AIA field of view, where as the loop in the 171 Å is pushed away from the southern source region as we would expect for an impulsive event. This inwardly directed anti-phase behaviour is unusual and we investigate this intriguing observation further.

5.4 Analysis

Analysis of the transverse oscillations is conducted using the method of taking space time cuts parallel to the projected loop displacement and fitting the background sub-tracted displacement time series with a damped cosine curve to obtain the oscillation
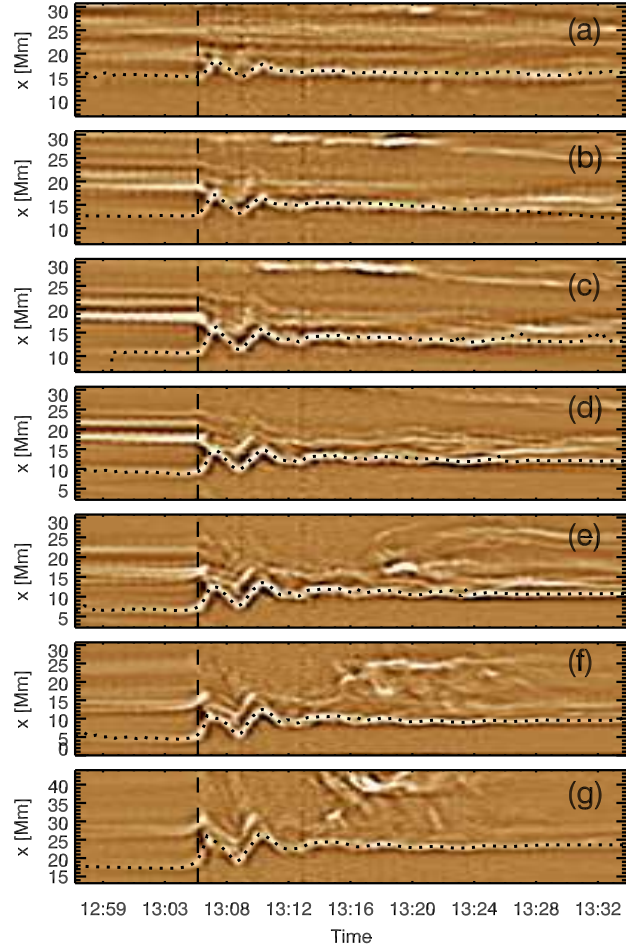
Figure 5.5: Example space-time images from a cut taken across the transversely oscillating loops is shown for the 193 Å bandpasses. The images have been wavelet filtered using the Mexican hat wavelet. The reference times of 13:06 UT shown by the vertically dashed lines indicates the start of the oscillations. a-g correspond to cuts 7-1. The cuts run from no. 1 on the left to no. 7 on the right in Figure 5.2.
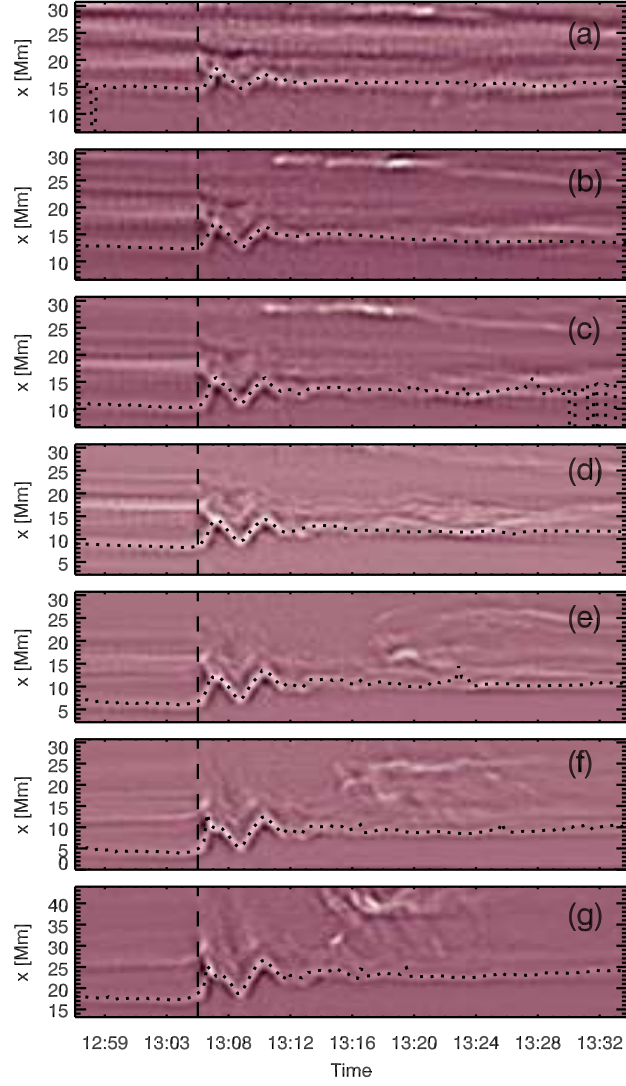
Figure 5.6: Example space-time images from a cut taken across the transversely oscillating loops is shown for the 211 Å bandpasses. The images have been wavelet filtered using the Mexican hat wavelet. The reference times of 13:06 UT shown by the vertically dashed lines indicates the start of the oscillations. a-g correspond to cuts 7-1. The cuts run from no. 1 on the left to no. 7 on the right in Figure 5.2.

111
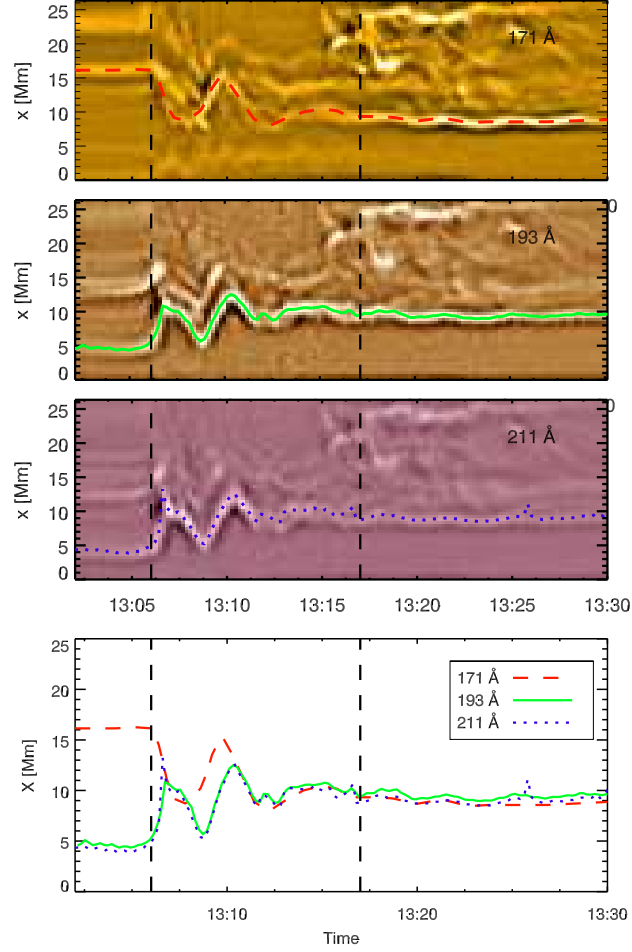
Figure 5.7: Example space-time images from a cut taken across the transversely oscillating loops is shown for the 171 Å, 193 Å, and 211 Å bandpasses. The images have been wavelet filtered using the Mexican hat wavelet. The anti-phase nature between the 171 Å loop and the loop observed in the 193 Å and 211 Å bandpasses is clearly visible and the displacement time series are indicated on the cuts. *Bottom*: The displacement time series are plotted on the same plot to highlight the anti-phase nature of the oscillations and to show how they compare spatially with one another. The reference times of 13:06 UT and 13:17 UT shown by the vertically dashed lines indicate the start of the initial high amplitude and later low amplitude oscillations respectively.

parameters as described in Chapter 3. The paths along which the cuts are taken to analyse the transverse oscillations are shown in the left panel of Figure 5.2. The angle of the paths are determined by a trial and error approach of identifying the clearest oscillations with the largest amplitudes. If an accurate estimate of the 3D loop geometry is found (not available in this case) then the cuts can be precisely aligned with the projected loop displacement. Where possible the displacement time series is determined automatically by fitting a Gaussian shape to the loop cross section at each time, however in most cases the displacement time series is determined by eye.

Figures 5.4, 5.5 and 5.6 show wavelet filtered space-time diagrams for each cut from the three AIA bandpasses, 171 Å, 193 Å and 211 Å, where transverse oscillations are detected. The displacement time series are indicated on each cut and the vertical dashed line at 13:06 UT indicates the reference time where the oscillations begin. A background polynomial of up to order four is subtracted from the displacement time series and a damped cosine profile is fitted using a Levenberg-Marquardt least squares method (Markwardt 2009) to determine the oscillation parameters. Similar to the method used in Foullon et al. (2010) and Gosain and Foullon (2012) to analyse quasi periodic pulsations in solar flares and transverse oscillations of prominences respectively, we find that the displacement time series are almost always best fitted by a profile that includes a linear change in the period with time e.g.

$$\xi(t) = \xi_0 \exp\left(\frac{-(t-t_0)}{\tau}\right) \cos\left(\frac{2\pi}{P + \alpha(t-t_0)}(t-t_0) - \phi\right), \qquad (5.1)$$

where ξ_0 is the displacement, τ is the damping time, P is the period, α is the rate of change in the period, ϕ is the phase and t_0 is the reference time. The errors on the oscillation parameters are taken as the standard deviation of the results from several cuts. Table 5.1 shows the oscillation parameters determined from the damped cosine profile fitting for each of the loops in the three bandpasses. The phases found by the profile fitting technique (and shown by the displacement profiles in Figure 5.7) show that the 171 Å loop ($\phi = $ -28 $\pm$ 3°) is initially oscillating in anti-phase with respect to the loops analysed in the 193 Å ($\phi = 135 \pm 14$°) and to a lesser extent the 211 Å ($\phi = 123 \pm 17$°) bandpasses. The 193 Å and 211 Å loop periods are comparable to one another whereas the period of the 171 Å loop is approximately 50 s longer. Figure 5.7 also shows that the 171 Å loop has a slightly longer period in this cut compared to the other loops however at a later time the displacement time profiles of each of the loops look to be in phase. The damping times show the characteristic short damping times expected for TLOs. Both the analysis and Figure 5.7 suggest

that the loops observed by the 193 Å and 211 Å bandpasses are part of the same multi-thermal loop structure rather than two distinct loops. The linear change in the period determined from the damped cosine fitting was positive for each of the loops analysed, suggesting that the period increases slightly during the oscillation. The example displacement time profiles from the three different wavelengths are compared in the bottom panel. This shows that the loops are perturbed at the same time with transverse oscillations that are initially directed inwards towards each other. Loop structures observed in the 193 Å and 211 Å bandpasses visible at x = 13 Mm begin to move inwards slightly before the hard X-ray flare peak (13:07 UT) and the excitation of the 171 Å loop highlighted by the dashed line. This early inwards motion may indicate that the loops are not instantaneously excited but that the excitation has a finite time width over which it ramps up, causing the loops to move inwards slightly earlier than the flare peak. At the end of the oscillations the loops which started at positions x = 5 Mm (193 Å, 211 Å) and x = 16 Mm (171 Å) have relaxed to the same position of x = 9 Mm.

Transverse oscillations are also excited at a later time in the same loops, beginning at approximately 13:17 UT (second vertical dashed line in Figure 5.7), but displaying smaller amplitudes. These oscillations are most likely a result of the plasma ejection from the flare site which flows along the field lines, perturbing them. Material ejected along field line trajectories to the south of the oscillating loops is visible in the top right part of the cuts. These lower amplitude oscillations are observed exclusively in the 171 Å and 193 Å bandpasses and show oscillations that are in phase with similar periods. Table 5.1 shows the results for these oscillations labelled 171b and 193b.

Any intensity oscillations present in the loops are investigated in the same way as for the displacement time series but taking the intensity located at each time series position. The intensity oscillations are also fitted with the damped cosine curve that includes a linear variation in the period. Results are shown in Table 5.1. Reliable intensity oscillations are observed for the 193 Å and 211 Å loops and the later, lower amplitude oscillation in the 193 Å bandpass. The intensity oscillations show approximately in phase behaviour with the displacement time series for the 193 Å and 211 Å bandpasses.

Table 5.1: Displacement oscillation parameters determined from the damped cosine fitting.

Loop	P (s)	τ (s)	ϕ $(°)$	α
Displacement				
171	224 ± 30	267 ± 70	-28 ± 5	0.179 ± 0.100
193	174 ± 10	271 ± 40	135 ± 10	0.071 ± 0.020
211	180 ± 10	285 ± 80	123 ± 20	0.059 ± 0.030
171b	196 ± 10	1295 ± 720	149 ± 20	0.008 ± 0.010
193b	194 ± 10	582 ± 190	149 ± 10	0.015 ± 0.100 [a]
Intensity				
193	171 ± 20	378 ± 160	143 ± 30	0.069 ± 0.040
211	151 ± 20	404 ± 240	152 ± 30	0.088 ± 0.030
193b	198 ± 10	834 ± 150	108 ± 30	0.006 ± 0.010

[a] Indicates the value is the result obtained for one cut only.
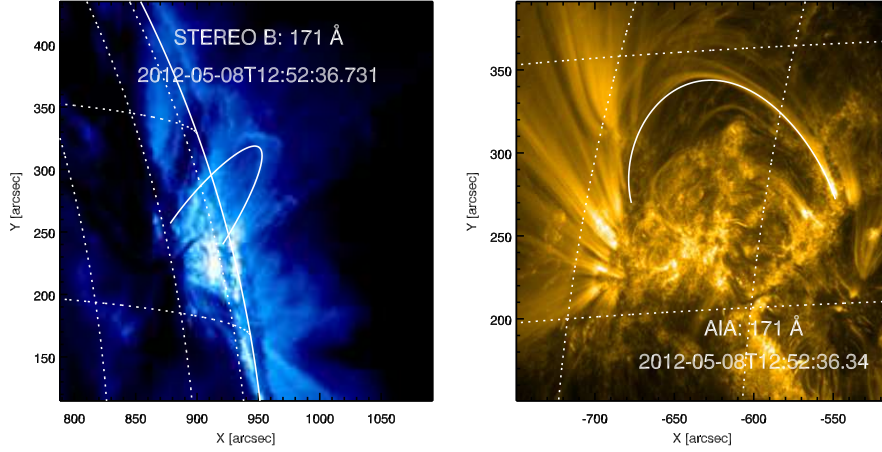
Figure 5.8: Figure showing the 3D geometry of the loops estimated from a comparison between STEREO and SDO viewpoints.

5.5 Active region topology

5.5.1 Loop 3D geometry

An estimate of the loop 3D geometry is found by comparing the loops in the AIA viewpoint with the loops observed on the limb by STEREO-B/EUVI in the 171 Å and 195 Å wavelengths. Figure 5.8 shows the comparison of the loop geometry between the SDO and the STEREO-B viewpoints. During this observation STEREO-B was approximately 118° behind the Earth viewpoint. See e.g. Section 3.4 and Verwichte et al. (2009, 2010) for details of the procedure for obtaining a 3D loop geometry. As a result of the reduced resolution compared with AIA and the fact that the loops are observed on the limb in EUVI, identifying and distinguishing loops from one another to get an accurate geometry is challenging. Using this method an approximate inclination angle of 43° north and a loop length of 195 Mm is found. This length is likely to be an underestimate of the true length of the loops since the best fit to the EUVI data was found by following the bright loop structure seen in all of the AIA bandpasses in Figure 5.1 which is below the loops studied (traced by the lines in Figure 5.2). There is a possibility that the anti-phase oscillations are a result of line of sight effects rather than a true anti-phase motion of loops. This possibility occurs if the loops are of opposite inclination with respect to the plane of sky. The comparison of the loop geometry shows that these loops located on the north east solar disk are highly inclined on the same side behind the plane of sky, suggesting that the anti-phase oscillations are not a result of line of sight effects.

5.5.2 Magnetic field topology: PFSS modelling

To probe the magnetic topology of the active region, magnetic field extrapolation is performed using the potential field source surface (PFSS) model (Schatten et al. 1969; Schrijver 2001; Schrijver and De Rosa 2003). The extrapolation technique incorporates line-of-sight magnetogram data from SDO/HMI near the central meridian and extrapolates the magnetic field out to a distance of 2.5 solar radii where it is then assumed radial. The most up to date magnetic map for a particular region of interest is obtained when the region has crossed the central meridian. In this observation the active region is located near N13° E44° on May 8 and has completely crossed the central meridian by May 13. Therefore in our analysis we use the coronal magnetic field model for data up to 2012 May 13, five days after the flare eruption. The left hand panel of Figure 5.9 shows the extrapolated field lines overlaid on an AIA 171 Å image. We are interested to see if there are any differences between
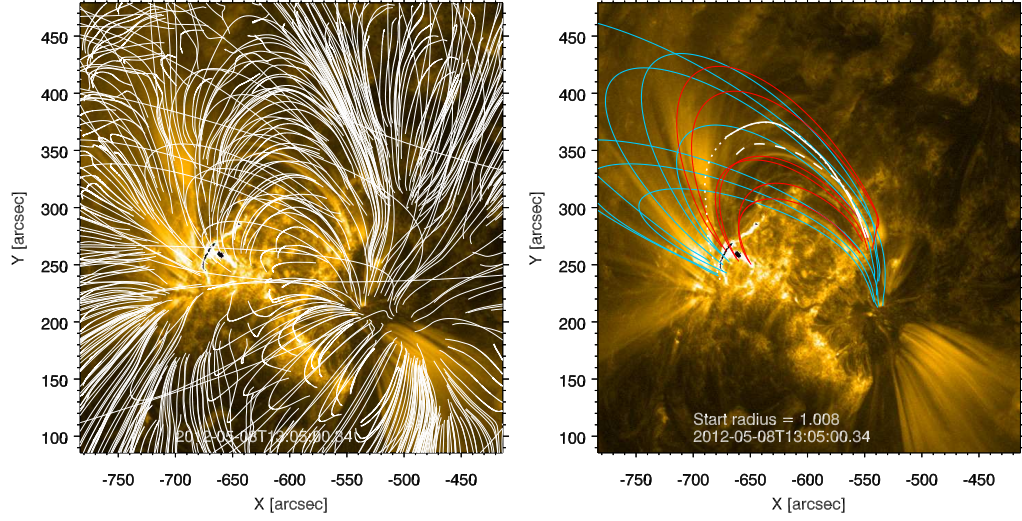
Figure 5.9: *Left*: plotted on a 171 Å SDO/AIA image are field lines calculated using the PFSS model with a starting radius of 1.008 solar radii. *Right*: Bundles of field lines that have different foot point positions are plotted to search for topological differences. The loop paths traced in the EUV images are overlaid in white as a comparison with the extrapolated field lines.

individual field lines such as the location of the foot points that may indicate different topological regions and give rise to the anti-phase oscillations. No particular topological differences between field lines are immediately apparent from overlaying the extrapolated field on the AIA image. To investigate this further, field lines with foot points that are anchored in different positions on the eastern and western sides are plotted in different colours. This is shown in the right hand panel of Figure 5.9. The loop paths of the AIA observed loops are also drawn on this plot. On the western side the red field lines are anchored in the negative flux region above the blue field lines which are anchored in the large negative sunspot. The observed 171 Å loop path shown by the dashed white line is seen to follow closely to a couple of the red field lines. On the east side of the active region the field lines are anchored at the same position as the flare ribbons. The blue field lines are located on the opposite side of the negative flux to some of the smaller red field lines. Both sets of eastern foot points must be located in regions of positive flux as their western foot points are anchored in negative flux regions. Figure 5.10 shows a negative polarity at X=-660″ Y=250″ that has disappeared by May 13.

The loop paths in the 193 Å and 211 Å channels (shown by the solid and dotted white lines) have larger radii of curvature and are therefore expected to have larger apex heights and foot point distances than the 171 Å loop. Since the active region

117
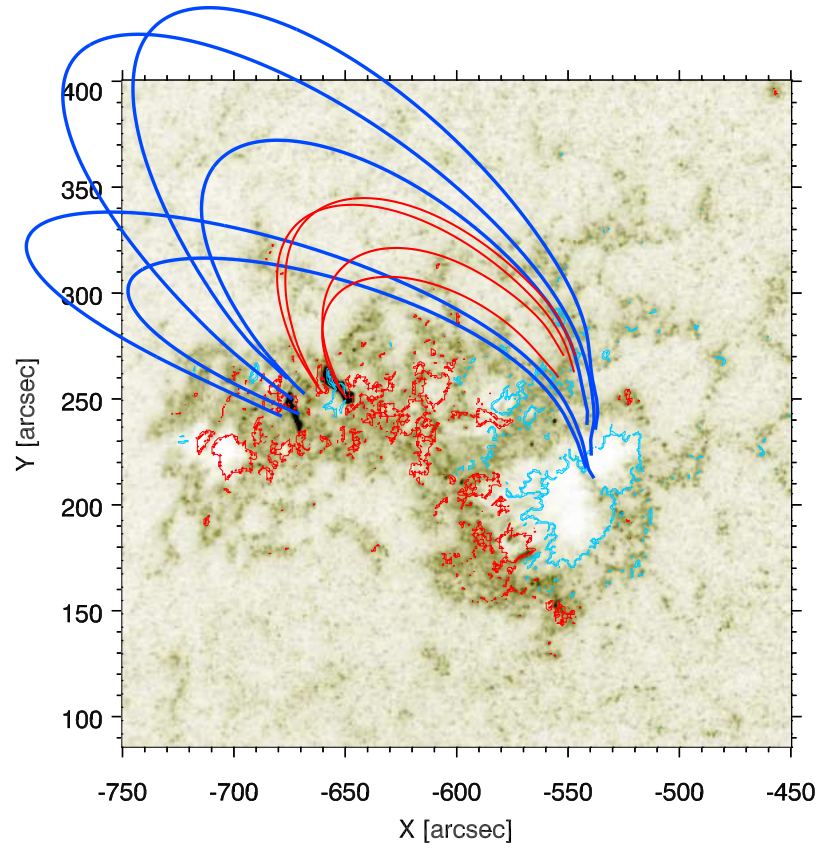
Figure 5.10: Field lines calculated using the PFSS model from 2012 May 13 are plotted on HMI line-of-sight magnetogram contours and an AIA 1600 Å reverse colour image showing the positions of the flare ribbons. The HMI contours and AIA image are from 13:05 UT on 2012 May 8. Magnetic field contours are plotted at -300 and 300 Gauss for the negative (blue contours) and positive (red contours) polarities respectively.

is evolving over the following days with the eruption of five M class and several C and B class flares, it is not surprising that their paths do not perfectly align with any of the PFSS field lines, which represent the expected topology five days later. Average misalignment angles of 20°- 40° have been reported for comparisons between observed loops and extrapolated potential field lines (Sandman et al. 2009). However, the comparison with the PFSS field lines and flare ribbon locations (see also Fig. 5.10) is helpful to confirm that the combined 193 Å and 211 Å loop path corresponds more closely to the topology of the higher and longer blue field lines, whereas the 171 Å loop corresponds to the topology of the lower and shorter red field lines.

As a further check to investigate if the anti-phase transverse oscillations are a result of line of sight effects, we perturb the groups of field lines shown in Figure 5.9 assuming a horizontally polarised fundamental kink mode, and create space-time diagrams using the cuts shown in Figure 5.2 that are used to analyse the observational loop oscillations. To model the oscillations we perturb the field lines following the method of Verwichte et al. (2009). Figure 5.11 shows the displacement time curves of field lines determined from a cut (location shown in panel (a)) assuming either a horizontally or vertically polarised fundamental kink mode. Panels (b) and (c) show the displacement time profiles we would expect if the red and blue bundles of field lines are oscillating in phase and panels (d) and (e) show the displacement time profiles we would expect if they are oscillating in anti-phase. This demonstrates that the observation of anti-phase transverse loop oscillations is not a result of line of sight effects and that the loops themselves must be oscillating in anti-phase.

5.6   Discussion

In this chapter we have presented an SDO/AIA observation of a loop observed in the 171 Å bandpass that oscillates with a transverse motion in anti-phase with respect to loops observed in the 193 Å and 211 Å bandpasses. This observation of transverse loop oscillations (TLOs) is unusual and counter intuitive when considering a flare blast wave excitation mechanism. A blast wave is often assumed to be the excitation mechanism for TLOs and should initially perturb the coronal loops away from the flare site.

The event occurs in the northern hemisphere and from the comparison between the AIA and STEREO fields of view, the loops are observed to be highly inclined in the same direction above the line of sight. This suggests that line of sight effects do not explain the anti-phase oscillations. Furthermore, the active region magnetic
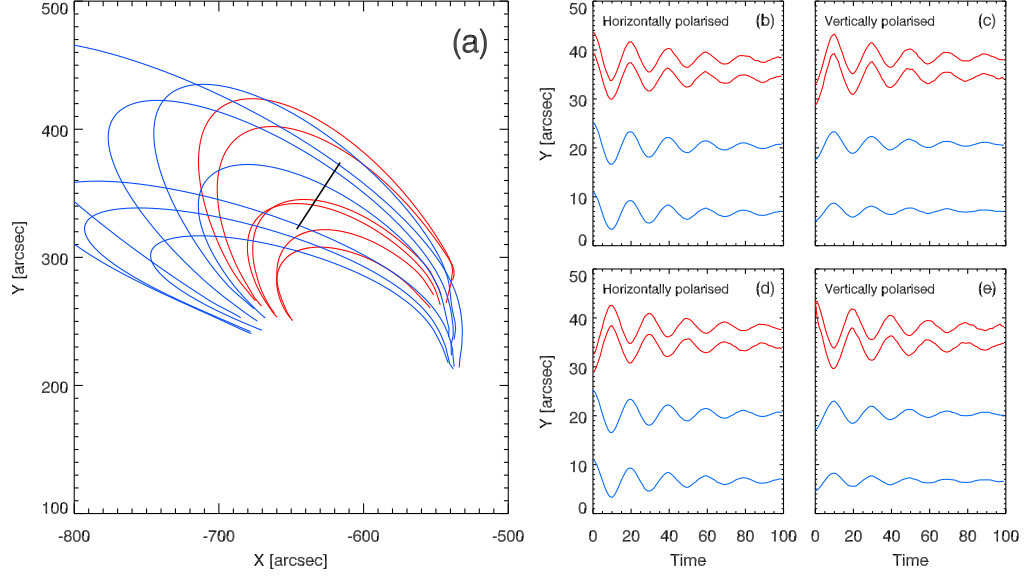
Figure 5.11: Figure demonstrating that the anti-phase transverse loop oscillations are not a result of line of sight effects but that field lines must be oscillating in anti-phase in order to produce an anti-phase signature. (a): The field lines obtained from the PFSS model. The red and blue groups of field lines are either perturbed so that they oscillate in phase or in anti-phase with each other. The black line indicates the cut taken to obtain space-time diagrams and is identical to the second from left cut in Figure 5.2. (b)-(e): Displacement time curves are shown for four field lines observed in the space-time diagrams for different polarisations of the kink mode and for the blue and red bundles of field lines oscillating either in phase or in anti-phase with one another. (b): Horizontally polarised kink mode, in phase perturbation. (c): Vertically polarised kink mode, in phase perturbation. (d): Horizontally polarised kink mode, anti-phase perturbation. (e): Vertically polarised kink mode, anti-phase perturbation.
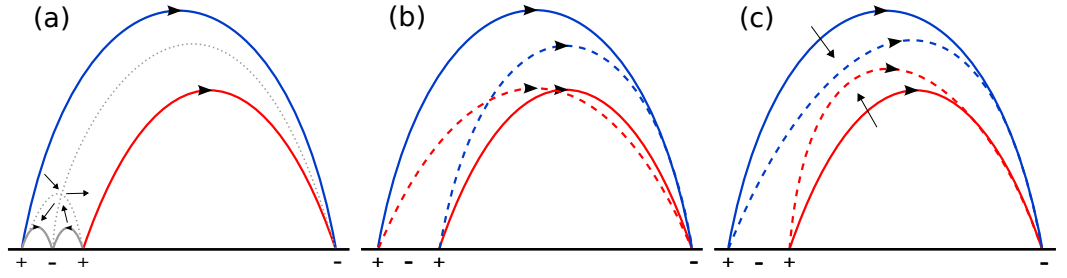
Figure 5.12: (a) Sketch showing the direction of the velocity field indicated by the arrows assuming a 2D reconnection process. (b) Example of how slipping field lines reconfigure from the initial plain field lines into the dashed field lines. (c) The arrows show the initial anti-phase direction of motion that adjacent loops might take if field lines are assumed to undergo slippage during the reconnection process.

field was investigated with the PFSS extrapolation technique and the resulting field lines were perturbed assuming that the TLOs were either horizontally or vertically polarised. The PFSS extrapolation method gives an adequate first approximation of the local magnetic topology of an active region, however a truer picture of the topology can be obtained using force free models (Seehafer 1978, 1982; Wiegelmann 2008) which require vector rather than line-of-sight magnetic field data. In this study the PFSS model is sufficient as a first investigation into how an observation of anti-phase TLOs links with the local magnetic topology but future studies should take this into account. From this analysis we rule out the possibility that the anti-phase oscillations are a result of an outside flare blast wave. Here the inwardly directed anti-phase nature of these oscillations suggests that the excitation is a local effect that is linked with the local magnetic topology of the region.

A previously reported example of anti-phase TLOs was presented by Schrijver et al. (2002). Here they linked the behaviour of the oscillations with the local magnetic topology of the region and the perturbation of null points. They suggest that a photospheric disturbance such as a sunquake may perturb the null points and so excite oscillations. In our observation however we do not see any signatures of photospheric disturbances. Anti-phase behaviour has also been observed in Doppler shift observations with SUMER (Kliem et al. 2002) between hot (10^7 K) and cooler (2×10^4 K) plasma. In the SUMER observation they rule out TLOs as the reason behind the anti-phase signatures because the oscillation amplitudes are large compared with the height of the observations. There are however some similarities of the SUMER observations with this work where oscillations in the cooler bandpass (171 Å) are in anti-phase with respect to the oscillations seen in the slightly hotter bandpasses (193 Å and 211 Å).

5.6.1 Reconnection driven wave dynamics

The impulsive nature and the inwardly directed anti-phase motion of the observed TLOs suggests that the excitation could be linked to the flare reconnection process. Longcope and Tarr (2012) studied reconnection at a current sheet by modelling a 2D quadrupolar field and analysing the energy conversion to fast magneto-acoustic waves. They study the dynamics of the external field and show that the velocity field above and below the current sheet is directed inwards (illustrated in their Figure 4). Our observations of anti-phase TLOs might then be explained as the signature of reconnection occurring in this active region. Figure 5.12a is a simplified model of the observed loops (solid lines) with the direction of the velocity field assuming a 2D reconnection model indicated by the arrows. In this case we would not expect anti-phase motion of the two loops because the velocity fields are directed in approximately the same direction. If this mechanism were to excite anti-phase oscillations then the loops must have their western (and eastern) foot points in opposite polarities to one another. A further limitation of this model is that it is in 2D and studies have shown that reconnection in 3D can be significantly different (Pontin 2011).

Panels b and c of Figure 5.12 illustrate the idea of slipping field lines. The slipping of field lines may occur either as a result of reconnection involving a 3D null point or slip-running reconnection. Figure 5.12b illustrates how field lines can change their connectivities through field line slippage. One of the foot points is held fixed (the negative polarity on the right hand side in this case) and the left hand foot points anchored in one positive polarity are allowed to slip over to the other positive source, so that the initial solid field lines end as the dashed field lines. In this observation we do not directly observe the slipping of field lines and we find that the oscillating loops end up at similar locations to where they started from. Figure 5.12c shows how field lines not directly involved in the reconnection process might then be perturbed by the slipping field lines. It provides an explanation of how inwardly directed transverse loop oscillations may be excited in this observation.

5.6.2 3D magnetic reconnection

3D reconnection at isolated null points has been split into three regimes: torsional spine, torsional fan, and spine-fan reconnection (Priest and Pontin 2009). Reconnection has also been proposed to occur in systems with multiple null points connected by separators, called separator reconnection (Pontin and Craig 2006), where current layers may form along the separator lines. In our observations it is possible that

a 3D null point has collapsed and that spine-fan reconnection is occurring. The slightly inward motions prior to the oscillation excitation (Section 5.4) and the low altitude release of energy may be further evidence that a null point has collapsed as field lines (and so loop structures) are initially drawn inwards towards the null point.

A two stage reconnection model with a fan-spine configuration was proposed by Török et al. (2009) motivated by Hinode/XRT observations of an event on the solar limb next to a quiet prominence cavity. During the first reconnection stage in their 3D numerical simulations, one can see field lines either side of the emerging flux show apparent motions towards the null point. Torsional Alfvén waves are also driven by the reconnection and are observed to propagate along the arcade field lines; the apparent inward motion of some of the field lines as a result of the torsional wave might again explain the inwardly directed anti-phase loop oscillations we observe. However, we need to be careful when comparing field line oscillations with oscillations of coronal structures since these Alfvén waves are perturbations of individual field lines whereas the transverse oscillations of density enhanced loops are interpreted as kink waves. Moreover, we note that the simulation by (Török et al. 2009) includes a prominence flux rope that is not present in our event. This introduces effects such as extra twist which may affect the perturbation of the field lines observed in the simulation.

3D non-null point reconnection models built on the concept of quasi-separatrix layers (QSLs) e.g. magnetic surfaces where there are strong gradients in the field line mapping (Démoulin et al. 1996) have been developed. QSLs are regions of enhanced current where magnetic reconnection is triggered if the current layers formed along QSLs are thin and dense enough (Démoulin et al. 1996). An example of a similar active region to the one we studied is shown in Démoulin et al. (1997), Figure 5d. Here the QSLs have been plotted along with typical field lines either side of the QSLs. Instead of the 2D picture of reconnection about an X point where field lines change topological connections, 3D field lines might instead undergo slip-running reconnection (Aulanier et al. 2006) where the field lines slip along one another and across the QSL boundary. If slip-running reconnection is the excitation mechanism behind the oscillations then we might expect the larger loop to shrink, the smaller loop to grow or a combination of the two. Figure 5.7 shows that the loops are initially about 10 Mm from one another in the cuts but at the end of the impulsive oscillations they are located at the same line-of-sight position at the location of the cut. This suggests that the loops have been pulled together and perhaps even merged during the observation. This is further evidence in support of a slip-running

reconnection excitation mechanism. X-ray coronal loop slippage triggered by a flare has been observed by Hinode/XRT (Aulanier et al. 2007). That observation shows the loop foot points slipping over a duration length of about 3.5 hours. Sometimes the loops show apparent motions in opposite directions, interpreted as a signature of the slip-running reconnection. Slip-running reconnection of field lines has also been observed to occur numerically before and after 3D null point reconnection in a region where a 3D null point is embedded within a QSL (Masson et al. 2009). Our observation of anti-phase loop oscillations may be a signature of field lines undergoing slip-running reconnection happening close to the EUV flare emission or in the vicinity of a 3D null point.

5.6.3 Differing periods between loops

Another unusual feature of our observation is that the smaller 171 Å loop oscillates with an average period that is approximately 50 s longer than the loops observed in the 193 Å and 211 Å bandpasses. Although this slightly longer period is within 2σ of the 193 Å and 211 Å loop periods, it is seen in the cuts in Figures 5.4 and 5.7. Table 5.1 shows that the linear change in period for the 171 Å loop is 0.179 compared with 0.071 and 0.059 for the 193 Å and 211 Å loops respectively. Increases in periods may be associated with growing loop lengths. Assuming that the transverse oscillations are fundamental kink modes, the phase speed, $V_{ph} = 2L/P$ is lower for the smaller 171 Å loop compared to the larger 193 Å and 211 Å loops. A lower value of the phase speed indicates a lower value for the average magnetic field strength of the loop. From the PFSS model the blue field lines are anchored in the sunspot region on the western side where as the red field lines are anchored just above this region. We then expect the blue field lines to have a larger average magnetic field strength compared to the red field lines. This would cause the oscillation period of the red field lines to be slightly longer. Since the red field lines are an approximate match for the 171 Å loop and the 193 Å and 211 Å loops align better with the blue field lines this could give an explanation for the slightly longer period observed for the 171 Å loop.

An example blue PFSS field line has an average magnetic field strength of approximately 23 G compared to approximately 42 G for an example red PFSS field line. This suggests that the 171 Å loop should have a shorter period compared to the 193 Å and 211 Å loops which is not what we observe. However we also note that the PFSS field lines are not a precise match for the projected loop coordinates and in particular that the western footpoint locations of the blue field lines do not match well with the estimated footpoint locations of the loops from the observations.

Chapter 6

Anti-phase oscillations of loops in the vicinity of a 2D X-point

6.1 Chapter overview

In this chapter we present a numerical study of transverse oscillations of coronal loops that are situated above and below a magnetic X-point. This study is motivated by the SDO/AIA observation, presented in Chapter 5, of unusual anti-phase oscillatory behaviour between coronal loops located in different topological regions.

6.2 Introduction

Magnetic reconnection, the process where magnetic field lines undergo topological changes and release energy, is important in the solar corona especially in the context of coronal heating and solar flares (Priest and Forbes 2002). In 2D, magnetic X-points are preferential places for reconnection to occur. Often X-points have been considered separately from MHD waves, however a number of studies have sought to change this.

Studies of magnetic X-points involving their interaction with magnetoacoustic waves and the oscillatory motion of the current layers has been conducted by several authors. Craig and McClymont (1991) studied a perturbed X-point in cylindrical coordinates where the field lines are anchored to the circular boundary and the system is closed so that no magnetic flux can enter or leave the domain. They presented analytical solutions describing the relaxation of the X-point, which were found by matching the large scale advection of the global field to the localised diffusion region at the boundary, given by $r \approx \eta^{1/2}$, where η is the resistivity. Craig

and McClymont (1991) concentrate only on the purely radial modes ($m = 0$) that have no nodes ($n = 0$) since these are the only modes that correspond to topological reconnection. The analysis results in equations describing the period, P, and damping time, τ, of the oscillatory relaxation of the X-point which is dependant on the Lundquist number, S such that,

$$\frac{P}{\tau_A} = 2\ln S, \tag{6.1a}$$

$$\frac{\tau}{\tau_A} = \frac{2}{\pi^2} \left(\ln S\right)^2, \tag{6.1b}$$

where τ_A is the Alfvén travel time and the Lundquist number is defined as:

$$S = \frac{LV_A}{\eta}. \tag{6.2}$$

Motivated by the work of Craig and McClymont (1991), McLaughlin and Hood (2004) conducted a numerical study of a fast magnetoacoustic wave propagating in the vicinity of a 2D magnetic X-point. Here they studied the propagation of a wave pulse originating from the top boundary using ideal MHD in a cold ($\beta = 0$) plasma. Resistive terms in the MHD equations were not considered and therefore no dissipation occurred in the system. They demonstrated that the linear fast magnetoacoustic wave launched from the simulation boundary undergoes refraction due to the spatially varying Alfvén speed, so that it curls around the null point. They show that the wave energy accumulates at the null point leading to an accumulation of current at the centre that builds up exponentially in time. An extension of this work considering a finite plasma-β was conducted by McLaughlin and Hood (2006). A consequence of including a finite value of β is that the sound speed will be non-zero at the null point and therefore the fast speed will also be non-zero at this point. Again they launch a magnetoacoustic pulse at the boundary which is also refracted around the null point. In contrast to the previous work they observe both fast and slow wave behaviour once the wave passes through the boundary where $\beta = 1$ and the sound speed is equal to the Alfvén speed. A consequence of the finite sound speed at the X-point is that some of the wave energy is allowed to pass through it. They conclude that there will still be a large accumulation of current at the null even in the finite β case, so that X-points are regions of preferential heating. Extending the work of Craig and McClymont (1991); McLaughlin and Hood (2004, 2006), McLaughlin et al. (2009) considered both a finite plasma-β and nonlinear effects. They model a 2D X-point, perturbed by a large amplitude circular

pulse that is the $m = 0$ mode in the perpendicular velocity. This corresponds to the $m = 2$ mode in Cartesian coordinates. They observe oscillatory reconnection behaviour of the current sheet so that an initially vertical current sheet becomes a horizontal sheet due to overshoot of the plasma carrying a greater amount of flux through the X-point than is required for a static equilibrium (Craig and McClymont 1991). Effects of a non-linear wave pulse on a 2D X-point was also considered by Gruszecki et al. (2011). The interaction between a circular fast wave perturbation on a magnetic X-point that includes the addition of the Hall term to the resistive MHD equations has been considered by Threlfall et al. (2012). Their numerical simulations displayed similar oscillatory relaxation behaviour of the current density as, e.g. McLaughlin et al. (2009), and the inclusion of the Hall term can lead to an accelerated rate of reconnection.

In the following study we extend the previous work by modelling a 2D X-point with density enhanced loops located in the upper and lower quadrants. A circular $m = 0$ pulse is launched, similar to that described in McLaughlin et al. (2009). We investigate if anti-phase transverse oscillations in loops situated in different topological regions can be excited from a perturbation at the X-point. We also study the effects of the plasma resistivity, the pressure, the amplitude of the velocity pulse and the initial position of the velocity pulse on both the loop oscillations and the oscillatory relaxation of the X-point.

6.3 Numerical model

Numerical simulations are performed using the Lare2D code (Arber et al. 2001) which solves the resistive MHD equations on a staggered grid to second order accuracy in space and time. We set up a magnetic X-point with a density enhanced loop above and below the centre. The X-point configuration has a magnetic field strength defined as,

$$\mathbf{B} = \frac{B_0}{L}(y, x), \tag{6.3}$$

where $B_0 = 1$ and $L = 30$. L is the characteristic length scale for magnetic field variations. The loops are given an Epstein density profile,

$$\rho = \rho_e + (\rho_0 - \rho_e)\operatorname{sech}^2\left(\frac{r - (r_1 + r_0/2)}{0.25r_0}\right), \tag{6.4}$$

where $r = \sqrt{x^2 + y^2}$, $r_1 = 19\,\mathrm{Mm}$, $r_0 = 2\,\mathrm{Mm}$, the external density ρ_e is 0.01 and the internal density ρ_0 is 0.1, giving a loop density contrast of 10. The normalisation
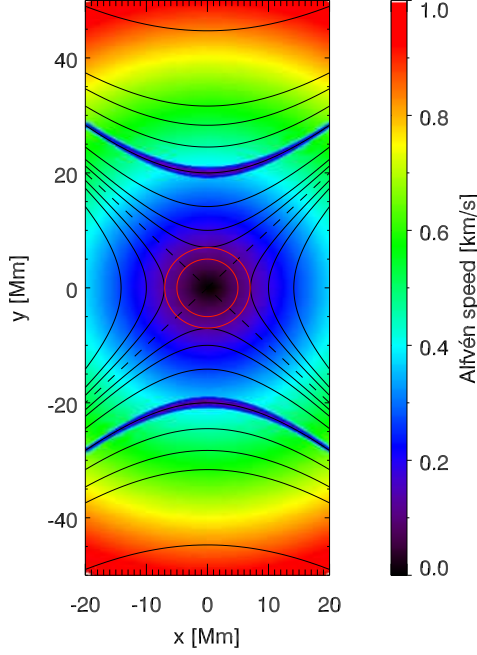
Figure 6.1: The equilibrium configuration showing the magnetic field contours on top of the Alfvén velocity. The dotted lines crossing through the centre of the X-point are the separatrix lines. The dense loops in the upper and lower quadrants are seen as regions of low Alfvén speed compared with the background. The position and width of the initial circular pulse is shown by the red contours.

parameters are given the following values: $B_0 = 0.0001$ T (1 G), $L_0 = 1$ Mm, $\rho_0 = 5 \times 10^{-13}$ kg m^{-3}. The number of gridpoints in the x and y direction are 128 and 512 respectively. x has a range of $[-20, 20]$ Mm and y has a range of $[-50, 50]$ Mm. All boundaries are held fixed so that the loops are line tied. Open boundary conditions are not used in the y direction because they introduce large velocity components of v_x and v_y at the boundary. The equilibrium configuration is shown in figure 6.1. Contours of the magnetic field strength are plotted on a map of the Alfvén velocity which highlights the positions of the loops above and below the X-point. The initial profiles of the plasma-β, temperature, sound speed and Alfvén speed in the y direction through the centre of the X-point are shown in figure 6.2. The plasma-β has a value much greater than 1 in the vicinity of the X-point and is much less than 1 in the regions occupied by the dense loops. The background sound speed and temperature are comparable to coronal values and the Alfvén speed in the loops is greater than the sound speed and also comparable to coronal conditions. The dimensionless pressure, p, has a value of 0.01 except where
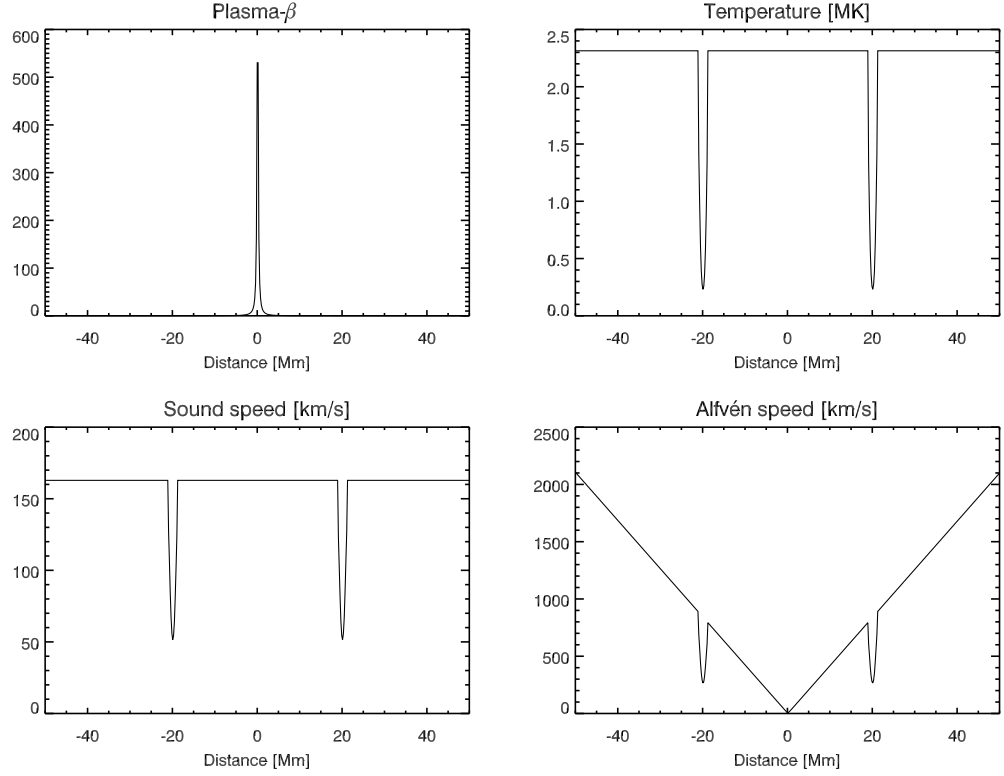
Figure 6.2: Initial profiles of (from top left to bottom right) the plasma-β, temperature, sound speed and Alfvén speed in the y direction through the centre of the X-point.

the effect of the variation of the pressure is considered.

6.3.1 Fast magnetoacoustic velocity perturbation

To excite the transverse oscillations of the loops and to investigate if we can set up anti-phase oscillations we launch a circular velocity pulse perpendicular to the magnetic field. In Cartesian coordinates and following e.g. McLaughlin et al. (2009), we define the variables $v_\perp$ and $v_\parallel$ as,

$$
\begin{aligned}
v_\perp &= (\mathbf{v} \times \mathbf{B}) \cdot \hat{z} = v_x B_y - v_y B_x, \\
v_\parallel &= \mathbf{v} \cdot \mathbf{B} = v_x B_x + v_y B_y.
\end{aligned}
\tag{6.5}
$$

Rearranging Eq. (6.5) to get v_x and v_y in terms of $v_\perp$ and $v_\parallel$ leads to,
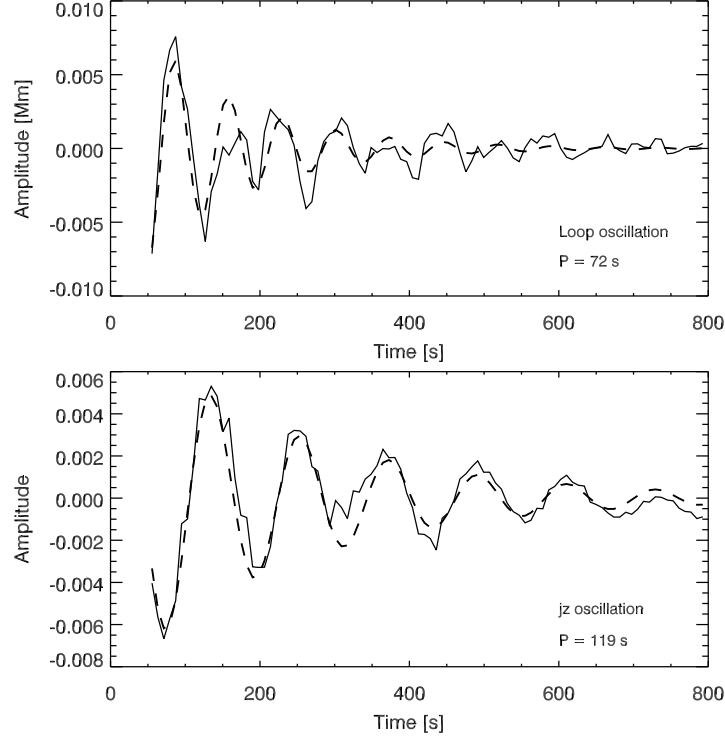
Figure 6.3: *Upper*: Time displacement of the density of the top loop fitted with a damped cosine curve. *Lower*: j_z oscillation at the centre of the X-point at position $(0, 0)$. The velocity pulse has an amplitude $A = 0.01$.

$$v_x = \frac{v_\parallel B_x + v_\perp B_y}{|B^2|},$$
$$v_y = \frac{v_\parallel B_y + v_\perp B_x}{|B^2|}. \tag{6.6}$$

For an $m = 2$ pulse ($m = 0$ in cylindrical geometry) that is perpendicular to the magnetic field, $v_\parallel = 0$ and $v_\perp = A \sin\left(\pi \frac{r - r_1}{r_0}\right)$ so that,

$$v_x = A \sin\left(\pi \frac{r - r_1}{r_0}\right) \frac{B_y}{B_x^2 + B_y^2},$$
$$v_y = -A \sin\left(\pi \frac{r - r_1}{r_0}\right) \frac{B_x}{B_x^2 + B_y^2}, \tag{6.7}$$

where $r_1 < r < r_1 + r_0$, $r = \sqrt{x^2 + y^2}$, $A = 0.01$, $r_1 = 4.5$ Mm and $r_0 = 3$ Mm.
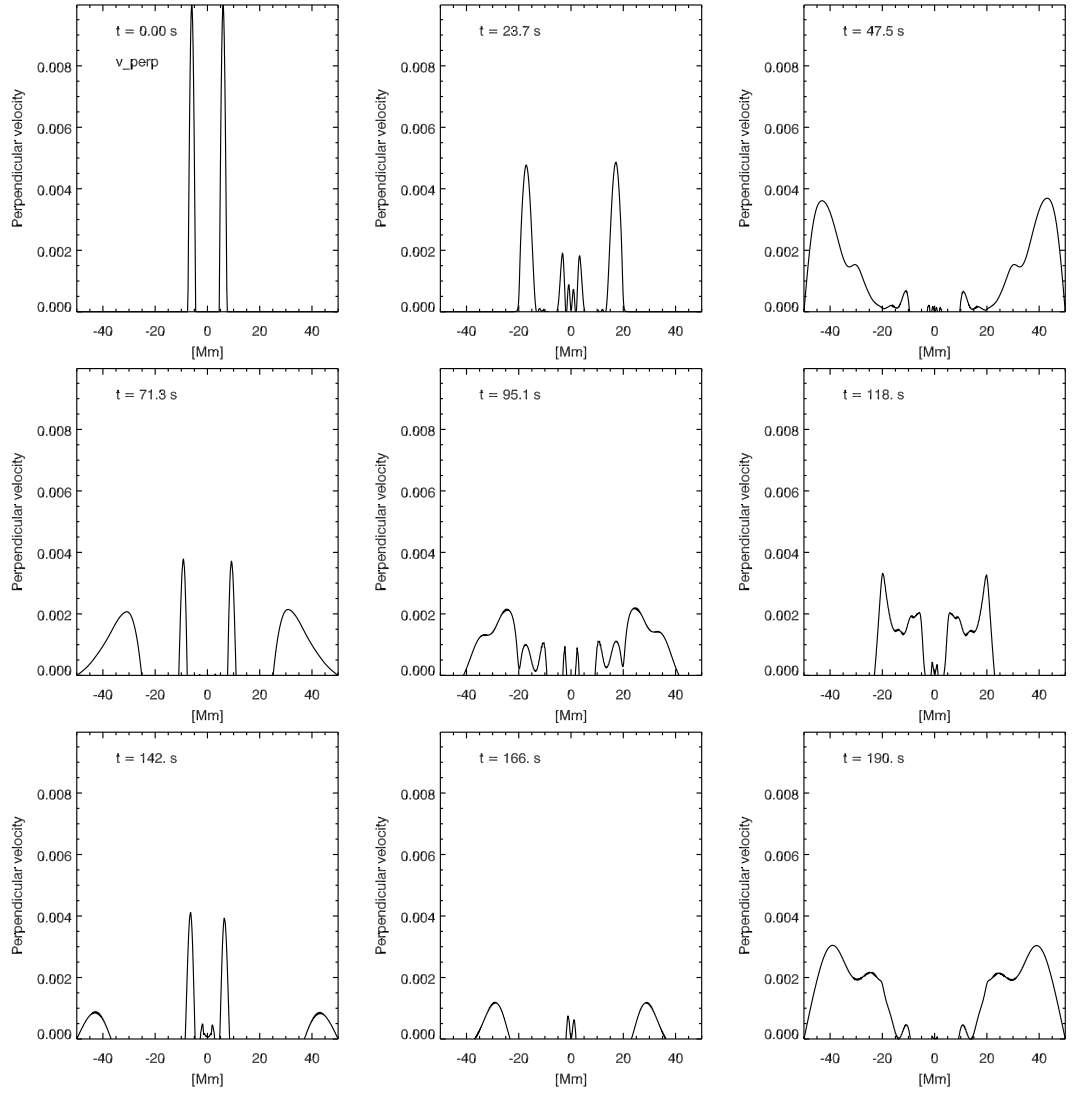
Figure 6.4: Perpendicular velocity in the y direction.
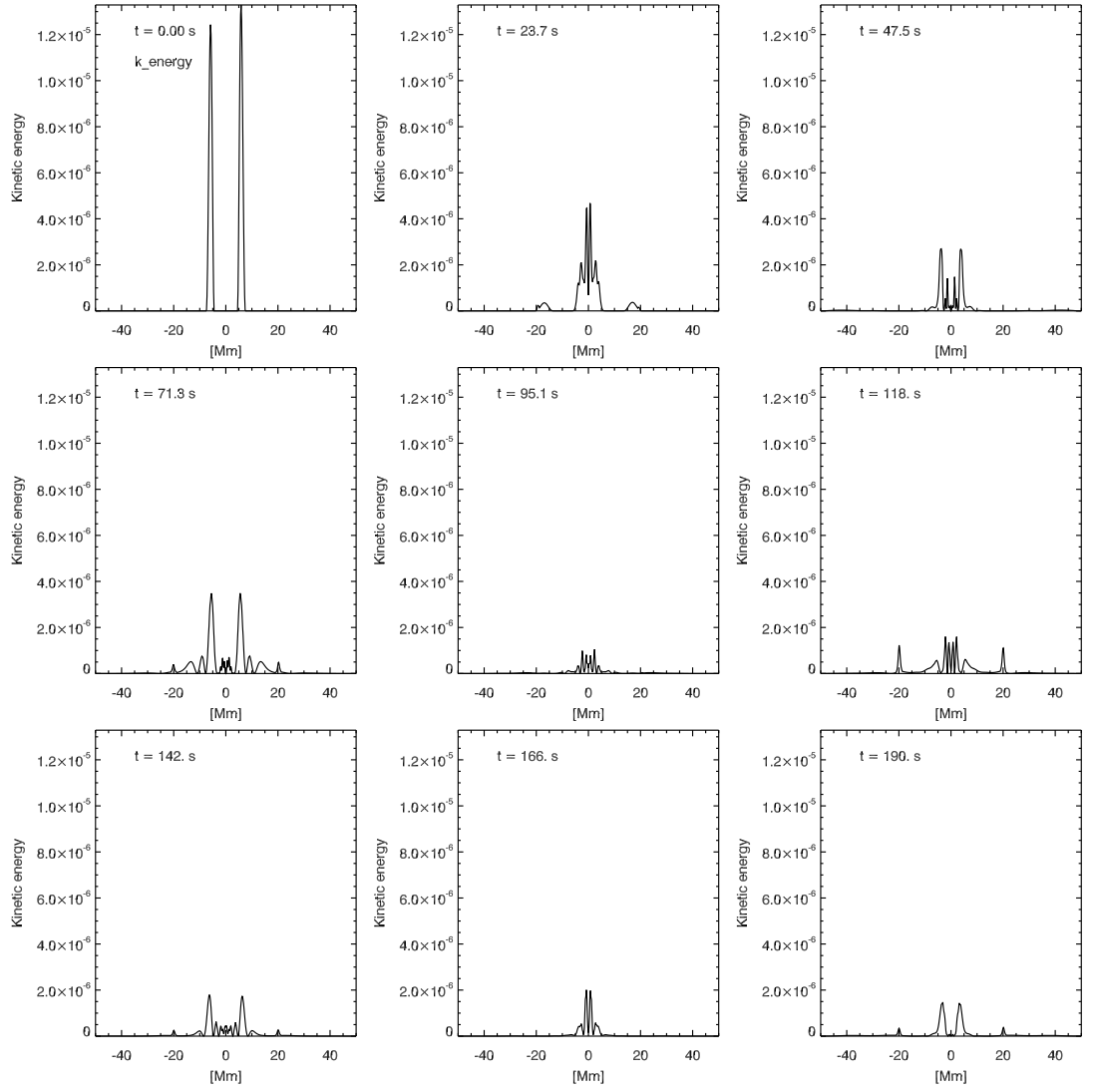
Figure 6.5: Kinetic energy in the y direction.

6.4 Results

Figure 6.3 shows the displacement time series of the top loop and the oscillation time series of the current in the ignorable direction (j_z) following an $m = 2$ pulse. Similar to McLaughlin et al. (2009) the initial pulse splits into separate inward and outward travelling pulses. In our experiment it is the outwardly directed pulse that initially excites the loops and the inwardly directed pulse that excites the X-point. The loops are initially perturbed inwards towards the X-point so that they oscillate in anti-phase to one another. We observe the contraction of the inwardly directed pulse and its refraction due to the spatially varying Alfvén speed. y is varied between $[-50, 50]$ Mm and $[-210, 210]$ Mm to ensure that the results do not vary because of the fixed boundary condition. The displacement-time variation of the loop is found by taking a cut in the vertical direction at $x = 0$, so that the cut passes directly through the loop apex, and subtracting a linear trend. The amplitude-time variation of the X-point is given by j_z at the centre of the X-point at the $x - y$ position of $(0, 0)$, and a linear trend is also subtracted. The trend subtracted variations are fitted with a damped cosine curve using a Levenberg-Marquardt least squares fitting technique (Markwardt 2009). The periodicity of j_z at 119 s is 1.7 times the loop oscillation period of 72 s. Figures 6.4 and 6.5 show the variation in the perpendicular velocity and kinetic energy in the vertical (y) direction in time that cover the first and first two peaks of oscillation for the oscillation in j_z and the loop oscillation respectively. The variation in the perpendicular velocity shows that the velocity reflects at the y boundary, however by varying the size of the domain in the y direction we found that the reflections do not affect the periodicity of either the loop or the X-point. Figure 6.6 shows 2D snapshots of the kinetic energy of the simulation region and shows that the majority of the kinetic energy is focused at the X-point and along the separatrices.

6.4.1 Varying the background resistivity

Craig and McClymont (1991) investigated numerically and semi analytically reconnection at an X-point in cylindrical geometry and showed that the oscillation and decay timescales depend on the plasma resistivity, η. Eqs. (6.1) show the dependency of the timescales on η, and in Lare2D $\eta = 1/S$ where S is the Lundquist number.

To investigate the effect of resistivity on the X-point oscillation and the loop oscillations, we vary the background resistivity between 0.00001 and 0.01. S therefore varies between 10^5 and 10^2 which is less than coronal values which are expected to
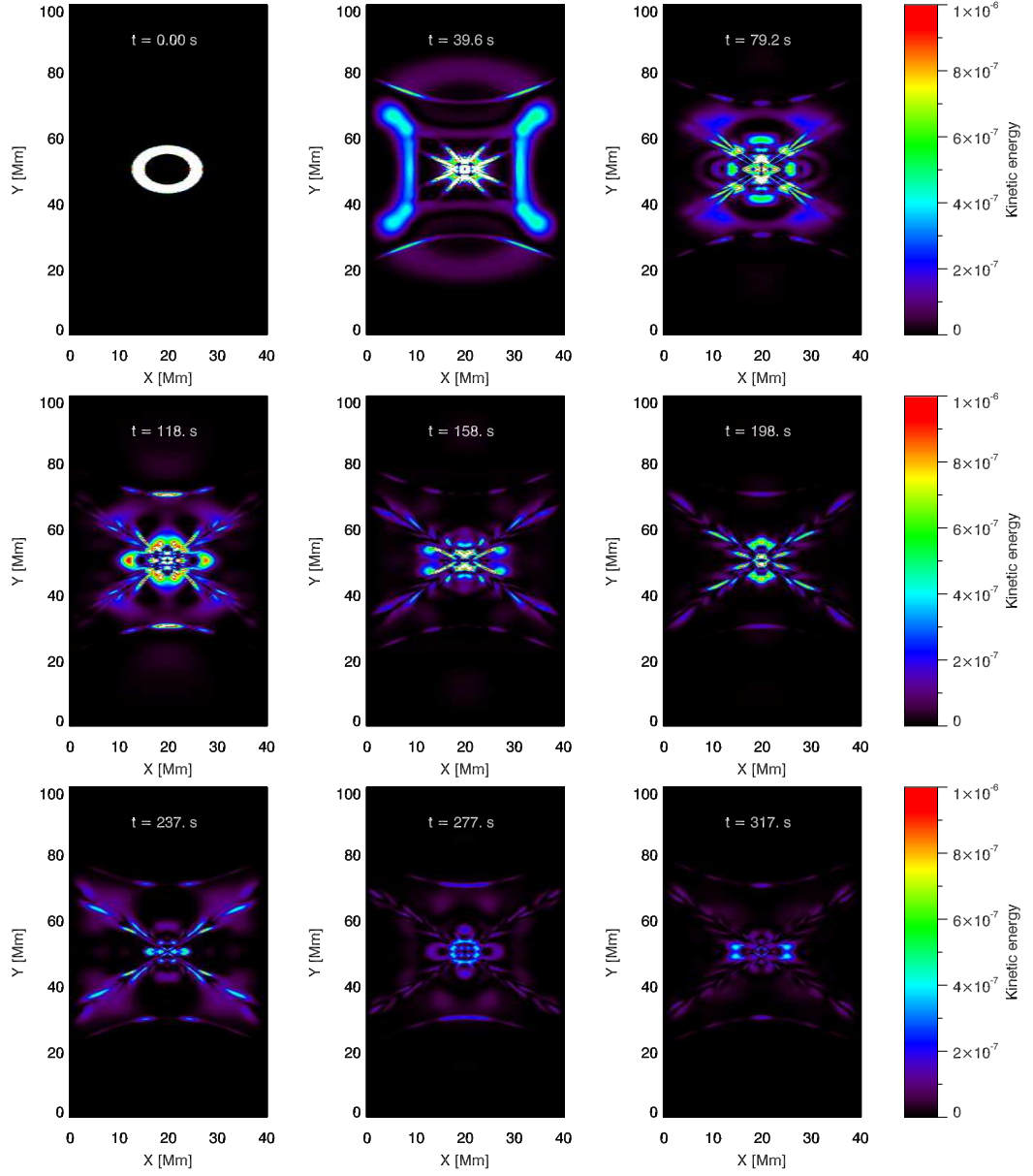
Figure 6.6: Evolution of the kinetic energy.
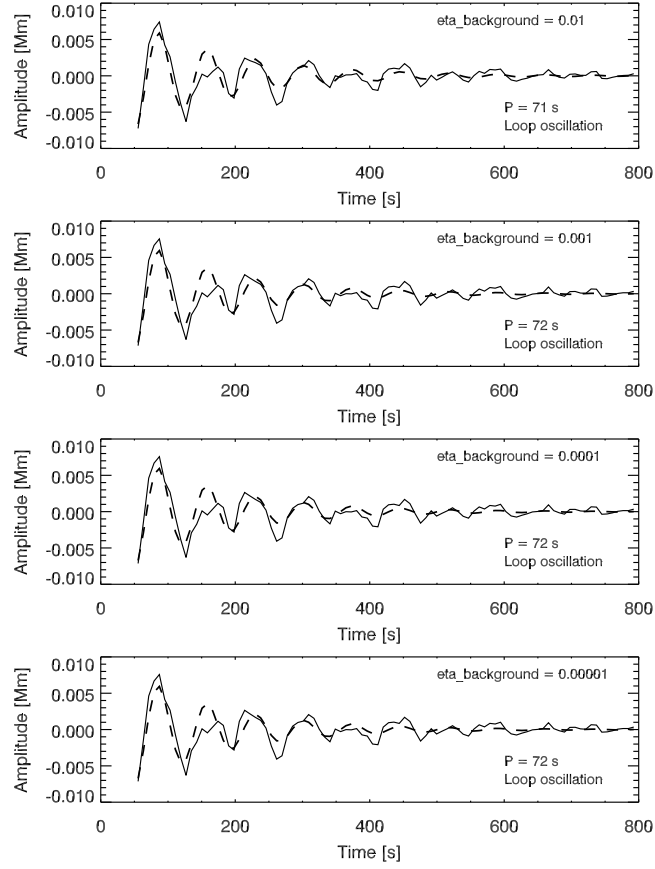
Figure 6.7: Displacement of the top loop as a function of time for different values of the resistivity.

be in the range $10^8 - 10^{12}$. Figures 6.7 and 6.8 show that varying the resistivity over a large range has no effect on the periodicity of either the loop displacement or current density oscillation. This result contradicts the analytical predictions, however there are some key differences between our simulations and the analytical and simulated model of (Craig and McClymont 1991). In our model we do not have a circular boundary and the fast magnetoacoustic wave pulse that is implemented in our simulations leads to many radial eigenmodes that have a range of frequencies (Threlfall et al. 2012).

6.4.2 Varying the pressure

Figure 6.9 and figure 6.10 show the displacement time series for the top loop and the time series of j_z respectively when the pressure, p, given in dimensionless units is
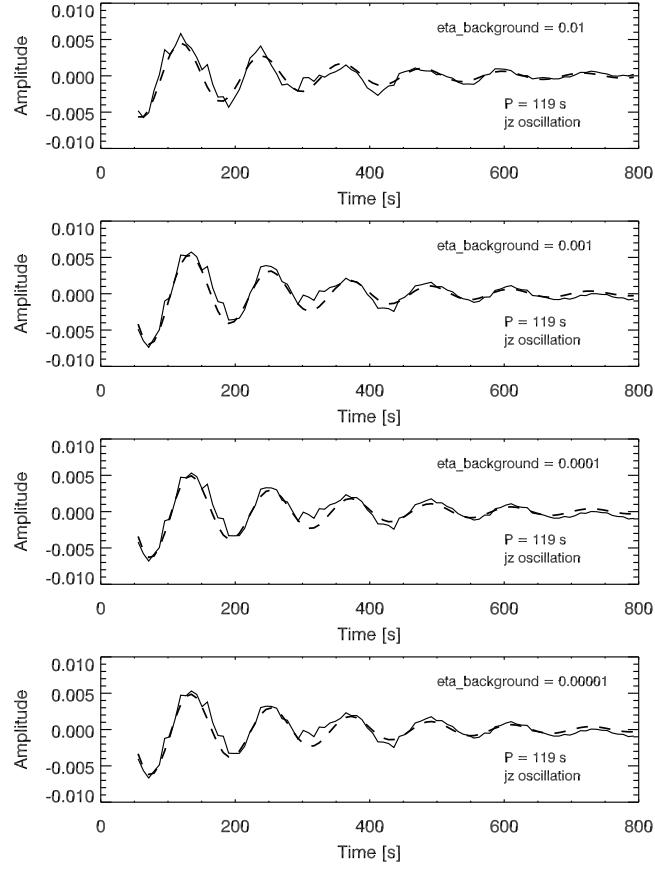
Figure 6.8: j_z component of the current density as a function of time for different values of the resistivity.

varied between 0.5 and 0.0005. As the pressure is increased, the loop displacement period first increases from about 70 s to 100 s and then decreases to 63 s when p = 0.5. The amplitude also decreases as the pressure increases. When $p = 0.05$, the sound speed is comparable to the Alfvén speed in the loops and when $p = 0.5$ the sound speed is much greater than the Alfvén speed near the loops and the X-point. These two cases do not represent coronal conditions and, in addition, the initial background temperature when $p = 0.5$ is on the order of 100 MK which far exceeds background coronal temperatures.

6.4.3 Varying the velocity amplitude A

We investigate the effect of varying the amplitude of the fast magnetoacoustic velocity perturbation on the oscillatory behaviour of the loops and the X-point. Figures
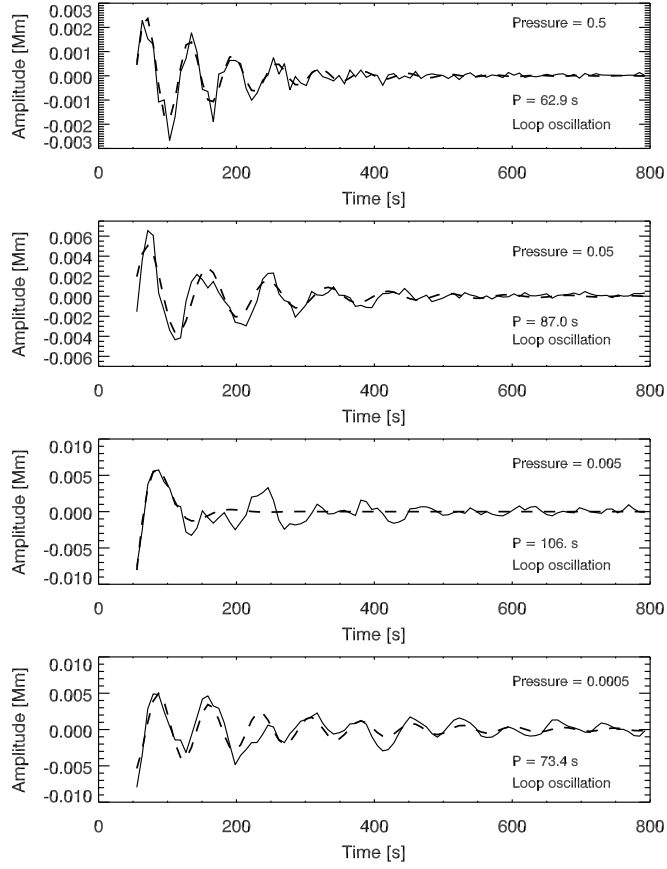
Figure 6.9: Displacement of the top loop as a function of time for different values of the pressure.

6.11 and 6.12 show the results of varying A between 0.001 and 1. Figure 6.11 shows that the amplitude of the loop oscillations increases linearly with the velocity amplitude except for the case when $A = 1$ where the problem starts to become nonlinear. This trend is also observed in the oscillatory behaviour of j_z at the X-point. In our simulations the normalised velocity $v_0 \approx 126$ km s^{-1} so that a velocity amplitude of 0.01 is equivalent to 1.26 km s^{-1}. For $p = 0.01$, the background sound speed is approximately 165 km s^{-1} and approximately 50 km s^{-1} in the loops (see figure 6.2). Therefore the velocity amplitude is between 0.1% and 3% of the sound speed and the problem is assumed linear for $A = 0.01$.
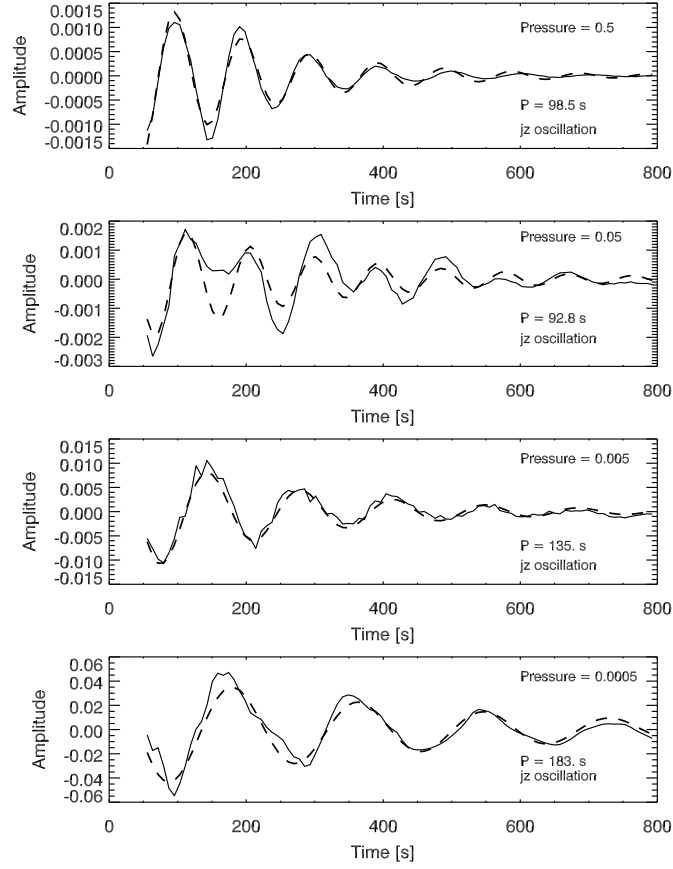
Figure 6.10: j_z component of the current density as a function of time for different values of the pressure.

6.4.4 Varying the initial position of the velocity perturbation

We vary the initial position of the velocity perturbation by varying r_1 in Eq. (6.7) between 3 Mm and 10 Mm from the X-point. Figures 6.13 and 6.14 show the displacement oscillation of the top loop and the oscillation of the current density at the X-point respectively. Figure 6.13 shows that the closer the velocity pulse is to the X-point, the clearer the displacement oscillation of the loop and the larger the oscillation amplitude. The figure shows variation in the loop oscillation period however the damped cosine fit is only reliable for the case where $r_1 = 3$ Mm. Figure 6.14 shows the oscillation of the current density at the centre of the X-point and shows that both the amplitude and the period of the oscillation increases slightly as the perturbation is moved towards the X-point. For each value of r_1, j_z displays oscillations that are reliably fitted with a damped cosine curve.
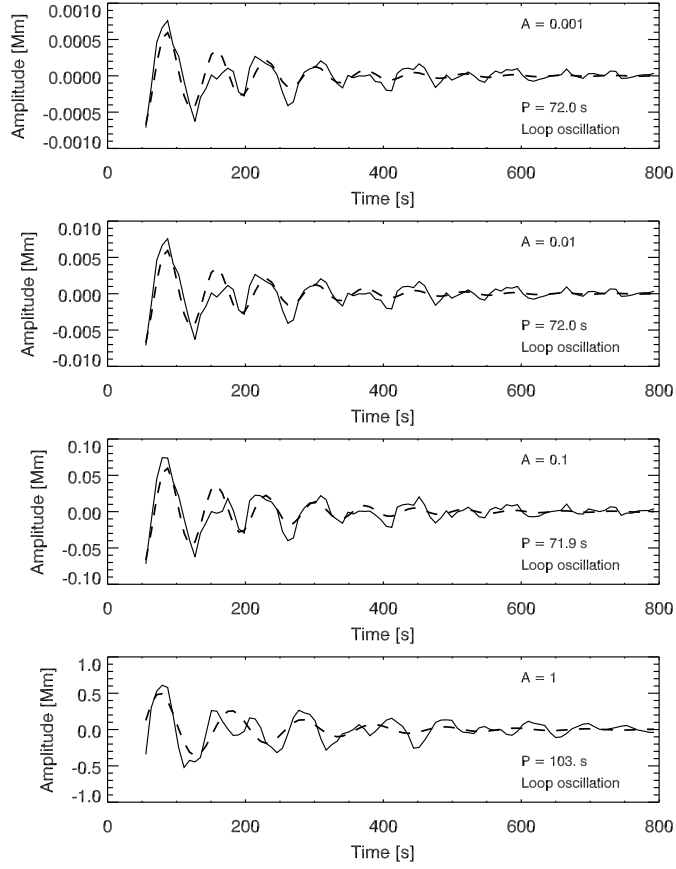
Figure 6.11: Displacement of the top loop as a function of time for different values of the velocity amplitude.

6.5 Analytic solution

Craig and McClymont (1991) studied a perturbed X-point and found analytic solutions after matching the large scale advection of the global field to the localised diffusion region. A wave equation can be written in terms of the vector potential ψ where $\mathbf{B} = \nabla \times \psi \mathbf{z}$,

$$\left[\frac{\partial^2}{\partial t^2} - (C_S^2 + V_A^2(r))\vec{\nabla}^2 \right] \psi = 0 \ . \tag{6.8}$$

where the resistivity η has been neglected and we assume a low plasma-β. We solve this analytically and match solutions at the boundary where the sound speed is equal to the Alfvén speed in order to find the frequencies of the modes, and to compare the periods with those of the loop displacement and j_z at the X-point centre from

139
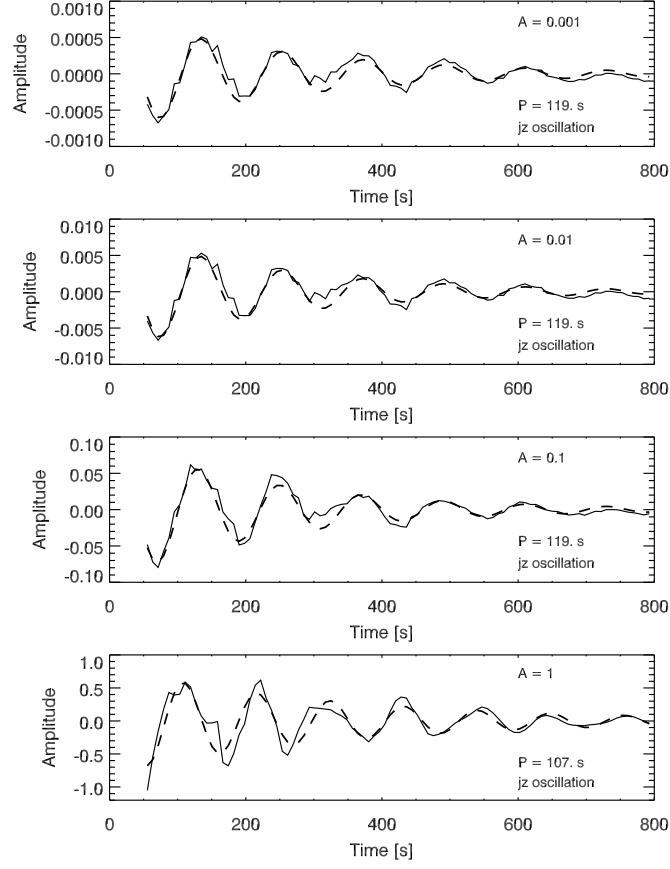
Figure 6.12: j_z component of the current density as a function of time for different values of the velocity amplitude.

the simulations.

For a normal mode with frequency ω and azimuthal wavenumber m, we find,

$$\frac{\partial^2 \psi}{\partial r^2} + \frac{1}{r}\frac{\partial \psi}{\partial r} + \left[\frac{\omega^2}{C_S^2 + V_A^2(r)} - \frac{m^2}{r^2}\right]\psi = 0 \ . \tag{6.9}$$

Taking $V_A = V_{A0}r/R$, Eq. 6.9 becomes,

$$\frac{\partial^2 \psi}{\partial r^2} + \frac{1}{r}\frac{\partial \psi}{\partial r} + \left[\frac{\omega^2}{C_S^2 + V_{A0}^2(r/R)^2} - \frac{m^2}{r^2}\right]\psi = 0 \ . \tag{6.10}$$

Now we consider the radius where $C_S = V_A$ i.e. where $\beta = 1$. Here $r^* = RC_S/V_{A0}$ and an outer boundary at $r=a$ is imposed. For $r \ll r^*$, the sound speed dominates and the equation becomes approximately,
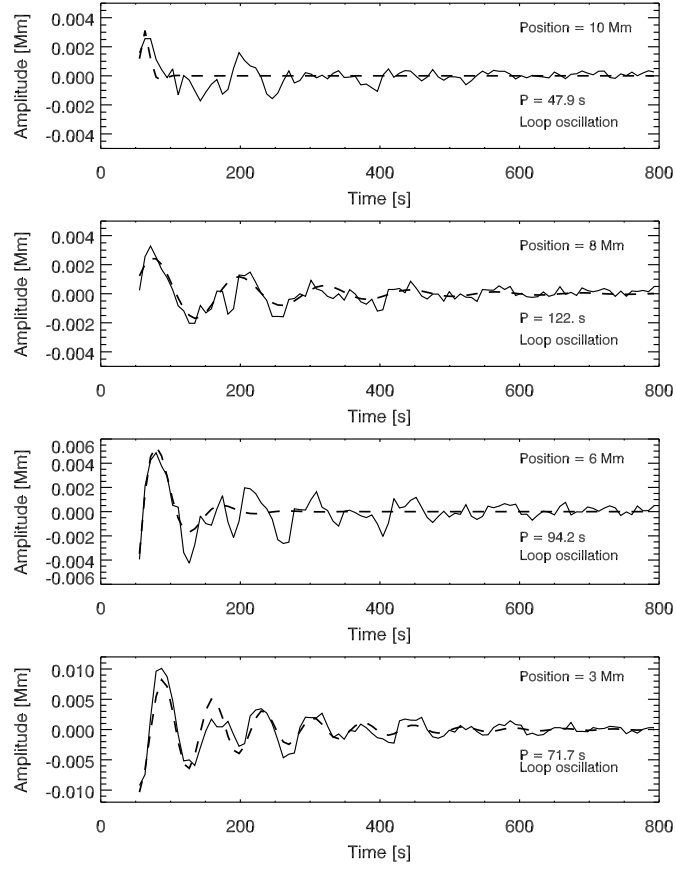
Figure 6.13: Displacement of the top loop as a function of time for different positions of the initial velocity pulse.

$$\frac{\partial^2 \psi}{\partial r^2} + \frac{1}{r}\frac{\partial \psi}{\partial r} + \left[\frac{\omega^2}{C_S^2} - \frac{m^2}{r^2}\right]\psi \, = \, 0 \; , \tag{6.11}$$

with a solution of the form,

$$\psi(r) \, = \, \psi_A \, J_m\!\left(\frac{\omega r}{C_S}\right) \; . \tag{6.12}$$

For $r \gg r^*$, the Alfvén speed dominates over the sound speed and the equation becomes,

$$\frac{\partial^2 \psi}{\partial r^2} + \frac{1}{r}\frac{\partial \psi}{\partial r} + \frac{1}{r^2}\left[\frac{\omega^2 R^2}{V_{A0}^2} - m^2\right]\psi \, = \, 0 \; , \tag{6.13}$$

with a solution,

$$\psi \, = \, \psi_B \sin(\kappa_m \ln(r/a)) + \psi_C \cos(\kappa_m \ln(r/a)) \; , \tag{6.14}$$

141
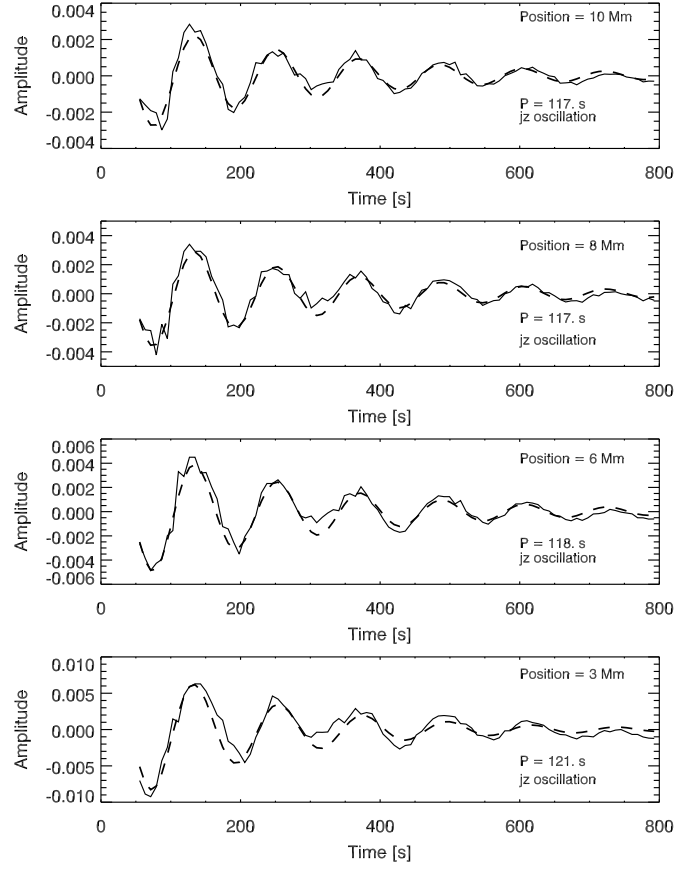
Figure 6.14: j_z component of the current density as a function of time for different positions of the initial velocity pulse.

where,

$$\kappa_m = \sqrt{\frac{\omega^2 R^2}{V_{A0}^2} - m^2} \ . \tag{6.15}$$

The boundary condition that $\psi = 0$ at $r = a$ means that,

$$\psi = \psi_B \sin(\kappa_m \ln(r/a)) \ . \tag{6.16}$$

Matching ψ and $\partial\psi/\partial r$ at $r = r^*$ means that $\psi_A = \psi_B$ and,

$$\kappa_m \ln(r^*/a) = -\left(n + \frac{1}{2}\right)\pi \ , \tag{6.17}$$

with n an integer. For the purely radial mode, m=0, and the lowest frequency mode (n=0),

$$\omega \;=\; \frac{V_{A0}\pi}{2R\ln(r^*/a)} \;=\; \frac{V_{A0}\pi}{2R}\left[\ln\left(\frac{RC_S}{aV_{A0}}\right)\right]^{-1}. \qquad (6.18)$$

The simulations have the following parameters: $R = 30$ Mm, $a = 20\text{-}50$ Mm (a circular boundary is assumed in the above analytic derivation), $V_{A0} = 1262$ kms^{-1} and $C_S = 162$ kms^{-1}. Therefore $r^* = 3.85$ Mm and for the range of values of a we find ω=0.026-0.040 rads^{-1}. This translates into periods between 157 and 244 s. This range of periods is larger than the oscillation period measured in the loop displacement and the oscillation period of j_z at the centre of the X-point. For a higher harmonic, n=1, we find P=52-81 s which is comparable to the loop displacement period.

6.6 Discussion

In this chapter we have presented numerical simulations of dense loops in the vicinity of a magnetic X-point that is perturbed by a fast magnetoacoustic circular pulse. This study extends the work of e.g. Craig and McClymont (1991); McLaughlin and Hood (2004, 2006); McLaughlin et al. (2009) where a perturbed X-point was studied but no other density structures such as loops were present in the region. The oscillatory behaviour of the X-point seen in the periodic variation of j_z is consistent with the previous studies and we show that the dense loops situated above and below the X-point respond to the velocity pulse and also display periodic oscillations. This study was motivated by the SDO/AIA observation of coronal loops oscillating in anti-phase presented in Chapter 5. The loops in the simulations are observed to oscillate in anti-phase to one another and the initial perturbation of both loops is directed inwards towards the X-point. This inwardly directed behaviour was a key feature of the observation and it is difficult to imagine how this motion could be excited by a flare blast wave. The observations were interpreted as a signature of slipping field lines due to the flare reconnection which is a signature of reconnection in 3D. Although we have shown that anti-phase oscillations of loops located in different topological regions about an X-point can be excited, this work would need to be extended to 3D in order to fully investigate the observations and the proposed mechanism.

Figure 6.3 shows the displacement-time oscillation of the loop located in the top quadrant and the oscillation of j_z at the X-point. The periodicity of j_z, 119 s, is 1.7 times the loop oscillation period of 72 s. This difference is not a result of nonlinear effects since the pulse velocity is small (between 0.1% and 3% of the sound speed)

and variations of A show the same periodicity.

Analytical expressions describing the period and decay time of the oscillatory behaviour of the X-point given in Eq. (6.1) were derived semi-analytically and numerically (Craig and McClymont 1991) and depend on the Lundquist number (or the resistivity). We show that varying the resistivity has no effect on the period or damping time of either the loop oscillations or the behaviour of the X-point. We also investigate the effect of varying the pressure, the velocity amplitude and the initial location of the circular velocity pulse. Varying the pressure leads to a variation of the temperature and the sound speed of the plasma. An increase in the pressure above 0.05 as shown in the top two plots of figure 6.9 leads to a sound speed that is larger than the Alfvén speed and which no longer represents coronal conditions. The figures for both the loop and j_z variation show that the oscillation amplitudes increase as the pressure decreases. Varying the velocity amplitude has no effect on the period of oscillation for small velocities. As the amplitude increases to 1, the velocity amplitude becomes nonlinear. The oscillation amplitudes also increase linearly as the velocity amplitude is increased. The variation in the initial position of the circular velocity pulse shows that the closer the pulse is to the X-point the larger the amplitude and the better the loop displacement oscillations can be fitted with a damped cosine curve. The variation of j_z shows a small increase in the period from 117 s to 121 s and a small increase in the amplitude as the pulse is brought nearer to the X-point.

A question that arises from the numerical simulations is, are the loops oscillating as normal modes? The TLOs observed with AIA are assumed to be oscillating as fundamental kink modes however in the simulations the fast magnetoacoustic pulse does not excite all parts of the loop at the same time, and so therefore is likely to excite harmonic modes. In addition, because the simulations are 2D and the curved loops represent infinite plasma slabs in the ignorable direction, we excite vertically polarised modes rather than horizontally polarised modes (e.g. Selwa et al. 2006). Reflections from the x boundary and the oscillation of the X-point itself may have a greater effect in dictating the mode of the loop oscillation and may be the reason why the loop has a periodicity that is less than that of the X-point. Launching a circular pulse in the perpendicular velocity leads to significant reflections from the x boundary because the width of the domain is relatively short compared to its height and it has fixed boundaries so that the loops are line tied. The pulse hits the x boundary just after it hits the loop tops and parallel velocity components, mainly located along the separatrix lines, are also excited. Therefore the loop oscillation may not be a normal mode of the loop but might instead be driven due to the velocity
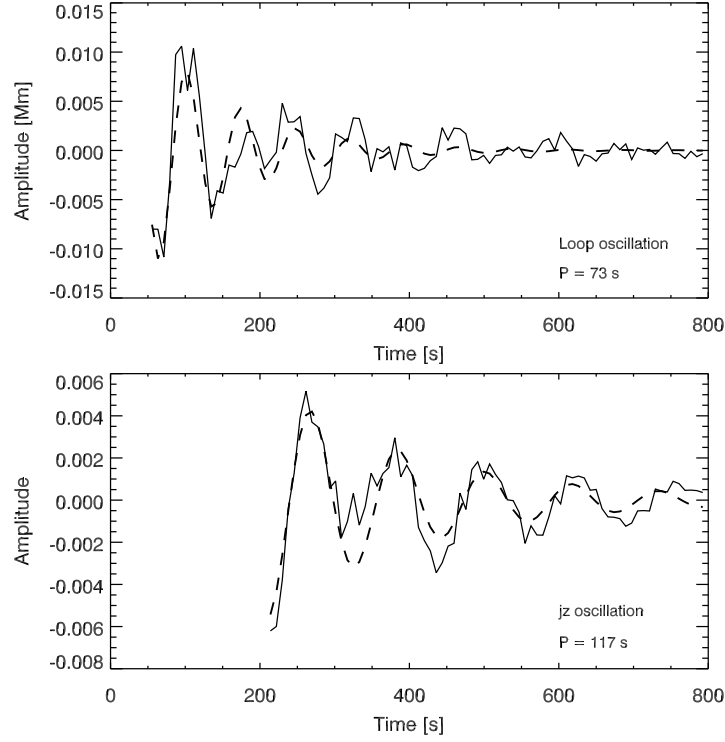
Figure 6.15: *Upper*: Time displacement of the density of the top loop fitted with a damped cosine curve. *Lower*: j_z oscillation at the centre of the X-point at position $(0, 0)$. The velocity pulse is a Gaussian pulse centered at the X-point rather than a circular annulus and has an amplitude $A = 0.01$.

reflections from the x boundary possibly combined with the parallel velocity along the separatrix lines.

An alternative approach to the circular perpendicular velocity pulse is an initially Gaussian velocity pulse centred at the X-point. This pulse is similar to the pulse described by Eq. (6.7) but with the sine term replaced by $\exp(-(x^2 + y^2)/(2w^2))$ where $w = 2$ Mm. Initial simulations with this velocity pulse also show anti-phase oscillations of the loops with periods comparable to those obtained with a circular pulse. Figure 6.15 shows the oscillatory behaviour of the loop in the top quadrant and the current density due to a Gaussian pulse. Oscillations in the current density at the X-point are observed with similar periodicity to before however clear oscillations are not observed until 200 s into the simulation, after approximately two loop oscillation periods.

145

Chapter 7

Summary

In this thesis, three observational studies and one numerical study of transverse loop oscillations (TLOs) in the solar corona are presented. The first observational study examined multiple TLOs in three limb active regions observed by SDO/AIA, whilst the second and third observations concentrated on loops seen in only one active region that display unusual oscillatory behaviour. The nature of the second and third observations suggest a direct link between their excitation and the flare reconnection processes, rather than the blast wave excitation mechanism assumed as the oscillation trigger in the first study. The numerical work was motivated by the third observational study of coronal loops oscillating transversely and in anti-phase to one another, to see if such anti-phase behaviour of two loops anchored in different topological regions can be modelled. Here we summarise each study and their original contributions to solar physics.

In Chapter 3, eleven TLOs seen in 171 Å AIA observations of three eruptive active regions were analysed. This is an important study as it significantly increased the number of reported TLO events, thereby helping to build up a better statistical picture of TLOs by measuring their periods and damping times. The loops in this study were found to have periods in the range of $100 - 600$ s and damping times in the range of $170 - 770$ s. A comparison of TLO periods and damping times have been used in previous studies to draw conclusions about which damping mechanisms are responsible for the observed rapid damping (e.g. Ofman and Aschwanden 2002). Comparing the results from this study with previous studies of TLOs, a scaling law was found that is consistent with resonant absorption. However since vital information on the loop properties such as the density and the width of the density inhomogeneous layer is unavailable this result must be viewed with caution.

In addition to applying the technique of coronal seismology to probe the local magnetic field strength, finding a range of $4 - 18$ G, analytical and Bayesian seismology techniques were also discussed. Both of these techniques assume that the TLOs are damped by the mechanism of resonant absorption and the Bayesian technique also takes into account the errors on the period and damping times. These techniques construct a 3D parameter space in the density contrast, inhomogeneity length scale and the Alfvén travel time, and if one of these parameters is determined from observations, then the other two parameters are constrained. Unfortunately in this study an accurate estimate of any one of the three parameters is not available. Combining AIA observations of TLOs with spectroscopic observations of the same event using instruments such as EIS on Hinode or NASA's IRIS satellite could provide accurate estimates of both the density contrast and the oscillatory information of loops. Such a study has been attempted by Van Doorsselaere et al. (2008) who studied a TLO using the imaging and spectroscopic capabilities of EIS. The periodicity of the TLO was determined from the Doppler shift and an estimate was made of the loop density contrast. Although in this case the loop displacement amplitude was below the spatial resolution of AIA, larger amplitude TLOs could be studied both spatially and spectroscopically by different instruments to get an accurate estimate of, for example, the magnetic field strength or the inhomogeneity length scale. It has been suggested that coronal seismology could be performed by complementing EUV observations of large TLOs with radio observations of type IV bursts (Zaqarashvili et al. 2013) since the frequency of radio emission depends upon the height and therefore the density of the plasma. A future study of a TLO combining EUV and radio observations could provide both the density and oscillatory information needed for an accurate estimate of the coronal magnetic field strength.

A limitation of TLO studies are that they are human intensive. TLOs are not easily automatically detected or analysed and therefore there is an inherent bias towards the study of large amplitude loops on the solar limb, since these events often display the best contrast with the background plasma. A future study that considers multiple loops in an active region which are observed in multiple AIA bandpasses would also be of interest. The majority of reported TLOs are seen in the 171 Å bandpass and in order to get a more complete picture of the behaviour of TLOs, observations across a number of bandpasses are needed.

In Chapter 4 the active region observed on 03/11/2010 and analysed in Chapter 3 was further studied in the 131 Å AIA bandpass. In this event, a loop larger than

those in the 171 Å bandpass was observed to the south of the active region and after the flare, during the CME eruption. This observation is the first analysis of a higher harmonic vertical TLO in a hot coronal loop. The oscillation has a period of 302 ± 14 s (291 ± 9 s) and a damping time of 306 ± 43 s (487 ± 125 s) for the first (second) strand. Intensity variations are observed along the loop and intensity oscillations that can be fitted with a damped cosine curve are observed at two points along the loop. An estimate of the 3D geometry is obtained from a comparison between STEREO-B and SDO viewpoints allowing the mode of the 5-min-period oscillation to be modelled.

This first observation of a TLO in hot coronal lines underlines the new capability of SDO/AIA of performing detailed spatial observations of the hot corona, which had been impossible with instruments such as TRACE. Coronal oscillations have been observed in hot flare lines by the SUMER spectrometer on SOHO, although in most of these cases spatial observations of the loops were unavailable. The oscillations were only observed in the Doppler shift in velocity and interpreted as slow magneto-acoustic oscillations of coronal loops. This observation clearly demonstrates that TLOs can exist in hot coronal lines. By combining high-cadence spatial observations from instruments such as AIA with spectrometer observations from HINODE/EIS, hot coronal oscillations and the distinctions between transverse and longitudinal modes may be studied in more detail. The loop oscillation is found to be vertically polarised and the detected intensity variations with relative amplitude between 0.1-0.3 are consistent with this conclusion. The forward modelling of the oscillation also supports a vertically rather than horizontally polarised mode interpretation. The loop was found to oscillate exclusively as a harmonic overtone. A $180°$ phase change is observed along the southern loop leg, indicating the presence of a node. The forward modelling of the different modes of oscillation suggest that the loop is oscillating either as a second or third harmonic. Since only one node is seen along the loop and the oscillations in the northern loop leg are hidden by the contrast with the background, the order of the mode cannot be confirmed. An interesting feature of this observation is that the oscillation is dominated by a higher harmonic and the fundamental mode is suppressed.

A key finding of this study is that the excitation mechanism of this TLO in a hot loop differs from the excitation mechanism suggested for TLOs observed in cooler bandpasses. In this case, reconnection processes may form a post flare loop and release the loop from the top (or even push it down towards the solar surface) re-

sulting in a vertically polarised mode. This is in contrast to the model of a blast wave hitting loops and causing transverse (often horizontally polarised) oscillations, which is often proposed as the excitation mechanism for cooler loops.

The third observational study, presented in Chapter 5, is another unusual TLO event that is also shown to be directly linked to the flare reconnection processes. This study differs from the previous two as the active region is observed on the solar disk rather than on the limb and oscillating loops are observed in three AIA bandpasses, 171 Å, 193 Å, and 211 Å. A flare eruption located close to the eastern loop footpoints excites TLOs and the 171 Å loop is seen to oscillate in anti-phase compared to the loops seen in the 193 Å and 211 Å bandpasses. The anti-phase oscillations with periods of approximately $180 - 220$ s are initially directed inwards so that the loops oscillate towards each other, which is unexpected if a flare blast wave is considered to be the excitation mechanism. The magnetic topology of the active region is probed by using a Potential Field Source Surface (PFSS) model to extrapolate the magnetic field from the photosphere. Comparing this with the position of the observed loops suggests that the eastern loop footpoint of the 171 Å loop is located in a different topological region to those of the 193 and 211 Å loops. We propose that the transverse oscillations are excited by the flare reconnection processes and in particular that they are the signatures of slipping field lines either as a direct result of slip-running reconnection or reconnection involving a 3D null point. Field lines might slip across quasi-separatrix layers (QSLs) (or in the vicinity of a null point) situated close to the eastern loop foot points which then perturb the loops in the vicinity of the field lines causing them to either move downwards (e.g. the 193/211 Å loops) or upwards (e.g. the 171 Å loop). As a result the loops move in anti-phase with respect to one another.

This observation suggests that TLOs can be used as a tool to probe the local magnetic topology and can indicate for example where the slipping of field lines is taking place. Slipping field lines are difficult to observe in EUV observations but TLOs are comparatively easier to observe with instruments such as AIA. Observations such as this can then complement extrapolation techniques to build up a detailed picture of an active region magnetic topology and to study any dynamic processes such as the slipping of field lines due to reconnection that may be occurring. A study comparing projected loop paths from STEREO/EUVI with extrapolated potential magnetic field lines (Sandman et al. 2009) has shown misalignment angles of between 20°- 40° between the projected loops and the extrapolated field lines. This

suggests a need for more realistic models of the coronal magnetic field.

Lastly in Chapter 6 we perform numerical simulations that are motivated by the observation of anti-phase TLOs presented in Chapter 5. Using the Lare2D code two dense loops located in different topological regions above and below a magnetic X-point configuration are modelled. A fast magnetoacoustic pulse perpendicular to the magnetic field is launched which initially splits into an inwardly traveling component directed towards the X-point and an outwardly traveling component directed towards the loops. The circular pulse excites the loops to oscillate transversely and to have their initial perturbation directed inwards towards the X-point. This demonstrates that such anti-phase oscillations of TLOs located in different topological regions can be modelled. It is proposed that the observation is a signature of slipping field lines which is a process that only occurs in 3D reconnection models. Therefore to more closely match the observation in Chapter 5 this model needs to be extended to 3D. The effect of the resistivity, pressure, velocity pulse amplitude and velocity pulse location on the loop displacement oscillations and the X-point oscillation was also investigated. A key result is that the periodicity of both the X-point and the displacement of the loop are independent of the resistivity. This contradicts the work of Craig and McClymont (1991) who derived relations linking the period and damping time of the oscillatory motion of the X-point to the Lundquist number and therefore the resistivity.

It is unclear from this study whether the loops oscillate as normal modes or if their oscillations are driven by, for example, the velocity reflections from the x boundaries. The period of the loop displacement is found to be 72 s compared to the period of the X-point which is 1.7 times larger than this at 119 s. An alternative approach to the circular pulse, and one which might model a fast wave generated by the reconnection rather than a pulse causing both reconnection and loop oscillations simultaneously, is an initial Gaussian perpendicular velocity pulse at the centre of the X-point. An experiment with a Gaussian pulse located at the centre of the X-point rather than the circular pulse perturbed anti-phase loop oscillations with similar periods to the circular pulse and oscillations in the current density that began at a later time (200 s) to the previous simulations.

Bibliography

C. E. Alissandrakis, C. Gontikakis, and H. C. Dara. Determination of the True Shape of Coronal Loops. *Sol. Phys.*, 252:73–87, October 2008. doi: 10.1007/s11207-008-9242-4.

J. Andries, M. Goossens, J. V. Hollweg, I. Arregui, and T. Van Doorsselaere. Coronal loop oscillations. Calculation of resonantly damped MHD quasi-mode kink oscillations of longitudinally stratified loops. *A&A*, 430:1109–1118, February 2005a. doi: 10.1051/0004-6361:20041832.

J. Andries, I. Arregui, and M. Goossens. Determination of the Coronal Density Stratification from the Observation of Harmonic Coronal Loop Oscillations. *ApJ*, 624:L57–L60, May 2005b. doi: 10.1086/430347.

S. Anfinogentov, G. Nisticò, and V. M. Nakariakov. Decay-less kink oscillations in coronal loops. *A&A*, 560:A107, December 2013. doi: 10.1051/0004-6361/201322094.

H. M. Antia, A. Bhatnagar, and P. Ulmschneider, editors. *Lectures on Solar Physics*, volume 619 of *Lecture Notes in Physics, Berlin Springer Verlag*, 2003.

P. Antolin and E. Verwichte. Transverse Oscillations of Loops with Coronal Rain Observed by Hinode/Solar Optical Telescope. *ApJ*, 736:121, August 2011. doi: 10.1088/0004-637X/736/2/121.

T. D. Arber, A. W. Longbottom, C. L. Gerrard, and A. M. Milne. A Staggered Grid, Lagrangian-Eulerian Remap Code for 3-D MHD Simulations. *J. Comput. Phys.*, 171:151–181, 2001.

I. Arregui and A. Asensio Ramos. Bayesian Magnetohydrodynamic Seismology of Coronal Loops. *ApJ*, 740:44–+, October 2011. doi: 10.1088/0004-637X/740/1/44.

I. Arregui, J. Andries, T. Van Doorsselaere, M. Goossens, and S. Poedts. MHD seismology of coronal loops using the period and damping of quasi-mode kink oscillations. *A&A*, 463:333–338, February 2007. doi: 10.1051/0004-6361:20065863.

I. Arregui, J. L. Ballester, and M. Goossens. On the Scaling of the Damping Time for Resonantly Damped Oscillations in Coronal Loops. *ApJ*, 676:L77–L80, March 2008. doi: 10.1086/587098.

M. J. Aschwanden. *Physics of the Solar Corona. An Introduction with Problems and Solutions (2nd edition)*. Springer, December 2005.

M. J. Aschwanden and C. J. Schrijver. Coronal Loop Oscillations Observed with Atmospheric Imaging Assembly—Kink Mode with Cross-sectional and Density Oscillations. *ApJ*, 736:102–+, August 2011. doi: 10.1088/0004-637X/736/2/102.

M. J. Aschwanden and J. Terradas. The Effect of Radiative Cooling on Coronal Loop Oscillations. *ApJ*, 686:L127–L130, October 2008. doi: 10.1086/592963.

M. J. Aschwanden, J. S. Newmark, J.-P. Delaboudinière, W. M. Neupert, J. A. Klimchuk, G. A. Gary, F. Portier-Fozzani, and A. Zucker. Three-dimensional Stereoscopic Analysis of Solar Active Region Loops. I. SOHO/EIT Observations at Temperatures of (1.0-1.5) X 10ˆ6 K. *ApJ*, 515:842–867, April 1999a. doi: 10.1086/307036.

M. J. Aschwanden, L. Fletcher, C. J. Schrijver, and D. Alexander. Coronal Loop Oscillations Observed with the Transition Region and Coronal Explorer. *ApJ*, 520:880–894, August 1999b. doi: 10.1086/307502.

M. J. Aschwanden, B. de Pontieu, C. J. Schrijver, and A. M. Title. Transverse Oscillations in Coronal Loops Observed with TRACE II. Measurements of Geometric and Physical Parameters. *Sol. Phys.*, 206:99–132, March 2002. doi: 10.1023/A:1014916701283.

M. J. Aschwanden, R. W. Nightingale, J. Andries, M. Goossens, and T. Van Doorsselaere. Observational Tests of Damping by Resonant Absorption in Coronal Loop Oscillations. *ApJ*, 598:1375–1386, December 2003. doi: 10.1086/379104.

M. J. Aschwanden, J.-P. Wülser, N. V. Nitta, and J. R. Lemen. First Three-Dimensional Reconstructions of Coronal Loops with the STEREO A and B Spacecraft. I. Geometry. *ApJ*, 679:827–842, May 2008. doi: 10.1086/529542.

A. Asensio Ramos, M. J. Martínez González, and J. A. Rubiño-Martín. Bayesian inversion of Stokes profiles. *A&A*, 476:959–970, December 2007. doi: 10.1051/0004-6361:20078107.

G. Aulanier, E. Pariat, P. Démoulin, and C. R. DeVore. Slip-Running Reconnection in Quasi-Separatrix Layers. *Sol. Phys.*, 238:347–376, November 2006. doi: 10.1007/s11207-006-0230-2.

G. Aulanier, L. Golub, E. E. DeLuca, J. W. Cirtain, R. Kano, L. L. Lundquist, N. Narukage, T. Sakao, and M. A. Weber. Slipping Magnetic Reconnection in Coronal Loops. *Science*, 318:1588–, December 2007. doi: 10.1126/science.1146143.

H. M. Bain, S. Krucker, L. Glesener, and R. P. Lin. Radio Imaging of Shock-accelerated Electrons Associated with an Erupting Plasmoid on 2010 November 3. *ApJ*, 750:44, May 2012. doi: 10.1088/0004-637X/750/1/44.

C. S. Brady and T. D. Arber. Damping of vertical coronal loop kink oscillations through wave tunneling. *A&A*, 438:733–740, August 2005. doi: 10.1051/0004-6361:20042527.

D. H. Brooks, H. P. Warren, and I. Ugarte-Urra. Solar Coronal Loops Resolved by Hinode and the Solar Dynamics Observatory. *ApJ*, 755:L33, August 2012. doi: 10.1088/2041-8205/755/2/L33.

L. Carcedo, D. S. Brown, A. W. Hood, T. Neukirch, and T. Wiegelmann. A Quantitative Method to Optimise Magnetic Field Line Fitting of Observed Coronal Loops. *Sol. Phys.*, 218:29–40, December 2003. doi: 10.1023/B:SOLA.0000013045.65499.da.

X. Cheng, J. Zhang, Y. Liu, and M. D. Ding. Observing Flux Rope Formation During the Impulsive Phase of a Solar Eruption. *ApJ*, 732:L25+, May 2011. doi: 10.1088/2041-8205/732/2/L25.

F. C. Cooper, V. M. Nakariakov, and D. Tsiklauri. Line-of-sight effects on observability of kink and sausage modes in coronal structures with imaging telescopes. *A&A*, 397:765–770, January 2003. doi: 10.1051/0004-6361:20021556.

I. J. D. Craig and A. N. McClymont. Dynamic magnetic reconnection at an X-type neutral point. *ApJ*, 371:L41–L44, April 1991. doi: 10.1086/185997.

J. L. Culhane, L. K. Harra, A. M. James, K. Al-Janabi, L. J. Bradley, R. A. Chaudry, K. Rees, J. A. Tandy, P. Thomas, M. C. R. Whillock, B. Winter, G. A.

Doschek, C. M. Korendyke, C. M. Brown, S. Myers, J. Mariska, J. Seely, J. Lang, B. J. Kent, B. M. Shaughnessy, P. R. Young, G. M. Simnett, C. M. Castelli, S. Mahmoud, H. Mapson-Menard, B. J. Probyn, R. J. Thomas, J. Davila, K. Dere, D. Windt, J. Shea, R. Hagood, R. Moye, H. Hara, T. Watanabe, K. Matsuzaki, T. Kosugi, V. Hansteen, and Ø. Wikstol. The EUV Imaging Spectrometer for Hinode. *Sol. Phys.*, 243:19–61, June 2007. doi: 10.1007/s01007-007-0293-1.

I. De Moortel and C. S. Brady. Observation of Higher Harmonic Coronal Loop Oscillations. *ApJ*, 664:1210–1213, August 2007. doi: 10.1086/518830.

I. De Moortel and D. J. Pascoe. Putting Coronal Seismology Estimates of the Magnetic Field Strength to the Test. *ApJ*, 699:L72–L75, July 2009. doi: 10.1088/0004-637X/699/2/L72.

I. De Moortel, A. W. Hood, J. Ireland, and T. D. Arber. Phase mixing of Alfvén waves in a stratified and open atmosphere. *A&A*, 346:641–651, June 1999.

I. De Moortel, A. W. Hood, and T. D. Arber. Phase mixing of Alfvén waves in a stratified and radially diverging, open atmosphere. *A&A*, 354:334–348, February 2000a.

B. De Pontieu, P. C. H. Martens, and H. S. Hudson. Chromospheric Damping of Alfvén Waves. *ApJ*, 558:859–871, September 2001. doi: 10.1086/322408.

B. De Pontieu, A. M. Title, J. Lemen, G. D. Kushner, D. J. Akin, B. Allard, T. Berger, P. Boerner, M. Cheung, C. Chou, J. F. Drake, D. W. Duncan, S. Freeland, G. F. Heyman, C. Hoffman, N. E. Hurlburt, R. W. Lindgren, D. Mathur, R. Rehse, D. Sabolish, R. Seguin, C. J. Schrijver, T. D. Tarbell, J.-P. Wuelser, C. J. Wolfson, C. Yanari, J. Mudge, N. Nguyen-Phuc, R. Timmons, R. van Bezooijen, I. Weingrod, R. Brookner, G. Butcher, B. Dougherty, J. Eder, V. Knagenhjelm, S. Larsen, D. Mansir, L. Phan, P. Boyle, P. N. Cheimets, E. E. DeLuca, L. Golub, R. Gates, E. Hertz, S. McKillop, S. Park, T. Perry, W. A. Podgorski, K. Reeves, S. Saar, P. Testa, H. Tian, M. Weber, C. Dunn, S. Eccles, S. A. Jaeggli, C. C Kankelborg, K. Mashburn, N. Pust, L. Springer, R. Carvalho, L. Kleint, J. Marmie, E. Mazmanian, T. M. D. Pereira, S. Sawyer, J. Strong, S. P. Worden, M. Carlsson, V. H. Hansteen, J. Leenaarts, M. Wiesmann, J. Aloise, K.-C. Chu, R. I. Bush, P. H. Scherrer, P. Brekke, J. Martinez-Sykora, B. W. Lites, S. W. McIntosh, H. Uitenbroek, T. J. Okamoto, M. A. Gummin, G. Auker, P. Jerram, P. Pool, and N. Waltham. The Interface Region Imaging Spectrograph (IRIS). *ArXiv e-prints*, January 2014.

V. Delouille, J. de Patoul, J. F. Hochedez, L. Jacques, and J. P. Antoine. Wavelet Spectrum Analysis Of Eit/Soho Images. *Sol. Phys.*, 228:301–321, May 2005. doi: 10.1007/s11207-005-5620-3.

P. Démoulin. Extending the concept of separatrices to QSLs for magnetic reconnection. *Advances in Space Research*, 37:1269–1282, 2006. doi: 10.1016/j.asr.2005.03.085.

P. Démoulin, J. C. Henoux, E. R. Priest, and C. H. Mandrini. Quasi-Separatrix layers in solar flares. I. Method. *A&A*, 308:643–655, April 1996.

P. Démoulin, L. G. Bagala, C. H. Mandrini, J. C. Henoux, and M. G. Rovira. Quasi-separatrix layers in solar flares. II. Observed magnetic configurations. *A&A*, 325: 305–317, September 1997.

A. J. Díaz. Fast magnetohydrodynamic oscillations in an elliptical coronal arcade. *A&A*, 456:737–746, September 2006. doi: 10.1051/0004-6361:20065184.

B. N. Dwivedi and F. b. E. N. Parker. *Dynamic Sun*. Cambridge University Press, May 2003.

M. V. Dymova and M. S. Ruderman. Resonantly damped oscillations of longitudinally stratified coronal loops. *A&A*, 457:1059–1070, October 2006. doi: 10.1051/0004-6361:20065051.

B. Edlén. Die Deutung der Emissionslinien im Spektrum der Sonnenkorona. Mit 6 Abbildungen. *ZAp*, 22:30, 1943.

P. M. Edwin and B. Roberts. Wave propagation in a magnetic cylinder. *Sol. Phys.*, 88:179–191, October 1983. doi: 10.1007/BF00196186.

G. H. Fisher, R. C. Canfield, and A. N. McClymont. Flare loop radiative hydrodynamics. V - Response to thick-target heating. VI - Chromospheric evaporation due to heating by nonthermal electrons. VII - Dynamics of the thick-target heated chromosphere. *ApJ*, 289:414–441, February 1985. doi: 10.1086/162901.

L. Fletcher, B. R. Dennis, H. S. Hudson, S. Krucker, K. Phillips, A. Veronig, M. Battaglia, L. Bone, A. Caspi, Q. Chen, P. Gallagher, P. T. Grigis, H. Ji, W. Liu, R. O. Milligan, and M. Temmer. An Observational Overview of Solar Flares. *Space Sci. Rev.*, 159:19–106, September 2011. doi: 10.1007/s11214-010-9701-8.

P. V. Foukal. *Solar Astrophysics, 3rd, Revised Edition*. WILEY-VCH, 2013.

C. Foullon, L. Fletcher, I. G. Hannah, E. Verwichte, B. Cecconi, V. M. Nakariakov, K. J. H. Phillips, and B. L. Tan. From Large-scale Loops to the Sites of Dense Flaring Loops: Preferential Conditions for Long-period Pulsations in Solar Flares. *ApJ*, 719:151–165, August 2010. doi: 10.1088/0004-637X/719/1/151.

C. Foullon, E. Verwichte, V. M. Nakariakov, K. Nykyri, and C. J. Farrugia. Magnetic Kelvin-Helmholtz Instability at the Sun. *ApJ*, 729:L8+, March 2011. doi: 10.1088/2041-8205/729/1/L8.

C. Foullon, E. Verwichte, K. Nykyri, M. J. Aschwanden, and I. G. Hannah. Kelvin-Helmholtz Instability of the CME Reconnection Outflow Layer in the Low Corona. *ApJ*, 767:170, April 2013. doi: 10.1088/0004-637X/767/2/170.

M. Fränz and D. Harper. Heliospheric coordinate systems. *Planet. Space Sci.*, 50:217–233, February 2002. doi: 10.1016/S0032-0633(01)00119-2.

G. A. Gary. Plasma Beta above a Solar Active Region: Rethinking the Paradigm. *Sol. Phys.*, 203:71–86, October 2001. doi: 10.1023/A:1012722021820.

G. A. Gary, Q. Hu, and J. K. Lee. A Rapid, Manual Method to Map Coronal-Loop Structures of an Active Region Using Cubic Bézier Curves and Its Applications to Misalignment Angle Analysis. *Sol. Phys.*, August 2013. doi: 10.1007/s11207-013-0359-8.

M. Goossens, editor. *An introduction to plasma astrophysics and magnetohydrodynamics*, volume 294 of *Astrophysics and Space Science Library*, October 2003.

M. Goossens, J. Andries, and M. J. Aschwanden. Coronal loop oscillations. An interpretation in terms of resonant absorption of quasi-mode kink oscillations. *A&A*, 394:L39–L42, November 2002. doi: 10.1051/0004-6361:20021378.

M. Goossens, I. Arregui, J. L. Ballester, and T. J. Wang. Analytic approximate seismology of transversely oscillating coronal loops. *A&A*, 484:851–857, June 2008. doi: 10.1051/0004-6361:200809728.

M. Goossens, R. Erdélyi, and M. S. Ruderman. Resonant MHD Waves in the Solar Atmosphere. *Space Sci. Rev.*, 158:289–338, July 2011. doi: 10.1007/s11214-010-9702-7.

S. Gosain and C. Foullon. Dual Trigger of Transverse Oscillations in a Prominence by EUV Fast and Slow Coronal Waves: SDO/AIA and STEREO/EUVI Observations. *ApJ*, 761:103, December 2012. doi: 10.1088/0004-637X/761/2/103.

156

M. Gruszecki, K. Murawski, M. Selwa, and L. Ofman. Numerical simulations of vertical oscillations of a multi-stranded coronal loop. *A&A*, 460:887–892, December 2006. doi: 10.1051/0004-6361:20065426.

M. Gruszecki, S. Vasheghani Farahani, V. M. Nakariakov, and T. D. Arber. Magnetoacoustic shock formation near a magnetic null point. *A&A*, 531:A63, July 2011. doi: 10.1051/0004-6361/201116753.

B. N. Handy, L. W. Acton, C. C. Kankelborg, C. J. Wolfson, D. J. Akin, M. E. Bruner, R. Caravalho, R. C. Catura, R. Chevalier, D. W. Duncan, C. G. Edwards, C. N. Feinstein, S. L. Freeland, F. M. Friedlaender, C. H. Hoffmann, N. E. Hurlburt, B. K. Jurcevich, N. L. Katz, G. A. Kelly, J. R. Lemen, M. Levay, R. W. Lindgren, D. P. Mathur, S. B. Meyer, S. J. Morrison, M. D. Morrison, R. W. Nightingale, T. P. Pope, R. A. Rehse, C. J. Schrijver, R. A. Shine, L. Shing, K. T. Strong, T. D. Tarbell, A. M. Title, D. D. Torgerson, L. Golub, J. A. Bookbinder, D. Caldwell, P. N. Cheimets, W. N. Davis, E. E. Deluca, R. A. McMullen, H. P. Warren, D. Amato, R. Fisher, H. Maldonado, and C. Parkinson. The transition region and coronal explorer. *Sol. Phys.*, 187:229–260, July 1999. doi: 10.1023/A:1005166902804.

I. G. Hannah and E. P. Kontar. Multi-thermal dynamics and energetics of a coronal mass ejection in the low solar atmosphere. *A&A*, 553:A10, May 2013. doi: 10.1051/0004-6361/201219727.

M. A. Hapgood. Space physics coordinate transformations - A user guide. *Planet. Space Sci.*, 40:711–717, May 1992. doi: 10.1016/0032-0633(92)90012-D.

J. Hershaw, C. Foullon, V. M. Nakariakov, and E. Verwichte. Damped large amplitude transverse oscillations in an EUV solar prominence, triggered by large-scale transient coronal waves. *A&A*, 531:A53+, July 2011. doi: 10.1051/0004-6361/201116750.

J. Heyvaerts and E. R. Priest. Coronal heating by phase-mixed shear Alfven waves. *A&A*, 117:220–234, January 1983.

J. V. Hollweg and G. Yang. Resonance absorption of compressible magnetohydrodynamic waves at thin 'surfaces'. *J. Geophys. Res.*, 93:5423–5436, June 1988. doi: 10.1029/JA093iA06p05423.

K. Hori, K. Ichimoto, T. Sakurai, I. Sano, and Y. Nishino. Flare-associated Coronal Disturbances Observed with the Norikura Green-Line Imaging System.

I. A Coronal Mass Ejection Onset. *ApJ*, 618:1001–1011, January 2005. doi: 10.1086/426013.

K. Hori, K. Ichimoto, and T. Sakurai. Flare-Associated Oscillations in Coronal Multiple-Loops Observed with the Norikura Green-Line Imaging System. In K. Shibata, S. Nagata, & T. Sakurai, editor, *New Solar Physics with Solar-B Mission*, volume 369 of *Astronomical Society of the Pacific Conference Series*, pages 213–+, October 2007.

R. A. Howard, J. D. Moses, A. Vourlidas, J. S. Newmark, D. G. Socker, S. P. Plunkett, C. M. Korendyke, J. W. Cook, A. Hurley, J. M. Davila, W. T. Thompson, O. C. St Cyr, E. Mentzell, K. Mehalick, J. R. Lemen, J. P. Wuelser, D. W. Duncan, T. D. Tarbell, C. J. Wolfson, A. Moore, R. A. Harrison, N. R. Waltham, J. Lang, C. J. Davis, C. J. Eyles, H. Mapson-Menard, G. M. Simnett, J. P. Halain, J. M. Defise, E. Mazy, P. Rochus, R. Mercier, M. F. Ravet, F. Delmotte, F. Auchere, J. P. Delaboudiniere, V. Bothmer, W. Deutsch, D. Wang, N. Rich, S. Cooper, V. Stephens, G. Maahs, R. Baugh, D. McMullin, and T. Carter. Sun Earth Connection Coronal and Heliospheric Investigation (SECCHI). *Space Sci. Rev.*, 136: 67–115, April 2008. doi: 10.1007/s11214-008-9341-4.

J. A. Ionson. Resonant absorption of Alfvenic surface waves and the heating of solar coronal loops. *ApJ*, 226:650–673, December 1978. doi: 10.1086/156648.

B. Kliem, I. E. Dammasch, W. Curdt, and K. Wilhelm. Correlated Dynamics of Hot and Cool Plasmas in the Main Phase of a Solar Flare. *ApJ*, 568:L61–L65, March 2002. doi: 10.1086/340136.

T. Kosugi, K. Matsuzaki, T. Sakao, T. Shimizu, Y. Sone, S. Tachikawa, T. Hashimoto, K. Minesugi, A. Ohnishi, T. Yamada, S. Tsuneta, H. Hara, K. Ichimoto, Y. Suematsu, M. Shimojo, T. Watanabe, S. Shimada, J. M. Davis, L. D. Hill, J. K. Owens, A. M. Title, J. L. Culhane, L. K. Harra, G. A. Doschek, and L. Golub. The Hinode (Solar-B) Mission: An Overview. *Sol. Phys.*, 243:3–17, June 2007. doi: 10.1007/s11207-007-9014-6.

R. M. Kulsrud. *Plasma physics for astrophysics*. Princeton University Press, 2005.

J. R. Lemen, A. M. Title, D. J. Akin, P. F. Boerner, C. Chou, J. F. Drake, D. W. Duncan, C. G. Edwards, F. M. Friedlaender, G. F. Heyman, N. E. Hurlburt, N. L. Katz, G. D. Kushner, M. Levay, R. W. Lindgren, D. P. Mathur, E. L. McFeaters, S. Mitchell, R. A. Rehse, C. J. Schrijver, L. A. Springer, R. A. Stern, T. D. Tarbell, J.-P. Wuelser, C. J. Wolfson, C. Yanari, J. A. Bookbinder, P. N. Cheimets,

D. Caldwell, E. E. Deluca, R. Gates, L. Golub, S. Park, W. A. Podgorski, R. I. Bush, P. H. Scherrer, M. A. Gummin, P. Smith, G. Auker, P. Jerram, P. Pool, R. Soufli, D. L. Windt, S. Beardsley, M. Clapp, J. Lang, and N. Waltham. The Atmospheric Imaging Assembly (AIA) on the Solar Dynamics Observatory (SDO). *Sol. Phys.*, 275:17–40, January 2012. doi: 10.1007/s11207-011-9776-8.

R. P. Lin, B. R. Dennis, G. J. Hurford, D. M. Smith, A. Zehnder, P. R. Harvey, D. W. Curtis, D. Pankow, P. Turin, M. Bester, A. Csillaghy, M. Lewis, N. Madden, H. F. van Beek, M. Appleby, T. Raudorf, J. McTiernan, R. Ramaty, E. Schmahl, R. Schwartz, S. Krucker, R. Abiad, T. Quinn, P. Berg, M. Hashii, R. Sterling, R. Jackson, R. Pratt, R. D. Campbell, D. Malone, D. Landis, C. P. Barrington-Leigh, S. Slassi-Sennou, C. Cork, D. Clark, D. Amato, L. Orwig, R. Boyle, I. S. Banks, K. Shirey, A. K. Tolbert, D. Zarro, F. Snow, K. Thomsen, R. Henneck, A. McHedlishvili, P. Ming, M. Fivian, J. Jordan, R. Wanner, J. Crubb, J. Preble, M. Matranga, A. Benz, H. Hudson, R. C. Canfield, G. D. Holman, C. Crannell, T. Kosugi, A. G. Emslie, N. Vilmer, J. C. Brown, C. Johns-Krull, M. Aschwanden, T. Metcalf, and A. Conway. The Reuven Ramaty High-Energy Solar Spectroscopic Imager (RHESSI). *Sol. Phys.*, 210:3–32, November 2002. doi: 10.1023/A:1022428818870.

D. W. Longcope and L. Tarr. The Role of Fast Magnetosonic Waves in the Release and Conversion via Reconnection of Energy Stored by a Current Sheet. *ApJ*, 756: 192, September 2012. doi: 10.1088/0004-637X/756/2/192.

N. Lugaz, C. Downs, K. Shibata, I. I. Roussev, A. Asai, and T. I. Gombosi. Numerical Investigation of a Coronal Mass Ejection from an Anemone Active Region: Reconnection and Deflection of the 2005 August 22 Eruption. *ApJ*, 738:127, September 2011. doi: 10.1088/0004-637X/738/2/127.

M. Luna, J. Terradas, R. Oliver, and J. L. Ballester. Transverse Oscillations of Two Coronal Loops. *ApJ*, 676:717–727, March 2008. doi: 10.1086/528367.

J. T. Mariska. Observations of Solar Flare Doppler Shift Oscillations with the Bragg Crystal Spectrometer on Yohkoh. *ApJ*, 620:L67–L70, February 2005. doi: 10.1086/428611.

C. B. Markwardt. Non-linear Least-squares Fitting in IDL with MPFIT. In D. A. Bohlender, D. Durand, & P. Dowler, editor, *Astronomical Data Analysis Software and Systems XVIII*, volume 411 of *Astronomical Society of the Pacific Conference Series*, pages 251–+, September 2009.

S. Masson, E. Pariat, G. Aulanier, and C. J. Schrijver. The Nature of Flare Ribbons in Coronal Null-Point Topology. *ApJ*, 700:559–578, July 2009. doi: 10.1088/0004-637X/700/1/559.

M. P. McEwan, G. R. Donnelly, A. J. Díaz, and B. Roberts. On the period ratio $P_1/2P_2$ in the oscillations of coronal loops. *A&A*, 460:893–899, December 2006. doi: 10.1051/0004-6361:20065313.

J. A. McLaughlin and A. W. Hood. MHD wave propagation in the neighbourhood of a two-dimensional null point. *A&A*, 420:1129–1140, June 2004. doi: 10.1051/0004-6361:20035900.

J. A. McLaughlin and A. W. Hood. MHD mode coupling in the neighbourhood of a 2D null point. *A&A*, 459:641–649, November 2006. doi: 10.1051/0004-6361:20065558.

J. A. McLaughlin, I. De Moortel, A. W. Hood, and C. S. Brady. Nonlinear fast magnetoacoustic wave propagation in the neighbourhood of a 2D magnetic X-point: oscillatory reconnection. *A&A*, 493:227–240, January 2009. doi: 10.1051/0004-6361:200810465.

R. O. Milligan and B. R. Dennis. Velocity Characteristics of Evaporated Plasma Using Hinode/EUV Imaging Spectrometer. *ApJ*, 699:968–975, July 2009. doi: 10.1088/0004-637X/699/2/968.

R. O. Milligan, P. T. Gallagher, M. Mathioudakis, and F. P. Keenan. Observational Evidence of Gentle Chromospheric Evaporation during the Impulsive Phase of a Solar Flare. *ApJ*, 642:L169–L171, May 2006. doi: 10.1086/504592.

R. J. Morton and R. Erdélyi. Transverse Oscillations of a Cooling Coronal Loop. *ApJ*, 707:750–760, December 2009. doi: 10.1088/0004-637X/707/1/750.

T. Mrozek. Failed Eruption of a Filament as a Driver for Vertical Oscillations of Coronal Loops. *Sol. Phys.*, 270:191–203, May 2011. doi: 10.1007/s11207-011-9750-5.

V. M. Nakariakov and L. Ofman. Determination of the coronal magnetic field by coronal loop oscillations. *A&A*, 372:L53–L56, June 2001. doi: 10.1051/0004-6361:20010607.

V. M. Nakariakov and E. Verwichte. Coronal Waves and Oscillations. *Living Reviews in Solar Physics*, 2:3–+, July 2005.

V. M. Nakariakov, L. Ofman, E. E. Deluca, B. Roberts, and J. M. Davila. TRACE observation of damped coronal loop oscillations: Implications for coronal heating. *Science*, 285:862–864, August 1999. doi: 10.1126/science.285.5429.862.

V. M. Nakariakov, D. Tsiklauri, A. Kelly, T. D. Arber, and M. J. Aschwanden. Acoustic oscillations in solar and stellar flaring loops. *A&A*, 414:L25–L28, January 2004. doi: 10.1051/0004-6361:20031738.

G. Nisticò, V. M. Nakariakov, and E. Verwichte. Decaying and decayless transverse oscillations of a coronal loop. *A&A*, 552:A57, April 2013a. doi: 10.1051/0004-6361/201220676.

G. Nisticò, E. Verwichte, and V. M. Nakariakov. 3d reconstruction of coronal loops by the principal component analysis. *Entropy*, 15(10): 4520–4539, 2013b. ISSN 1099-4300. doi: 10.3390/e15104520. URL `http://www.mdpi.com/1099-4300/15/10/4520`.

K. Nykyri and C. Foullon. First magnetic seismology of the CME reconnection outflow layer in the low corona with 2.5-D MHD simulations of the Kelvin-Helmholtz instability. *Geophys. Res. Lett.*, 40:4154–4159, August 2013. doi: 10.1002/grl.50807.

L. Ofman and M. J. Aschwanden. Damping Time Scaling of Coronal Loop Oscillations Deduced from Transition Region and Coronal Explorer Observations. *ApJ*, 576:L153–L156, September 2002. doi: 10.1086/343886.

E. N. Parker. The Solar-Flare Phenomenon and the Theory of Reconnection and Annihiliation of Magnetic Fields. *ApJS*, 8:177, July 1963. doi: 10.1086/190087.

D. J. Pascoe and I. De Moortel. Standing Kink Modes in Three-dimensional Coronal Loops. *ApJ*, 784:101, April 2014. doi: 10.1088/0004-637X/784/2/101.

W. D. Pesnell, B. J. Thompson, and P. C. Chamberlin. The Solar Dynamics Observatory (SDO). *Sol. Phys.*, 275:3–15, January 2012. doi: 10.1007/s11207-011-9841-3.

H. E. Petschek. Magnetic Field Annihilation. *NASA Special Publication*, 50:425, 1964.

D. I. Pontin. Three-dimensional magnetic reconnection regimes: A review. *Advances in Space Research*, 47:1508–1522, May 2011. doi: 10.1016/j.asr.2010.12.022.

161

D. I. Pontin and I. J. D. Craig. Dynamic Three-dimensional Reconnection in a Separator Geometry with Two Null Points. *ApJ*, 642:568–578, May 2006. doi: 10.1086/500725.

E. R. Priest and T. G. Forbes. The magnetic nature of solar flares. *A&A Rev.*, 10: 313–377, 2002. doi: 10.1007/s001590100013.

E. R. Priest and D. I. Pontin. Three-dimensional null point reconnection regimes. *Physics of Plasmas*, 16(12):122101, December 2009. doi: 10.1063/1.3257901.

K. K. Reeves and L. Golub. Atmospheric Imaging Assembly Observations of Hot Flare Plasma. *ApJ*, 727:L52+, February 2011. doi: 10.1088/2041-8205/727/2/L52.

M. S. Ruderman and B. Roberts. The Damping of Coronal Loop Oscillations. *ApJ*, 577:475–486, September 2002. doi: 10.1086/342130.

T. Sakurai, M. Goossens, and J. V. Hollweg. Resonant behaviour of MHD waves on magnetic flux tubes. I - Connection formulae at the resonant surfaces. *Sol. Phys.*, 133:227–245, June 1991. doi: 10.1007/BF00149888.

A. W. Sandman, M. J. Aschwanden, M. L. Derosa, J. P. Wülser, and D. Alexander. Comparison of STEREO/EUVI Loops with Potential Magnetic Field Models. *Sol. Phys.*, 259:1–11, October 2009. doi: 10.1007/s11207-009-9383-0.

S. L. Savage, G. Holman, K. K. Reeves, D. B. Seaton, D. E. McKenzie, and Y. Su. Low-altitude Reconnection Inflow-Outflow Observations during a 2010 November 3 Solar Eruption. *ApJ*, 754:13, July 2012. doi: 10.1088/0004-637X/754/1/13.

K. H. Schatten, J. M. Wilcox, and N. F. Ness. A model of interplanetary and coronal magnetic fields. *Sol. Phys.*, 6:442–455, March 1969. doi: 10.1007/BF00146478.

P. H. Scherrer, J. Schou, R. I. Bush, A. G. Kosovichev, R. S. Bogart, J. T. Hoeksema, Y. Liu, T. L. Duvall, J. Zhao, A. M. Title, C. J. Schrijver, T. D. Tarbell, and S. Tomczyk. The Helioseismic and Magnetic Imager (HMI) Investigation for the Solar Dynamics Observatory (SDO). *Sol. Phys.*, 275:207–227, January 2012. doi: 10.1007/s11207-011-9834-2.

J. T. Schmelz, S. H. Saar, K. Nasraoui, V. L. Kashyap, M. A. Weber, E. E. DeLuca, and L. Golub. Multi-stranded and Multi-thermal Solar Coronal Loops: Evidence from Hinode X-ray Telescope and EUV Imaging Spectrometer Data. *ApJ*, 723: 1180–1187, November 2010. doi: 10.1088/0004-637X/723/2/1180.

162

J. Schou, P. H. Scherrer, R. I. Bush, R. Wachter, S. Couvidat, M. C. Rabello-Soares, R. S. Bogart, J. T. Hoeksema, Y. Liu, T. L. Duvall, D. J. Akin, B. A. Allard, J. W. Miles, R. Rairden, R. A. Shine, T. D. Tarbell, A. M. Title, C. J. Wolfson, D. F. Elmore, A. A. Norton, and S. Tomczyk. Design and Ground Calibration of the Helioseismic and Magnetic Imager (HMI) Instrument on the Solar Dynamics Observatory (SDO). *Sol. Phys.*, 275:229–259, January 2012. doi: 10.1007/s11207-011-9842-2.

C. J. Schrijver. Simulations of the Photospheric Magnetic Activity and Outer Atmospheric Radiative Losses of Cool Stars Based on Characteristics of the Solar Magnetic Field. *ApJ*, 547:475–490, January 2001. doi: 10.1086/318333.

C. J. Schrijver and D. S. Brown. Oscillations in the Magnetic Field of the Solar Corona in Response to Flares near the Photosphere. *ApJ*, 537:L69–L72, July 2000. doi: 10.1086/312753.

C. J. Schrijver and M. L. De Rosa. Photospheric and heliospheric magnetic fields. *Sol. Phys.*, 212:165–200, January 2003. doi: 10.1023/A:1022908504100.

C. J. Schrijver, M. J. Aschwanden, and A. M. Title. Transverse oscillations in coronal loops observed with TRACE I. An Overview of Events, Movies, and a Discussion of Common Properties and Required Conditions. *Sol. Phys.*, 206:69–98, March 2002. doi: 10.1023/A:1014957715396.

N. Seehafer. Determination of constant alpha force-free solar magnetic fields from magnetograph data. *Sol. Phys.*, 58:215–223, July 1978. doi: 10.1007/BF00157267.

N. Seehafer. A comparison of different solar magnetic field extrapolation procedures. *Sol. Phys.*, 81:69–80, November 1982. doi: 10.1007/BF00151981.

J. F. Seely and U. Feldman. Direct measurement of the increase in altitude of the soft X-ray emission region during a solar flare. *ApJ*, 280:L59–L62, May 1984. doi: 10.1086/184270.

M. Selwa, S. K. Solanki, K. Murawski, T. J. Wang, and U. Shumlak. Numerical simulations of impulsively generated vertical oscillations in a solar coronal arcade loop. *A&A*, 454:653–661, August 2006. doi: 10.1051/0004-6361:20054286.

P. J. A. Simões, L. Fletcher, H. S. Hudson, and A. J. B. Russell. Implosion of Coronal Loops during the Impulsive Phase of a Solar Flare. *ApJ*, 777:152, November 2013. doi: 10.1088/0004-637X/777/2/152.

P. A. Sweet. The Neutral Point Theory of Solar Flares. In B. Lehnert, editor, *Electromagnetic Phenomena in Cosmical Physics*, volume 6 of *IAU Symposium*, page 123, 1958.

J. Terradas and L. Ofman. Loop Density Enhancement by Nonlinear Magnetohydrodynamic Waves. *ApJ*, 610:523–531, July 2004. doi: 10.1086/421514.

J. Terradas, J. Andries, and E. Verwichte. Linear coupling between fast and slow MHD waves due to line-tying effects. *A&A*, 527:A132+, March 2011. doi: 10.1051/0004-6361/201015862.

W. T. Thompson. Coordinate systems for solar image data. *A&A*, 449:791–803, April 2006. doi: 10.1051/0004-6361:20054262.

J. Threlfall, C. E. Parnell, I. De Moortel, K. G. McClements, and T. D. Arber. Nonlinear wave propagation and reconnection at magnetic X-points in the Hall MHD regime. *A&A*, 544:A24, August 2012. doi: 10.1051/0004-6361/201219098.

S. Tomczyk, G. L. Card, T. Darnell, D. F. Elmore, R. Lull, P. G. Nelson, K. V. Streander, J. Burkepile, R. Casini, and P. G. Judge. An Instrument to Measure Coronal Emission Line Polarization. *Sol. Phys.*, 247:411–428, February 2008. doi: 10.1007/s11207-007-9103-6.

T. Török, G. Aulanier, B. Schmieder, K. K. Reeves, and L. Golub. Fan-Spine Topology Formation Through Two-Step Reconnection Driven by Twisted Flux Emergence. *ApJ*, 704:485–495, October 2009. doi: 10.1088/0004-637X/704/1/485.

D. Tothova, D. E. Innes, and G. Stenborg. Oscillations in the wake of a flare blast wave. *A&A*, 528:L12, April 2011. doi: 10.1051/0004-6361/201015272.

D. Tsiklauri, V. M. Nakariakov, T. D. Arber, and M. J. Aschwanden. Flare-generated acoustic oscillations in solar and stellar coronal loops. *A&A*, 422:351–355, July 2004. doi: 10.1051/0004-6361:20040299.

Y. Uchida. Diagnosis of Coronal Magnetic Structure by Flare-Associated Hydromagnetic Disturbances. *PASJ*, 22:341, 1970.

T. Van Doorsselaere, J. Andries, S. Poedts, and M. Goossens. Damping of Coronal Loop Oscillations: Calculation of Resonantly Damped Kink Oscillations of One-dimensional Nonuniform Loops. *ApJ*, 606:1223–1232, May 2004. doi: 10.1086/383191.

T. Van Doorsselaere, V. M. Nakariakov, and E. Verwichte. Coronal loop seismology using multiple transverse loop oscillation harmonics. *A&A*, 473:959–966, October 2007. doi: 10.1051/0004-6361:20077783.

T. Van Doorsselaere, V. M. Nakariakov, P. R. Young, and E. Verwichte. Coronal magnetic field measurement using loop oscillations observed by Hinode/EIS. *A&A*, 487:L17–L20, August 2008. doi: 10.1051/0004-6361:200810186.

T. Van Doorsselaere, V. M. Nakariakov, P. R. Young, and E. Verwichte. Coronal magnetic field measurement using loop oscillations observed by Hinode/EIS. *A&A*, 487:L17–L20, August 2008b. doi: 10.1051/0004-6361:200810186.

T. Van Doorsselaere, D. C. C. Birtill, and G. R. Evans. Detection of three periodicities in a single oscillating coronal loop. *A&A*, 508:1485–1491, December 2009. doi: 10.1051/0004-6361/200912753.

E. Verwichte, V. M. Nakariakov, L. Ofman, and E. E. Deluca. Characteristics of transverse oscillations in a coronal loop arcade. *Sol. Phys.*, 223:77–94, September 2004. doi: 10.1007/s11207-004-0807-6.

E. Verwichte, C. Foullon, and V. M. Nakariakov. Fast magnetoacoustic waves in curved coronal loops. *A&A*, 446:1139–1149, February 2006a. doi: 10.1051/0004-6361:20053955.

E. Verwichte, C. Foullon, and V. M. Nakariakov. Fast magnetoacoustic waves in curved coronal loops. II. Tunneling modes. *A&A*, 449:769–779, April 2006b. doi: 10.1051/0004-6361:20054398.

E. Verwichte, C. Foullon, and V. M. Nakariakov. Seismology of curved coronal loops with vertically polarised transverse oscillations. *A&A*, 452:615–622, June 2006c. doi: 10.1051/0004-6361:20054437.

E. Verwichte, M. J. Aschwanden, T. Van Doorsselaere, C. Foullon, and V. M. Nakariakov. Seismology of a Large Solar Coronal Loop from EUVI/STEREO Observations of its Transverse Oscillation. *ApJ*, 698:397–404, June 2009. doi: 10.1088/0004-637X/698/1/397.

E. Verwichte, C. Foullon, and T. Van Doorsselaere. Spatial Seismology of a Large Coronal Loop Arcade from TRACE and EIT Observations of its Transverse Oscillations. *ApJ*, 717:458–467, July 2010. doi: 10.1088/0004-637X/717/1/458.

E. Verwichte, T. Van Doorsselaere, C. Foullon, and R. S. White. Coronal Alfvén Speed Determination: Consistency between Seismology Using AIA/SDO Transverse Loop Oscillations and Magnetic Extrapolation. *ApJ*, 767:16, April 2013. doi: 10.1088/0004-637X/767/1/16.

T. Wang. Standing Slow-Mode Waves in Hot Coronal Loops: Observations, Modeling, and Coronal Seismology. *Space Sci. Rev.*, 158:397–419, July 2011. doi: 10.1007/s11214-010-9716-1.

T. Wang, S. K. Solanki, W. Curdt, D. E. Innes, and I. E. Dammasch. Doppler Shift Oscillations of Hot Solar Coronal Plasma Seen by SUMER: A Signature of Loop Oscillations? *ApJ*, 574:L101–L104, July 2002. doi: 10.1086/342189.

T. Wang, L. Ofman, J. M. Davila, and Y. Su. Growing Transverse Oscillations of a Multistranded Loop Observed by SDO/AIA. *ApJ*, 751:L27, June 2012. doi: 10.1088/2041-8205/751/2/L27.

T. J. Wang and S. K. Solanki. Vertical oscillations of a coronal loop observed by TRACE. *A&A*, 421:L33–L36, July 2004. doi: 10.1051/0004-6361:20040186.

T. J. Wang, S. K. Solanki, D. E. Innes, W. Curdt, and E. Marsch. Slow-mode standing waves observed by SUMER in hot coronal loops. *A&A*, 402:L17–L20, May 2003a. doi: 10.1051/0004-6361:20030448.

T. J. Wang, S. K. Solanki, W. Curdt, D. E. Innes, I. E. Dammasch, and B. Kliem. Hot coronal loop oscillations observed with SUMER: Examples and statistics. *A&A*, 406:1105–1121, August 2003b. doi: 10.1051/0004-6361:20030858.

T. J. Wang, S. K. Solanki, and M. Selwa. Identification of different types of kink modes in coronal loops: principles and application to TRACE results. *A&A*, 489: 1307–1317, October 2008. doi: 10.1051/0004-6361:200810230.

A. Wasiljew and K. Murawski. Numerical simulations of the first harmonic kink mode of vertical oscillations of a solar coronal loop. *A&A*, 498:863–868, May 2009. doi: 10.1051/0004-6361/200811025.

R. S. White and E. Verwichte. Transverse coronal loop oscillations seen in unprecedented detail by AIA/SDO. *A&A*, 537:A49, January 2012. doi: 10.1051/0004-6361/201118093.

T. Wiegelmann. Nonlinear force-free modeling of the solar coronal magnetic field. *Journal of Geophysical Research (Space Physics)*, 113:A03S02, March 2008. doi: 10.1029/2007JA012432.

A. Witkin. Scale space filtering. In *Proc. Int. Joint Conf. Artificial Intell.*, Espoo, Finland, 1983.

T. N. Woods, F. G. Eparvier, R. Hock, A. R. Jones, D. Woodraska, D. Judge, L. Didkovsky, J. Lean, J. Mariska, H. Warren, D. McMullin, P. Chamberlin, G. Berthiaume, S. Bailey, T. Fuller-Rowell, J. Sojka, W. K. Tobiska, and R. Viereck. Extreme Ultraviolet Variability Experiment (EVE) on the Solar Dynamics Observatory (SDO): Overview of Science Objectives, Instrument Design, Data Products, and Model Developments. *Sol. Phys.*, 275:115–143, January 2012. doi: 10.1007/s11207-009-9487-6.

T. V. Zaqarashvili, V. N. Melnik, A. I. Brazhenko, M. Panchenko, A. A. Konovalenko, A. V. Franzuzenko, V. V. Dorovskyy, and H. O. Rucker. Radio seismology of the outer solar corona. *A&A*, 555:A55, July 2013. doi: 10.1051/0004-6361/201321548.